

UF-IHEPA 00-01

EXCLUSIVE MEASUREMENTS IN $B \rightarrow D^* N \bar{N} X$

BY

ANTONIO I. RUBIERA

A DISSERTATION PRESENTED TO THE GRADUATE SCHOOL
OF THE UNIVERSITY OF FLORIDA IN PARTIAL FULFILLMENT
OF THE REQUIREMENTS FOR THE DEGREE OF
DOCTOR OF PHILOSOPHY

UNIVERSITY OF FLORIDA

2000

ACKNOWLEDGMENTS

If the pursuit of an undergraduate degree is comparable to a 500-meter race, the pursuit of a doctorate is more like a marathon. Many people have been instrumental to me finishing this marathon.

The idea for this analysis came from my advisor, John Yelton, who played a principal role in its success. His patience and wisdom have been instrumental in my development as a scientist. Paul Avery offered helpful criticisms along the way which helped me improve my delivery of the results. I would also like to thank the University of Florida faculty members who have been most helpful to me, for the courses they taught, and the professional guidance they willingly volunteered: Pierre Ramond, Charles Thorn, Zongan Qiu, and Bernard Whiting. While at Cornell I was guided and helped by David Besson, Brian Helstley, David Jaffe and Andy Foland. Many of the suggestions that have improved the quality of this analysis came from these colleagues. My fellow graduate students in the CLEO Florida group, Jiu Zheng and Craig Prescott, were patient in their guidance. Andy Foland and Craig Prescott proved to me that brilliance can be achieved without arrogance.

The long and tortuous road to the finish line would not be possible without the unflinching support of my family: my grandfather and grandmother, my father and mother. I fail to find words that accurately describe how deeply I feel my debt to them. Neither my grandfather nor my mother lived to see their seeds bear fruit. Their positive influence is sorely missed.

The lunch CLEO software elite endured my opinions: Andreas Warburton, David Urner, Peter Gaidarev, Martin Lohner, Chris Jones and Adam Lyon. The

Chapter House gang, Rahida, Samina, Basit and Mike Marsh, made my Friday nights during the nine months of Ithaca summer considerably more enjoyable than they would have been otherwise. I thank the deplorable upstate New York weather for forcing me to work harder. The Chapter House gang also endured my opinions, but with the added advantage of a few beers. Herbert, Pia, and baby Gabriel offered me company off-CLEO while I lived in Ithaca. Lauren Hsu and Antonella Cipollone allowed me to pass on some of my analysis experience. I thank Jean Duboscq and Bonnie Valant-Spaight, and Stefan Anderson.

I have been fortunate to be graced with friends who have offered me their company and their understanding during the bad times and loads of fun during the good times: From Cornell EE, Wolfgang Hofman and Jason Reed; From UF, Steve Thomas (who shared with me his deep insights into French culture), Dawn Shuler, Mike (DR) Jones, Richard Pietri, Richard Haas and Ilsa Webeck; From Miami High/Miami/Cornell, Christine Sobilo, Luis (Kike) Ramos, George and Oscar Hernandez, Armando Garcia de la Torre, Elizabeth San Martin, Elizabeth Padron, Mario and Blanca Berrios, Jimmy Windsor, Jimmy Windsor Jr, Tiburon, and others who I may have unwittingly forgotten. Barbara Tuchman and Henry Kissinger provided invaluable reading material. Madonna, Depeche Mode, and the Orb provided great music.

I hope a new generation of graduate students is able to profit from this analysis, and thank the CLEO collaboration for all its support.

TABLE OF CONTENTS

ACKNOWLEDGMENTS	ii
ABSTRACT	vii
CHAPTERS	
1 INTRODUCTION	1
1.1 Matter	2
1.1.1 Hadrons	2
1.1.2 Leptons.	4
1.1.3 Gauge Bosons	5
1.1.4 Spin and Statistics	6
1.1.5 The CKM Matrix	6
1.1.6 Symmetries	7
1.2 Decays	8
1.2.1 Weak Decays	8
1.2.2 Strong Decays	10
1.3 B Meson Decays	13
1.3.1 Quantum Chromodynamics	16
1.3.2 Heavy Quark Effective Theory	17
1.3.3 Semileptonic Decays to Mesons	19
1.3.4 Hadronic Decays to Mesons	19
1.4 $B \rightarrow$ Baryons	21
1.4.1 Results to Date	21
1.4.2 The Argument for $B \rightarrow [D]N\bar{N}X$ modes	22
1.4.3 Thesis Overview	23
2 CLEO II DETECTOR	28
2.1 Sub-detector Components	30
2.2 Tracking System	33
2.2.1 PTL Detector	34
2.2.2 SVX Detector	34
2.2.3 Drift Chamber	34
2.2.4 Momentum and Angular Resolution	35
2.2.5 dE/dx Measurements	36

2.2.6	Time-of-Flight Measurements	40
2.3	Electromagnetic Calorimeter	40
2.3.1	Dimensions	42
2.3.2	Clustering	43
2.4	Muon Detector	46
3	PARTICLE SELECTION	47
3.1	Data Sample	48
3.2	Monte Carlo Sample	48
3.3	Track Selection	49
3.3.1	Fitting Algorithm	49
3.3.2	Drift Chamber Track Variables	50
3.3.3	The TRKMNG Package	51
3.4	Particle Separation	51
3.5	π^0 Reconstruction	53
3.6	D^* Reconstruction	54
3.6.1	The KNLIB Fitting Package	54
3.6.2	Fit Optimization	55
3.6.3	Comparison with $B \rightarrow D^* X$	63
3.7	Antineutron Showers	65
3.7.1	Shower Parameters	67
3.7.2	Antiproton Showers in Data	68
3.7.3	Antineutron Selection Criteria	70
3.7.4	Antineutron Backgrounds	73
4	MEASUREMENT OF $B^0 \rightarrow D^{*-} P \bar{P} \pi^+$	75
4.1	Monte Carlo Reliability	75
4.2	Reconstruction Procedure	76
4.3	Monte Carlo Study	77
4.4	Results in Data	79
4.5	Resonant Substructure	89
4.5.1	Two-body Decay and Possible Strong Resonances	89
4.5.2	Δ Baryon Contributions in the Form of $B^0 \rightarrow D^{*-} \bar{p} \Delta^{++}$ and $B^0 \rightarrow D^{*-} p \bar{\Delta}^0$	90
4.6	Backgrounds	91
4.7	Systematic Uncertainties	93
5	MEASUREMENT OF $B^0 \rightarrow D^{*-} P \bar{N}$	94
5.1	Reconstruction Procedure	95
5.2	$D_s^+ \rightarrow p \bar{n}$ in Monte Carlo	96

5.3	Results in Data	101
5.4	$D_s^+ \rightarrow p \bar{n}$ in Data	104
5.5	$\mathcal{B}(B^0 \rightarrow D^{*-} p \bar{n})$ Measurements.	106
5.6	Correction Factor	109
5.7	Use of a $\bar{\Lambda}$ Sample	110
5.7.1	Backgrounds in Signal and Generic Monte Carlo	114
5.8	Antineutron Directional Cosine Resolution	115
5.9	$\bar{B}^0 \rightarrow D^{*+} \bar{p} n$	116
5.10	Systematic Uncertainties	118
6	CONCLUSION	119
6.1	$B \rightarrow$ Baryons phenomenology	120
6.2	Possible Future $B \rightarrow$ Baryons Modes at CLEO	121
6.3	Significance of Results	121
	REFERENCES	123
	BIOGRAPHICAL SKETCH	126

Abstract of Dissertation Presented to the Graduate School
of the University of Florida in Partial Fulfillment of the
Requirements for the Degree of Doctor of Philosophy

UF-IHEPA 00-01

EXCLUSIVE MEASUREMENTS IN $B \rightarrow D^* N \bar{N} X$

By

Antonio I. Rubiera

August 2000

Chairman: J. Yelton
Major Department: Physics

We report the first observation of exclusive decays of the type $B \rightarrow D^* N \bar{N} X$, where N is a nucleon. Using a sample of 9.7×10^6 $B\bar{B}$ pairs collected with the CLEO detector operating at the Cornell Electron Storage Ring, we measure the branching fractions $\mathcal{B}(B^0 \rightarrow D^{*-} p \bar{p} \pi^+) = (6.5_{-1.2}^{+1.3} \pm 1.0) \times 10^{-4}$, and $\mathcal{B}(B^0 \rightarrow D^{*-} p \bar{n}) = (14.5_{-3.0}^{+3.4} \pm 2.7) \times 10^{-4}$. The charge conjugate process is implied in the reconstruction of $B^0 \rightarrow D^{*-} p \bar{p} \pi^+$. However, in the reconstruction of $B^0 \rightarrow D^{*-} p \bar{n}$, only the mode with the antineutron is used in our measurement because neutrons do not have a distinctive annihilation signature.

Antineutrons are identified by their annihilation in the CsI electromagnetic calorimeter. Since we are unable to isolate a sample of antineutrons in data, we use antiproton annihilation showers in a $\bar{\Lambda} \rightarrow \bar{p} \pi^+$ sample to define the antineutron selection criteria. We find a discrepancy for antiproton annihilation showers between the Monte Carlo and data, which we assume affects antineutrons as well. We increase the raw yield for $B^0 \rightarrow D^{*-} p \bar{n}$ by 21% to correct for this discrepancy.

The possible contributions from $B^0 \rightarrow D^{*-} D_s^+$ with $D_s^+ \rightarrow p \bar{n}$ and $B^0 \rightarrow D^{*-} D_s^{*+}$ with $D_s^{*+} \rightarrow D_s^+ \gamma$ and $D_s^+ \rightarrow p \bar{n}$ are eliminated from the analysis by rejecting events with $1.91 \text{ GeV} < M_{p\bar{n}} < 2.04 \text{ GeV}$ for a loss of 9% in the reconstruction efficiency. We fail to find evidence for the decay $D_s^+ \rightarrow p \bar{n}$.

We search for possible contributions to the resonant substructure of $B^0 \rightarrow D^{*-} p \bar{n}$ and $B^0 \rightarrow D^{*-} p \bar{p} \pi^+$ due to a heavy charmed baryon decaying strongly to $\bar{p} D^{*-}$ for $B^0 \rightarrow D^{*-} p \bar{p} \pi^+$ and $\bar{n} D^{*-}$ for $B^0 \rightarrow D^{*-} p \bar{n}$, as well as a resonance of the virtual W decaying to $p\bar{p}\pi^+$. We also study the possible effect of feed-down Δ baryon contributions to the background for both modes, as well as the $B^0 \rightarrow D^{*-} p \bar{p} \pi^+$ signal. No conclusive evidence is found for a measurable contribution from the aforementioned contributions to the resonant substructure.

Antineutrons are used for the first time in the exclusive reconstruction of a B meson. By finding conclusive evidence for the existence of decay modes of the type $B \rightarrow DN\bar{N}X$, we challenge the assumption that the $B \rightarrow \text{Baryons}$ rate is dominated by decays to charmed baryons.

List of Figures

1.1	A Feynman diagram for neutron beta decay in Fermi Weak Theory	9
1.2	A Feynman diagram for neutron beta decay in the Standard Model	9
1.3	A Feynman diagram for $D^* \rightarrow D^0 \pi_{soft}$	11
1.4	A second Feynman diagram for $D^* \rightarrow D^0 \pi_{soft}$	12
1.5	A color-allowed Feynman diagram for $B^- \rightarrow D^0 \pi^-$ for one quark color	14
1.6	A color-suppressed Feynman diagram for $B^- \rightarrow D^0 \pi^-$ for one quark color	15
1.7	A Feynman diagram for $B^- \rightarrow \Lambda_c^+ \bar{p} \pi^-$	22
1.8	Two Feynman diagrams for $B^0 \rightarrow D^{*-} p \bar{n}$	26
1.9	A Feynman diagram for $B^0 \rightarrow D^{*-} p \bar{p} \pi^+$	27
2.1	Cross section into hadrons from the collision of e^+e^- beams at CESR as measured by the CLEO II detector in the energy range 9.44 GeV to 10.62 GeV	29
2.2	Front view of the CLEO II detector	31
2.3	Side view of the CLEO II detector	32
2.4	dE/dx vs. track momentum	38
2.5	Main drift chamber (DR) wire arrangement	39
2.6	Time-of-Flight vs. track momentum	41
2.7	Layout of CLEO II detector showing barrel and endcap calorimeter sections	42
3.1	$m_{D^*-m_{D^0}}$ in GeV for $B \rightarrow D^* X$ with $\bar{D}^0 \rightarrow K^+ \pi^-$ in CLEO II	57
3.2	$m_{D^*-m_{D^0}}$ in GeV for $B \rightarrow D^* X$ with $\bar{D}^0 \rightarrow K^+ \pi^-$ in CLEO II.5	58
3.3	$m_{D^*-m_{D^0}}$ in GeV for $B \rightarrow D^* X$ with $\bar{D}^0 \rightarrow K^+ \pi^- \pi^0$ in CLEO II	59
3.4	$m_{D^*-m_{D^0}}$ in GeV for $B \rightarrow D^* X$ with $\bar{D}^0 \rightarrow K^+ \pi^- \pi^0$ in CLEO II.5	60
3.5	$m_{D^*-m_{D^0}}$ in GeV for $B \rightarrow D^* X$ with $\bar{D}^0 \rightarrow K^+ \pi^- \pi^+ \pi^-$ in CLEO II	61
3.6	$m_{D^*-m_{D^0}}$ in GeV for $B \rightarrow D^* X$ with $\bar{D}^0 \rightarrow K^+ \pi^- \pi^+ \pi^-$ in CLEO II.5	62
3.7	E_{main} vs. PQCD for protons and antiprotons in CLEO II	70
3.8	E_{main} vs. PQCD for protons and antiprotons in CLEO II	71
3.9	E_{main} in GeV without proton requirement for \bar{n} 's, γ 's from π^0 's, and K_L 's	74
3.10	E_{main} in GeV with proton requirement for \bar{n} 's, γ 's from π^0 's, and K_L 's	74

4.1	ΔE vs M_{BC} distribution for $B^0 \rightarrow D^{*-} p \bar{p} \pi^+$ in CLEO II ON resonance data.	80
4.2	ΔE vs M_{BC} distribution for $B^0 \rightarrow D^{*-} p \bar{p} \pi^+$ in CLEO II.5 ON resonance data	81
4.3	M_{BC} (in GeV) for $B^0 \rightarrow D^{*-} p \bar{p} \pi^+$ in CLEO II	82
4.4	M_{BC} (in GeV) for $B^0 \rightarrow D^{*-} p \bar{p} \pi^+$ in CLEO II.5.	83
4.5	M_{BC} for $B^0 \rightarrow D^{*-} p \bar{p} \pi^+$ in data	86
4.6	ΔE (in GeV) for $B^0 \rightarrow D^{*-} p \bar{p} \pi^+$ in CLEO II/II.5 data	87
4.7	π_s from D^* momentum for $B^0 \rightarrow D^{*-} p \bar{p} \pi^+$ in data and Monte Carlo	88
4.8	M_{BC} in data and generic Monte Carlo for $B^0 \rightarrow D^{*-} p \bar{p} \pi^+$ (in GeV)	92
5.1	A Feynman diagram for $D_s^+ \rightarrow p \bar{n}$	96
5.2	$M_{p+\bar{n}}$ in GeV. $B^0 \rightarrow D_s^+ D^{*-}$ with $D_s^+ \rightarrow p \bar{n}$	97
5.3	$M_{p+\bar{n}}$ (in GeV) from a reconstruction of $B^0 \rightarrow D^{*-} p \bar{n}$ in a signal Monte Carlo $B^0 \rightarrow D_s^{*+} D^{*-}$ with $D_s^+ \rightarrow p \bar{n}$	98
5.4	(white) is $B^0 \rightarrow D_s^+ D^{*-}$ with $D_s^+ \rightarrow p \bar{n}$. (dashed) is $B^0 \rightarrow D_s^{*+} D^{*-}$ with $D_s^+ \rightarrow p \bar{n}$. $M_{p+\bar{n}}$ (in GeV)	99
5.5	(white) is $B^0 \rightarrow D_s^+ D^{*-}$ with $D_s^+ \rightarrow p \bar{n}$. (dashed) is $B^0 \rightarrow D_s^{*+} D^{*-}$ with $D_s^+ \rightarrow p \bar{n}$. m_{B^0} (in GeV)	99
5.6	(white) is inclusive of all contributions. (dashed) is after exclusion of both $D_s^+ \rightarrow p \bar{n}$ contributions	101
5.7	(white) is ON resonance, (solid) is OFF resonance	102
5.8	M_{B^0} for $B^0 \rightarrow D^{*-} p \bar{n}$ in CLEO II ON resonance data	103
5.9	M_{B^0} for $B^0 \rightarrow D^{*-} p \bar{n}$ in CLEO II.5 ON resonance data	103
5.10	$M_{p+\bar{n}}$ for $B^0 \rightarrow D^{*-} p \bar{n}$ (in GeV) in CLEO II/II.5	104
5.11	$M_{p+\bar{n}}$ vs. m_{B^0} (both in GeV)	105
5.12	Inclusive m_{B^0} in data for $B^0 \rightarrow D^{*-} p \bar{n}$ (in GeV)	106
5.13	m_{B^0} in data for $B^0 \rightarrow D^{*-} p \bar{n}$ in GeV excluding both $D_s^+ \rightarrow p \bar{n}$ contributions	107
5.14	Antineutron momentum distribution (in GeV)	112
5.15	m_{B^0} in GeV for $B^0 \rightarrow D^{*-} p \bar{n}$ selection criteria applied to selected signal Monte Carlo background modes	114
5.16	m_{B^0} for $B^0 \rightarrow D^{*-} p \bar{n}$ in GeV. (white) is data, (solid) is generic MC	115
5.17	E_{main} (in GeV) for neutrons and antineutrons in $B^0 \rightarrow D^{*-} p \bar{n}$ signal Monte Carlo	117

List of Tables

1.1	Quark families	3
1.2	Anti-quark families	3
1.3	Estimated quark masses	3
1.4	Selected meson masses	4
1.5	Selected baryon masses	4
1.6	Lepton masses	5
1.7	Some characteristics of bosons	5
1.8	Some B meson decay mechanisms	13
1.9	Representative $B \rightarrow$ Baryons decay mechanisms	21
2.1	Some e^+e^- annihilation final states	30
2.2	Vertex detector and drift chamber parameters	35
2.3	Drift chamber resolution	35
2.4	Momentum resolution (δp_t) for the CLEO II data at selected values of p_t	36
2.5	Radiation lengths of material before barrel section of the calorimeter	43
2.6	Energy and angle resolutions for a photon in the barrel at two values of cluster energy	45
3.1	The CLEO data	48
3.2	Particle identification criteria	52
3.3	m_{D^0} and $m_{D^*-m_{D^0}}$ double Gaussian data cuts	63
3.4	D^* yield: $\bar{D}^0 \rightarrow K^+ \pi^-$	64
3.5	D^* yield: $\bar{D}^0 \rightarrow K^+ \pi^- \pi^0$	65
3.6	D^* yield: $\bar{D}^0 \rightarrow K^+ \pi^- \pi^+ \pi^-$	65
3.7	Shower types and energy measured in calorimeter	66
3.8	Antineutron shower selection criteria.	71
3.9	Shower population in a generic $B\bar{B}$ Monte Carlo sample without proton requirement	72
3.10	Shower population in a generic $B\bar{B}$ Monte Carlo sample with proton requirement	72
4.1	ΔE fit results for $B^0 \rightarrow D^{*-} p \bar{p} \pi^+$ signal MC in CLEO II	78
4.2	ΔE fit results for $B^0 \rightarrow D^{*-} p \bar{p} \pi^+$ signal MC in CLEO II.5 . . .	78
4.3	M_{BC} distribution fit results for $B^0 \rightarrow D^{*-} p \bar{p} \pi^+$ signal MC in CLEO II	78

4.4	M_{BC} distribution fit results for $B^0 \rightarrow D^{*-} p \bar{p} \pi^+$ signal MC in CLEO II.5	79
4.5	Results in the CLEO II/II.5 data of various fits to M_{BC} for $B^0 \rightarrow D^{*-} p \bar{p} \pi^+$	84
4.6	$B^0 \rightarrow D^{*-} p \bar{p} \pi^+$: number of events found per mode	85
4.7	% composition of generated (phase space MC) and events reconstructed (data) of $M_{p\pi^+}$ and $M_{\bar{p}\pi^+}$	90
4.8	Estimate of systematic uncertainties (in %) for $B^0 \rightarrow D^{*-} p \bar{p} \pi^+$	93
5.1	Antineutron shower selection criteria.	94
5.2	$B^0 \rightarrow D^{*-} p \bar{n}$ signal MC ϵ_{MC} 's and widths in CLEO II.	100
5.3	$B^0 \rightarrow D^{*-} p \bar{n}$ signal MC ϵ_{MC} 's and widths in CLEO II.5	100
5.4	Measurements of $B^0 \rightarrow D^{*-} p \bar{n}$ branching fractions	107
5.5	Results of various fits to m_{B^0} for $B^0 \rightarrow D^{*-} p \bar{n}$ with or without the $D_s^+ \rightarrow p \bar{n}$ contributions	108
5.6	Λ selection criteria	110
5.7	Λ double Gaussian fixed parameters	110
5.8	$\epsilon_{annihilation}$: (%) of match 1 or 2 antiprotons in $\bar{\Lambda}$'s passing annihilation shower selection cuts for six momentum spectra	111
5.9	Correction Factor (C.F.) as a function of p_{proton} and % of antineutrons found in signal Monte Carlo for each momentum range in CLEO II/II.5	113
5.10	Neutron shower selection criteria	116
5.11	Estimate of systematic uncertainties (in %) for $B^0 \rightarrow D^{*-} p \bar{n}$	118
6.1	Exclusive measurements in $B \rightarrow$ Baryons to date	119

CHAPTER 1

INTRODUCTION

The study of the elementary particles at a wide range of interaction energies has occupied scientists since the discovery of the electron in 1896 [1]. Particle physics has evolved from a field involved in the discovery of new particles to one devoted to their systematic study. A logical structure, currently explained by the Standard Model of elementary particles [2, 3, 4], has been unveiled.

The Standard Model, however, offers an incomplete picture of some experimental high energy physics results. The results we describe are amongst these. Despite some weaknesses, the Standard Model has withstood intense experimental scrutiny, and while some of the equations are currently not calculable, evidence has not been found for physics beyond the Standard Model. Particles acquire their masses in the Standard Model via the Higgs mechanism, that requires the existence of a massive gauge boson, the Higgs boson, that has yet to be found.

We first introduce particle physics phenomenology -particles and their decays, which is the information most often used by the practitioner of experimental high energy physics. A discussion of the current status of B physics phenomenology follows. Finally, we review $B \rightarrow$ Baryons previous to our results, concluding with an overview of our work and its significance.

1.1 Matter

Matter is composed of three types of indivisible constituents: leptons, gauge bosons, and quarks. Leptons and gauge bosons are found individually in Nature. Quarks combine in two types of arrangements to form hadrons. The first arrangement is of the form quark-antiquark, and is called a meson. The second arrangement, three quarks, is called a baryon. Mesons and baryons, collectively known as hadrons, comprise all the known forms of matter consisting of quarks.

Hadronic matter is said to be colorless. A color is assigned to each quark in a meson or a baryon. The three quarks in a baryon each have a different color—red, green, blue— and the combination of all three colors yields a colorless hadron. The quark and the antiquark in a meson form a color-anticolor pair (e.g. $q_{blue}\bar{q}_{blue}$).

1.1.1 Hadrons

There are three families of quarks, each consisting of two types of quark: an up-type quark, with electromagnetic charges $+2/3$ that of the electron, or $(+2/3)q_e$, and a down-type quark, with $(-1/3)q_e$. Every type of quark is called a flavor of quark.

The first and lightest family consists of the up (u) and down (d) quarks. The next family, with heavier quarks, is the charm (c) and strange (s) family. Even heavier still is the third family: the top (t) and bottom (b) quarks. All are shown in Table 1.1.

For every matter constituent there is an anti-matter constituent with opposite electromagnetic charge and equal mass, as shown in Table 1.2.

Table 1.1: Quark families

up-type (+2/3) q_e	up: u	charm: c	top: t
down-type (-1/3) q_e	down: d	strange: s	bottom: b

Table 1.2: Anti-quark families

up-type (-2/3) q_e	\bar{u}	\bar{c}	\bar{t}
down-type (+1/3) q_e	\bar{d}	\bar{s}	\bar{b}

Quarks are not found individually in Nature. Their masses can be estimated by the mass spectrum of mesons and baryons that has been measured to date. In Table 1.3 we show current best estimates of the lower and upper limits for quark masses. The estimated masses for quarks are useful in current Standard Model calculations. However, the quark mass estimates have large uncertainties, especially in the case of the up and down quarks. The values quoted in this Table and the next values quoted in this section are from the 1998 Review of particle physics [5]. The mass of the top quark $m_t = 173.8 \pm 5.2$ GeV.

Table 1.3: Estimated quark masses

Quark	Low mass	High mass
u	1.5 MeV	5 MeV
d	3 MeV	9 MeV
s	60 MeV	170 MeV
c	1.1 GeV	1.4 GeV
b	4.1 GeV	4.4 GeV

The proton, for example, has the quark content (uud), and one of the pions, the π^+ , has the quark content ($u\bar{d}$). Each type of quark is considered a distinct

flavor. The group of mesons containing a charm quark and a light antiquark (one of \bar{s} , \bar{u} , \bar{d}) is called the charm mesons.

Meson and baryon masses are known to varying degrees of accuracy, as shown in Table 1.4 for selected mesons, and Table 1.5 for selected baryons.

Table 1.4: Selected meson masses

Meson	Quark content	Mass
π^\pm	$u\bar{d}$	139.56995 ± 0.00035 MeV
K^\pm	$s\bar{u}$	493.677 ± 0.016 MeV
D^0	$c\bar{u}$	1864.6 ± 0.5 MeV
B^0	$b\bar{d}$	5279.2 ± 1.8 MeV

Table 1.5: Selected baryon masses

Meson	Quark content	Mass
proton	uud	938.27231 ± 0.00028 MeV
Λ	sud	1115.683 ± 0.006 MeV
Λ_c	cud	2284.9 ± 0.6 MeV
Λ_b	bud	5624 ± 9 MeV

1.1.2 Leptons.

The leptons, the e , the μ , and the τ , are fundamental particles. Each can be produced with an accompanying neutrino, ν_l , with $l = e, \mu$, or τ . Neutrino physics in the near future will yield a better understanding than is currently available. Neutrinos have been thought to be massless and not to mix (that is, each neutrino flavor was thought only to interact with its lepton partner). The recent observation of neutrino mixing, however, implies that neutrinos have mass [6]. Unlike quarks,

leptons are observed as single particles with well-measured masses. In Table 1.6 we show the current mass measurements. Large differences in masses are found between the electron, the muon, and the tau.

Table 1.6: Lepton masses

Lepton	Mass
electron: e^\pm	$0.51099907 \pm 0.00000015$ MeV
muon: μ^\pm	105.658389 ± 0.000034 MeV
tau: τ^\pm	$1777.05^{+0.29}_{-0.26}$ GeV

Helicity is the orientation of a particle's momentum vector in respect to its spin. Helicity can be right-handed or left-handed for all fermions except neutrinos, which are only left-handed. Antineutrinos, likewise, are only right-handed.

1.1.3 Gauge Bosons

The mediators of the physical forces, the particles that allow decays to take place, are called gauge bosons. In Table 1.7 we outline their masses and the types of interaction that each mediates. $l = e, \mu, \tau$, u =up-type quark(u, c, t), and d =down-type quark(d, s, b).

Table 1.7: Some characteristics of bosons

Boson	Force	Mass	Decays
photon	electromagnetic	massless	$\gamma \rightarrow l^+ l^-$
gluons	strong	massless	$g \rightarrow q \bar{q}$
W^\pm	weak	80.41 ± 0.10 GeV	$W^+ \rightarrow l^+ \nu_l, u \bar{d}$
Z^0	weak	91.187 ± 0.007 GeV	$W^+ \rightarrow l^+ l^-, \nu \bar{\nu}, q^+ q^-$

1.1.4 Spin and Statistics

Matter is also characterized by the statistics obeyed. Leptons and quarks are fermions, obeying Fermi statistics, an example of which is the Pauli exclusion principle for electrons occupying the same shell in an atom. The spin of leptons and quarks is $(\pm\frac{1}{2})$. Bosons obey Bose statistics, which allow an infinite number of particles to occupy the same energy state. Bosons have integral spin $(0, \pm 1)$. The different relative alignments of the spins of the individual quarks, together with the addition of angular momentum, results in a large number of possible states.

1.1.5 The CKM Matrix

The interactions of quarks from different flavor families are suppressed with respect to those within the same family. In order to correct for this discrepancy, the characteristics of a given decay as prescribed by weak theory are adjusted using the flavor mixing 3×3 unitary and complex matrix V , the Cabibbo-Kobayashi-Maskawa matrix [5], which transforms the weak d, s, b quark states to the physically measured d', s', b' quark states, to arrive at a correct theoretical understanding of a weak decay for all quark flavors:

$$V_{CKM} = \begin{pmatrix} V_{ud}(0.9745 - 0.9760) & V_{us}(0.217 - 0.224) & V_{ub}(0.004 - 0.013) \\ V_{cd}(0.217 - 0.224) & V_{cs}(0.9737 - 0.9753) & V_{cb}(0.036 - 0.042) \\ V_{td}(0.004 - 0.013) & V_{ts}(0.035 - 0.042) & V_{tb}(0.9991 - 0.9994) \end{pmatrix}$$

with

$$\begin{pmatrix} d' \\ s' \\ b' \end{pmatrix} = V \begin{pmatrix} d \\ s \\ b \end{pmatrix}$$

The diagonal elements of V are ≈ 1 , implying that decays which involve these CKM matrix elements are Cabibbo-allowed, whereas all other decays, which involve off diagonal elements, are Cabibbo-suppressed. For example, a $b \rightarrow cW^-$, $W^- \rightarrow \bar{c}s$ decay has a much larger decay rate than a $b \rightarrow cW^-$, $W^- \rightarrow \bar{c}d$ decay.

1.1.6 Symmetries

A particle and its antiparticle are said to be symmetric under CPT transformations, where C is charge conjugation, P is parity, and T is time reversal. The inversion of parity acts like a mirror in the inversion of space coordinates. CPT symmetry is valid for all forces.

A subset of this symmetry is CP. The product of a charge conjugation and a parity inversion affect a particle the same as its antiparticle. When CP is violated, a particle will prefer a different subset of decays than its antiparticle. Such is the case for neutral kaons. The K^0 and \bar{K}^0 states in weak theory are different from the physically observed strong states, the K_S , or K -short and the K_L , or K -long, each with its respective antiparticle. Short and long refer to the respective decay lifetimes. Charge symmetry is obeyed implicitly in neutral kaon decay, but parity is violated. CP violation is evident in the difference in decay rates of K_S 's and K_L 's to final states of two and three pions, the former being even under parity,

and the latter odd under parity [7]. CP violation in B decays and will be the focus of many studies in the near future.

1.2 Decays

All hadrons, except the proton and electron, are unstable and decay to lighter hadrons, leptons, and bosons. The top quark decays well before the time required to form hadrons (baryons or mesons). Therefore, the bottom group of baryons (e.g. Λ_b , with quark content bud) and mesons (e.g. B_c , with quark content $b\bar{c}$) is the group of hadrons with the largest masses currently found in Nature.

1.2.1 Weak Decays

The b quark in the B meson decays via the weak interaction. The b quark decay is often accompanied by the strong decays of soft gluons which allow for the hadronization of a large number of final states. The Fermi Electroweak theory, which aimed to explain neutron β decay, $n \rightarrow pe^-\bar{\nu}_e$, as shown by the Feynman diagram Figure 1.1, introduced the neutrino to particle physics, serving as the precursor of the Standard Model. A full theoretical understanding of this decay was accomplished by the Standard Model, in which this decay is mediated by the W vector boson, not present in the Fermi Electroweak theory. The decay $n \rightarrow pe^-\bar{\nu}_e$ is correctly described as the quark level process $d \rightarrow W^-u$, followed by $W^- \rightarrow e^-\bar{\nu}_e$, as shown by the Feynman diagram in Figure 1.2.

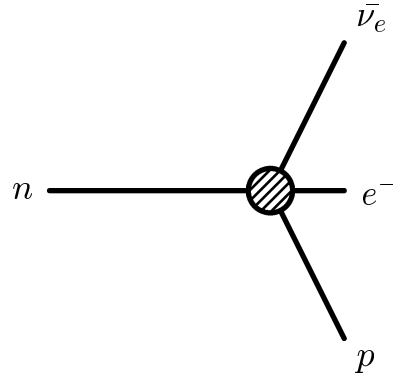


Figure 1.1: A Feynman diagram for neutron beta decay in Fermi Weak Theory

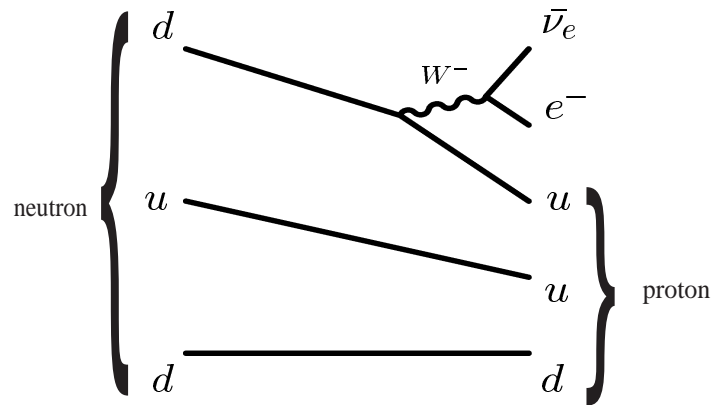


Figure 1.2: A Feynman diagram for neutron beta decay in the Standard Model

Examples of weak semi-leptonic decays of mesons, analogous to neutron β decay, are $K^+ \rightarrow \pi^0 e^+ \nu_e$, $D^0 \rightarrow K^- e^+ \nu_e$, and $B^0 \rightarrow D^- e^+ \nu_e$. The weak semi-leptonic decays of baryons follow a similar pattern. These decays are referred to as semi-leptonic decays since the final products are a combination of a weak leptonic decay and quark hadronization. Leptonic weak decays, in which the unstable particle annihilates into an $l^+ \nu_l$ pair, examples of which are $\pi^+ \rightarrow \mu^+ \nu_\mu$ and $K^+ \rightarrow \mu^+ \nu_\mu$ are the most theoretically well understood type of decays, as it lacks any final state hadronization.

1.2.2 Strong Decays

The weak decays of the heavy (charm and bottom) quarks in mesons and baryons often involve the secondary emission of strongly-interacting soft gluons. While we understand the weak component of these decays using the Standard Model, the strong component is not calculable.

The strong interaction hadronization process is not well understood theoretically when soft, or low momentum, gluons mediate the decay. The Standard Model is based on perturbation expansions which rely on convergence. A process involving soft gluons yields equations that are no longer perturbatively convergent. This stumbling block has prevented us from understanding many details of unstable particle decay, particularly for the case of heavy hadrons, in which the large mass available in the decay implies a very large number of possible final decay products from an equally large number of soft gluons.

The D^* meson, for example, which we reconstruct in this analysis, is a spin 1 meson that decays via the strong interaction. Two possible Feynman diagrams

for this decay are shown in Figures 1.3 and 1.4. Our ignorance about soft gluon strong interactions forbids us from knowing the proportion of the total decay rate due to any one diagram.

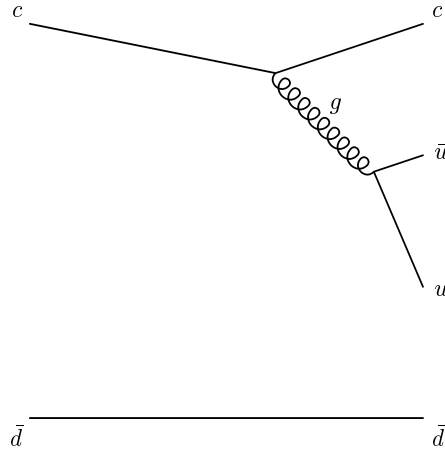


Figure 1.3: A Feynman diagram for $D^* \rightarrow D^0 \pi_{soft}$

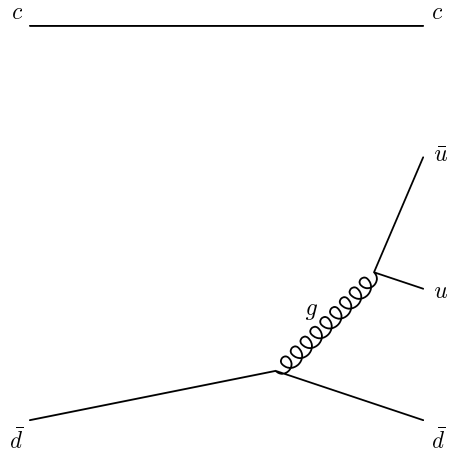


Figure 1.4: A second Feynman diagram for $D^* \rightarrow D^0 \pi_{soft}$

1.3 B Meson Decays

The B meson, which is the topic of our study, can decay to a large number of lighter particles by various mechanisms, some of which are detailed in Table 1.8. The $b \rightarrow cW^-$ type decays account for more than 95% of the B decays that are possible in the Standard Model. The combined semileptonic decay rate for the three lepton families is $\approx 25\%$, with hadronic decays accounting for almost all of the remaining decay rate.

Table 1.8: Some B meson decay mechanisms

Quark-level mechanism	Sample decay mode
Semileptonic decay: $b \rightarrow cW^-, W^- \rightarrow l^-\nu_l$	$B \rightarrow Dl^-\nu_l$
Hadronic decays: $b \rightarrow cW^-, W^- \rightarrow \bar{c}s$	$B \rightarrow DD_s$
$b \rightarrow cW^-, W^- \rightarrow \bar{u}d$	$B \rightarrow D\pi$

The W boson is colorless. Its decay to quarks constrains the color of both quarks to cancel. The number of Feynman diagrams for a given B decay by the color of the quarks. Whereas decays mediated by an external W boson allow for any of the three possible colors (for example, the π^- in $B^- \rightarrow D^0\pi^-$, as shown in the Feynman diagram in Figure 1.5). Those in which the W boson decays internally limit the color of all the quarks to be the same as that of the parent meson, as shown in the Feynman diagram in Figure 1.6. The latter quality is referred to as color suppression. Decays that only have an internal W boson-mediated diagram, such as $B^0 \rightarrow D^0\pi^0$, are color-suppressed decays.

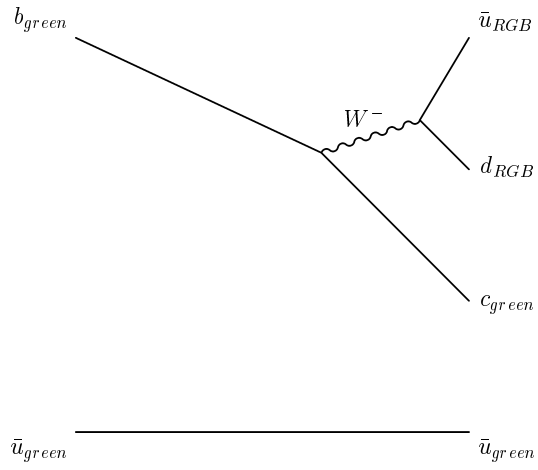


Figure 1.5: A color-allowed Feynman diagram for $B^- \rightarrow D^0 \pi^-$ for one quark color

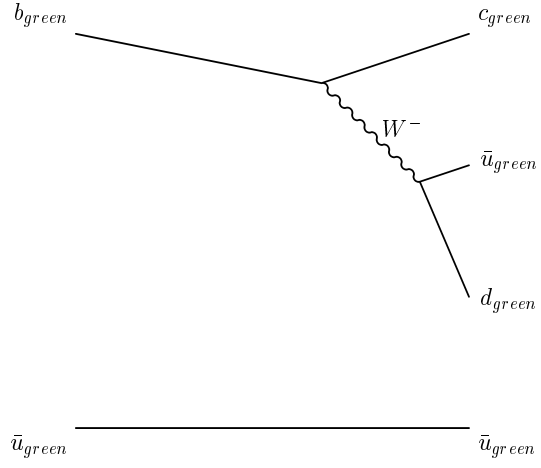


Figure 1.6: A color-suppressed Feynman diagram for $B^- \rightarrow D^0 \pi^-$ for one quark color

The decays $b \rightarrow (c, u)W^-$ are mediated by the W^- vector boson, while decays of type $b \rightarrow (s, d)\gamma$ and $b \rightarrow (s, d)g$ are mediated by neutral bosons. All decays except $b \rightarrow cW^-$ contribute a small fraction of the total decay rate. However, it is for many of these rare decays that our current phenomenological understanding allows for the closest agreement between theory and experiment.

It is theoretically allowed, and has been experimentally measured, that a B^0 meson can oscillate to a \bar{B}^0 before decay, allowing for neutral $\Upsilon(4S) \rightarrow B\bar{B}$ events with either 2 B^0 's, or 2 \bar{B}^0 's [8].

1.3.1 Quantum Chromodynamics

The Standard Model unifies the electromagnetic and the weak interactions. It also encompasses the strong interactions in the form of Quantum Chromodynamics (QCD) [9, 10]. The strong coupling constant α_s is smallest for short range interactions, or for large momentum transfer, a quality of QCD called asymptotic freedom.

The QCD Lagrangian is given by [11]:

$$\mathcal{L}_{QCD} = (\bar{q}_{red}, \bar{q}_{blue}, \bar{q}_{green})(i\gamma^\mu D_\mu - m) \begin{pmatrix} q_{red} \\ q_{blue} \\ q_{green} \end{pmatrix} + \frac{1}{2}tr(G_{\mu\nu}G^{\mu\nu}) + \text{h.c.},$$

where the covariant derivative is:

$$D_\mu = \partial_\mu + \frac{1}{2}ig\lambda^l A_\mu$$

$\frac{1}{2}\lambda^l$ are the SU(3) flavor matrices, and A_μ are the eight color gauge fields. $G_{\mu\nu}$ is the gluon field-strength tensor.

1.3.2 Heavy Quark Effective Theory

The properties of the D and B mesons, which are composed of a heavy quark and a light anti-quark, have been described using heavy-quark symmetry [12, 13] by Heavy Quark Effective Theory (HQET). In a meson, a quark and an antiquark are confined to a bound state in a cloud of virtual quarks and gluons which need to be incorporated into any calculation. In the case of a heavy meson, such as a B meson, the heavy quark has a substantially larger mass than the light antiquark. In HQET, the heavy quark is independent of the light anti-quark. HQET assumptions simplify the Standard Model equations, allowing, for instance, the comparison with theory of experimental values of V_{ub} and V_{cb} .

The effective Lagrangian that is used to characterize B decays is given by [14, 15]:

$$\mathcal{L}_{eff} = -2\sqrt{(2)}G_F J_{CC}^\mu J_{CC,\mu}^\dagger + \text{h.c.},$$

where G_F , the Fermi constant, is 1.17 GeV^{-2} , and J_{CC}^μ is the charged weak current given by:

$$J_{CC}^\mu = (\bar{\nu}_e, \bar{\nu}_\mu, \bar{\nu}_\tau)\gamma^\mu \begin{pmatrix} e_L \\ \mu_L \\ \tau_L \end{pmatrix} + (\bar{u}_L, \bar{c}_L, \bar{t}_L)\gamma^\mu V_{CKM} \begin{pmatrix} d_L \\ s_L \\ b_L \end{pmatrix}$$

The assumption that the heavy quark mass m_Q is effectively infinite is used to simplify the QCD Lagrangian. The heavy quark and the light quark are decoupled, and the effect of the cloud of virtual light quarks, light antiquarks, and gluons is assumed to be small enough to be ignored. The QCD Lagrangian, of which \mathcal{L}_{eff} is a simplified version, is simplified to:

$$\mathcal{L}_Q = \bar{Q}(i\gamma^\mu D_\mu - m_Q)Q$$

where D^μ is the QCD covariant derivative.

In the limit $m_Q \rightarrow \infty$ the strong interactions of the heavy quark become independent of its mass and spin and the effective Lagrangian is further simplified to:

$$\mathcal{L}_{HQET} = \bar{h}_v i v \cdot D h_v$$

where h_v is the effective heavy quark field and v is the hadron's velocity, which is close to that of the heavy quark.

In the calculation of HQET quantities, the strong interaction effects that are non-perturbative are grouped into a form factor that includes a dimensionless probability function, the Isgur-Wise function $\xi(v \cdot v')$ [16], where v and v' are respectively the initial and final velocities in a scattering or decay process. An example of the role this function plays is the elastic scattering of a B meson. The hadronic matrix element for this process is:

$$\frac{1}{m_B} \langle \bar{B}(v') | \bar{b}_{v'} \gamma^\mu b_v | \bar{B}(v) \rangle = \xi(v \cdot v') (v + v')^\mu$$

where b_v and $b_{v'}$ are the heavy quark fields. The heavy quark symmetry used in B physics phenomenology represents substantial progress in the theoretical description of B decays. In the next section we discuss semileptonic B decays, for which HQET has been successfully used to derive decay rates.

1.3.3 Semileptonic Decays to Mesons

The combination of large branching fractions and high reconstruction efficiencies have allowed experiments such as CLEO to measure several semileptonic B decays with high accuracy [17]. This wealth of experimental results has allowed phenomenologists to compare theory and experiment. The decay kinematics of a specific B semileptonic decay dictate the type of form factor contributions to the decay rate. In the case of $\bar{B} \rightarrow D^* l \bar{\nu}$, for example, there are no $\frac{1}{m_Q}$ corrections to the decay rate. This behavior, which is explained by Luke's theorem [18], implies that the HQET-derived decay rate for $\bar{B} \rightarrow D^* l \bar{\nu}$ has low sensitivity to higher order perturbative corrections as well as non-perturbative effects.

1.3.4 Hadronic Decays to Mesons

Whereas HQET has been useful in describing semileptonic B decays, an equally accurate description of hadronic B decays using HQET has only recently begun to be pursued for two-body decays to mesons [19, 20, 21]. Whereas in semileptonic B decays one of the two currents in a matrix element is weak, and therefore calculable to all orders in perturbation theory, in the hadronic case we have matrix elements of four-quark operators with hadronic uncertainties due to the exchange of gluons and quarks.

In energetic hadronic two-body B decays hadronization is assumed to take place after the quarks that form each of the two hadrons have traveled sufficiently long distances for there to have been no significant exchange of gluons or quarks between them. This decay characteristic is referred to as factorization, in which the matrix elements of four-quark operators factorized to independent current elements for each hadron. By using the operator product expansion (OPE) [22, 23], the weak interaction effects are treated as separate from the long range strong interaction effects. The HQET effective weak hamiltonian for $b \rightarrow c, u$ transitions after this procedure is given by:

$$\mathcal{H}_{eff} = \frac{G_F}{2}(V_{cb}[c_1(\mu)Q_1^{cb} + c_2(\mu)Q_2^{cb}] + \text{h.c.}) + Q_{b \rightarrow u} + Q_{penguin}$$

where $c_1, c_2(\mu)$ are scale dependent Wilson coefficients. $Q_{1,2}^{cb}$, $Q_{b \rightarrow u}$, and $Q_{penguin}$ are, respectively, four-quark operators for $b \rightarrow c$, $b \rightarrow u$, and penguin decays [20]. The relative strength of each type of operator as well as the Wilson coefficients are decay-dependent.

Applying the factorization hypothesis to \mathcal{H}_{eff} to, for example, the decay amplitude of the decay $\bar{B}^0 \rightarrow D^+\pi^-$, results in:

$$A_{factorized} = \frac{G_F}{2}V_{cb}V_{ud}^*a_1\langle\pi^-|(\bar{d}u)_{axial}|0\rangle\langle D^+|(\bar{c}b)_{vector}|\bar{B}^0\rangle$$

where a_1 can be verified with experiment. As the number of hadronic two-body B decays and the accuracy with which their decay rates are measured increases in the near future, it will be possible to test the decay rates derived using HQET similarly to how it has been done for semileptonic B decays.

1.4 $B \rightarrow \text{Baryons}$

A distinctive feature of the B meson system is that the large mass of the b-quark allows for many of the weak decays of the B meson to include the creation of a baryon-antibaryon pair. The as yet unmeasured decay $D_s^+ \rightarrow p \bar{n}$ bars this feature from being unique. In Table 1.9 we outline the $B \rightarrow \text{Baryons}$ decays allowed in the Standard Model.

Table 1.9: Representative $B \rightarrow \text{Baryons}$ decay mechanisms

Quark-level mechanism	Sample decay mode
Semileptonic decays: $b \rightarrow cW^-, W^- \rightarrow l^- \nu_l$ $b \rightarrow uW^-, W^- \rightarrow l^- \nu_l$	$B \rightarrow \Lambda_c \bar{p} l^- \nu_l$ $B \rightarrow p \bar{p} l^- \nu_l$
Hadronic decays: $b \rightarrow cW^-, W^- \rightarrow \bar{c}s$ $b \rightarrow cW^-, W^- \rightarrow \bar{c}s$ $b \rightarrow cW^-, W^- \rightarrow \bar{u}d$ $b \rightarrow cW^-, W^- \rightarrow \bar{u}d$ $b \rightarrow sg,$ $b \rightarrow uW^-, W^- \rightarrow \bar{u}d$	$B \rightarrow J/\psi K, J/\psi \rightarrow \text{Baryons}$ $B \rightarrow \Xi_c \bar{\Lambda}_c$ $B \rightarrow \Lambda_c \bar{p} \pi$ $B^0 \rightarrow D^{*-} p \bar{n}$ $B \rightarrow \Lambda \bar{p}, B \rightarrow p \bar{p} K$ $B \rightarrow p \bar{n} \pi$

1.4.1 Results to Date

The $B \rightarrow pX$ was measured by CLEO to be $8.0 \pm 0.5 \pm 0.3\%$ [24], assuming $B \rightarrow pX = B \rightarrow nX$. Based on this number we expect roughly 8% of all B mesons in our data to be a $B \rightarrow \text{Baryons}$ event. The Λ_c , Σ_c and Ξ_c charmed baryons have been inclusively measured in B decays [25, 26]. Upper limit exclusive measurements have been reported to date for $B \rightarrow \Lambda_c \bar{p} l^- \nu_l$ with $l = e, \mu$ [27], and selected two-body rare decays [28].

Based on the inclusive measurements reported to date, $B \rightarrow \text{Baryons}$ decays to date have been expected to be produced predominantly in decays of the type $B \rightarrow \Lambda_c \bar{p} X$, and this is the type of decay that has been exclusively reconstructed to date [29]. A typical Feynman diagram for a $B \rightarrow \bar{\Lambda}_c p X$ decay is shown in Figure 1.7.

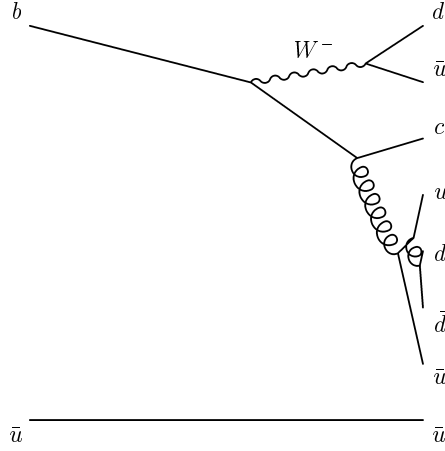


Figure 1.7: A Feynman diagram for $B^- \rightarrow \Lambda_c^+ \bar{p} \pi^-$.

1.4.2 The Argument for $B \rightarrow [D] N \bar{N} X$ modes

Combining the recently measured value $\mathcal{B}(\Lambda_c^+ \rightarrow p K^- \pi^+) = 5.0 \pm 0.5 \pm 1.2\%$ [30] with estimates of the product branching fraction $\mathcal{B}(B \rightarrow \Lambda_c X) \times \mathcal{B}(\Lambda_c \rightarrow$

$pK^-\pi^+ = 0.18\%$ [31] we can determine that $B \rightarrow \bar{\Lambda}_c pX$ modes account for only 3.6% of $B \rightarrow \text{Baryons}$, which is approximately half of the total $B \rightarrow \text{Baryons}$ rate, as measured in the inclusive $B \rightarrow pX$ measurement [24].

Based on our current knowledge of $B \rightarrow \text{Baryons}$, there must be processes other than Λ_c production that contribute to the $B \rightarrow \text{Baryons}$ rate. It is our goal to find evidence for $B \rightarrow \text{Baryons}$ decays which do not involve a Λ_c . Dunietz [32] suggested that modes of the type $B \rightarrow DN\bar{N}X$, in which D represents any charmed meson, and N a proton or neutron, are likely to be sizeable. $B \rightarrow DN\bar{N}X$ final states can arise either from the hadronization of the W boson into a baryon-antibaryon pair, or from the production of a highly excited charmed baryon that decays strongly into a baryon plus a charmed meson. CLEO previously reported an inclusive upper limit for $\mathcal{B}(B \rightarrow DN\bar{N}X)$ at the 90% confidence level of $< 4.8\%$ [24].

1.4.3 Thesis Overview

In this thesis we will attempt the exclusive reconstruction of two specific $B \rightarrow [D]N\bar{N}X$ decay modes, $B^0 \rightarrow D^{*-} p \bar{p} \pi^+$ and $B^0 \rightarrow D^{*-} p \bar{n}$. Typical Feynman diagrams for $B^0 \rightarrow D^{*-} p \bar{n}$ and $B^0 \rightarrow D^{*-} p \bar{p} \pi^+$ are shown in Figures 1.8 and 1.9, respectively.

The choice of these two modes is guided by the following criteria:

1. D^* mesons have the lowest signal contamination among the D mesons.
2. Both decays can occur via external W decay. Although this characteristic is not a principle, to date only the $b \rightarrow c$ decay modes that have been measured

share this characteristic. The reasons for the predominance of these decays are not known.

3. These are the two modes with the lowest decay daughter multiplicity, which translates into the highest reconstruction efficiency.

4. $B^0 \rightarrow D^{*-} p \bar{n}$ and $B^0 \rightarrow D^{*-} p \bar{p} \pi^+$ have low combinatoric backgrounds.

We report here, for the first time, evidence for decays of the type $B \rightarrow [D]N\bar{N}X$, and present measurements of the branching fractions $\mathcal{B}(B^0 \rightarrow D^{*-} p \bar{p} \pi^+)$ and $\mathcal{B}(B^0 \rightarrow D^{*-} p \bar{n})$. The charge conjugate process is implied in the reconstruction of $B^0 \rightarrow D^{*-} p \bar{p} \pi^+$. However, in the reconstruction of $B^0 \rightarrow D^{*-} p \bar{n}$, only the mode with the antineutron is used in our measurement because neutrons do not have the distinctive annihilation signature. These measurements invalidate the previous assumption that $B \rightarrow$ Baryons is dominated by Λ_c decays, while establishing evidence for the existence of a new type of B decay mechanism with a sizeable decay rate.

The thesis is divided as follows:

In Chapter 2 we describe the CLEO detector. We place special emphasis on the electromagnet calorimeter, which we use to select antineutron candidates.

In Chapter 3 we outline the selection criteria for the $B^0 \rightarrow D^{*-} p \bar{p} \pi^+$ and $B^0 \rightarrow D^{*-} p \bar{n}$ decay daughters. We place special emphasis on our selection of antineutron showers due to the novelty of their use.

In Chapter 4 we describe our measurement of $B^0 \rightarrow D^{*-} p \bar{p} \pi^+$, in which we use a reconstruction technique used to reconstruct decays in which the energy of all the decay daughters is well determined.

In Chapter 5 we describe our measurement of $B^0 \rightarrow D^{*-} p \bar{n}$, in which we use a reconstruction technique which is similar to that used to reconstruct other B decays with missing energy. In our case the missing energy is due to the antineutron candidate.

In Chapter 6 we conclude by summarizing our results, stressing on their significance, and outlining possible decay modes that we believe are important and measurable with the expectedly larger datasets available to future studies.

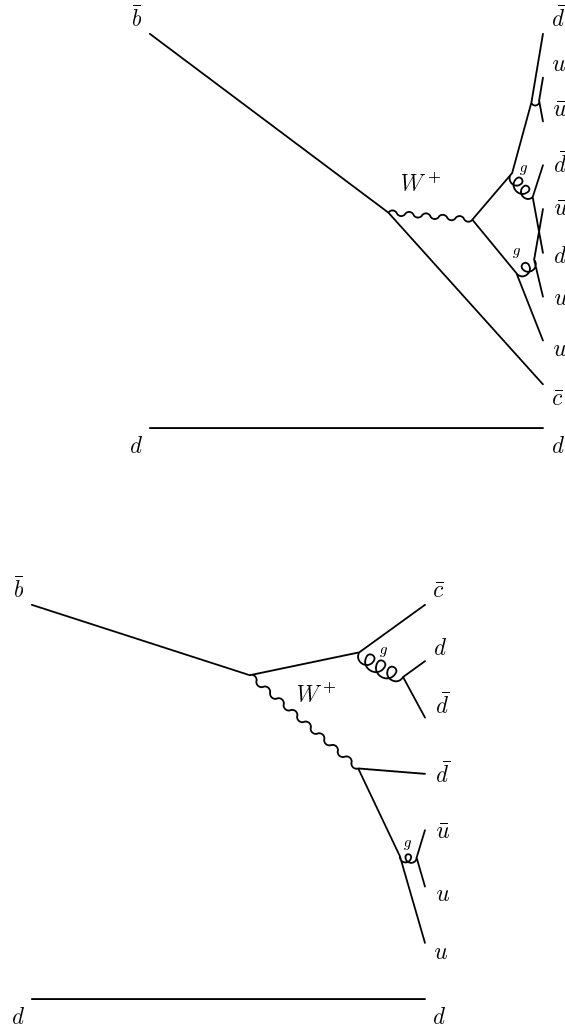


Figure 1.8: Two Feynman diagrams for $B^0 \rightarrow D^{*-} p \bar{n}$

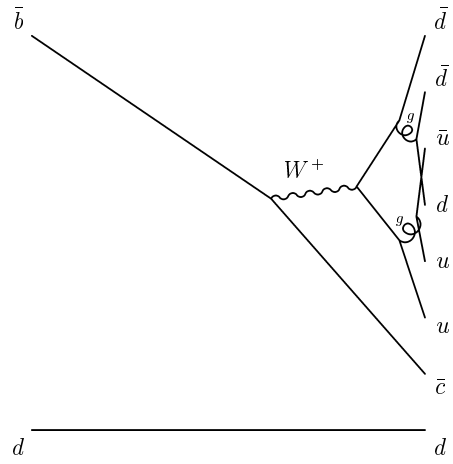


Figure 1.9: A Feynman diagram for $B^0 \rightarrow D^{*-} p \bar{p} \pi^+$

CHAPTER 2 CLEO II DETECTOR

The CLEO II detector [33] is centered at the interaction point resulting from the collision of an electron beam and a positron beam, each at ≈ 5.3 GeV beam energy, located at the Cornell Electron Storage Ring (CESR). The beams collide almost head-on, resulting in a center-of-mass total energy of ≈ 10.6 GeV. It is in the energy range near this value that the Υ resonances, with the quark content $b\bar{b}$, are produced. As shown in Figure 2.1, the $\Upsilon(1S)$ to $\Upsilon(4S)$ resonances are found in the energy range 9.44 GeV to 10.62 GeV. The $\Upsilon(4S)$ is above the threshold for strong decay to $B\bar{B}$ pairs to take place. Close to 100% of the $\Upsilon(4S)$ decay rate is to nearly equal numbers of charged and neutral $B\bar{B}$ pairs.

Data is taken at the $\Upsilon(4S)$ resonance (to be referred to as ON resonance) to study B decays. Because approximately 2/3 of the ON resonance data are composed of events in which the initial $q\bar{q}$ pair is not an $\Upsilon(4S)$, a sample of data is also taken 60 MeV below the resonance (to be referred to as OFF resonance) in order to subtract the non- $\Upsilon(4S)$, or continuum component of the ON resonance data. The e^+e^- annihilation at or near the $\Upsilon(4S)$ resonance yields a wide variety of possible final states, some which are shown in Table 2.1.

The decay product of an e^+e^- annihilation is called an event. Because final states differ greatly in cross section (the frequency with which events of a given topology are produced) some event types are produced with high frequency, while other event types are produced with low frequency. Electronic triggering on an

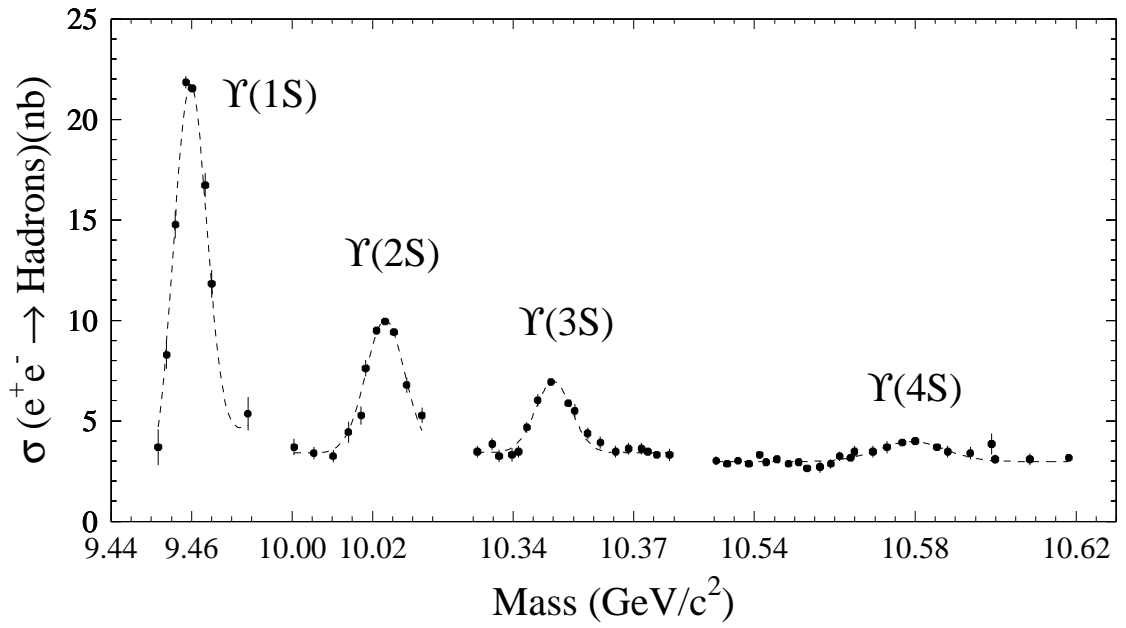


Figure 2.1: Cross section into hadrons from the collision of e^+e^- beams at CESR as measured by the CLEO II detector in the energy range 9.44 GeV to 10.62 GeV

Table 2.1: Some e^+e^- annihilation final states

$e^+e^- \rightarrow \gamma\gamma$
$e^+e^- \rightarrow l^+l^-$ (with $l=e, \mu, \tau$)
$e^+e^- \rightarrow \Upsilon(4S) \rightarrow B\bar{B}$ (requires an energy threshold)
$e^+e^- \rightarrow q\bar{q}$ (followed by hadronization)

event-by-event basis is used to select some or all of a given type of event. Triggering allows us to record only the events that we are interested in studying, most of which are of types produced with low cross sections.

2.1 Sub-detector Components

In order to get enough information out of an event, we use an ensemble of sub-detectors, each yielding incomplete information about the event. When the information from all sub-detectors is combined, we have sufficient information to measure useful physics properties. A front view and a side view of the CLEO II detector are shown in Figure 2.2 and Figure 2.3.

From the innermost to the outermost (with respect to the beam pipe, which is located at the center of the detector), the sub-detectors are:

1. Vertex detector

- (a) PTL (precision tracking layers) detector, used during the earlier part of data recording. These data will be referred to as CLEO II data.
- (b) 3-layer SVX (silicon vertex detector), used during the later part of data recording. These data will be referred to as CLEO II.5 data.

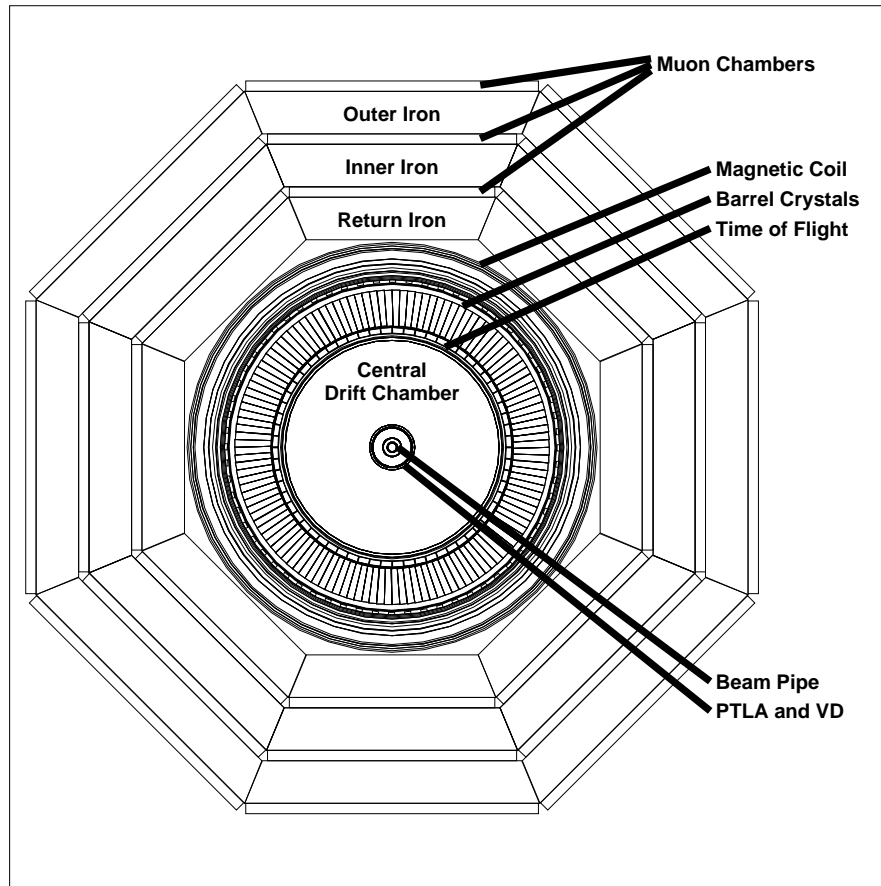


Figure 2.2: Front view of the CLEO II detector

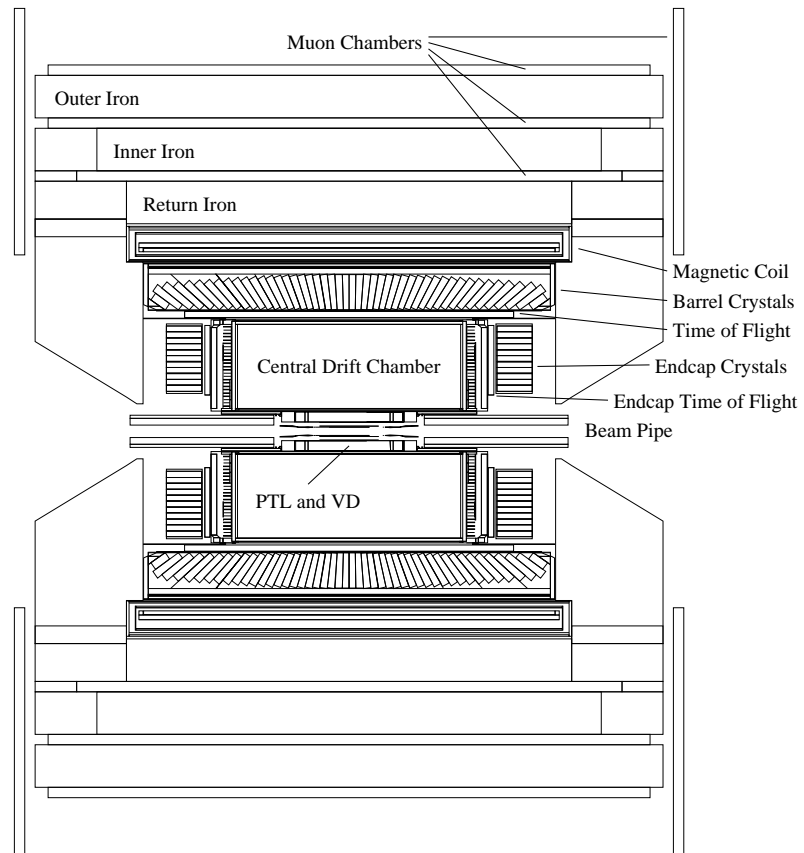


Figure 2.3: Side view of the CLEO II detector

2. Drift chamber.
3. TOF (Time-of-Flight) detector.
4. Electromagnetic calorimeter.
5. Muon detector.

The volume including all but the muon detector is enclosed in a 1.5 Tesla superconducting magnet. An important feature of this magnet is the uniformity of its magnetic field, which ensures that charged particles bend uniformly regardless of where in the detector the particle travels. A clear introduction to detectors as well as experimental methods in high energy physics is found in Perkins [34].

2.2 Tracking System

A charged particle traversing a magnetic field in the presence of charged wires in a chamber containing gas will ionize this gas as it loses energy. We measure the time at which this process takes place as well as the energy collected by each wire. These measurements allow us to know the position of the particle in time and the energy released at a number of points, or hits, along its trajectory. For a given momentum, the rate at which a particle loses energy along this trajectory, measured as dE/dx , is dependent on its mass, thus allowing us to separate protons, kaons, and pions. The TOF (Time-of-Flight) of a particle in a scintillating medium is also dependent on its mass and momentum. TOF measurements yield a second way to separate protons, kaons, and pions.

2.2.1 PTL Detector

The PTL detector is an inner drift chamber composed of six layers of straw tubes. There are 64 axial wires for each layer, and there is a half cell stagger between sequential layers. The PTL detector does not measure the longitudinal, or z-axis, position of the particle. The PTL transverse position measurements are more precise than those from the drift chamber.

2.2.2 SVX Detector

In later running of CLEO II, the PTL drift chamber was replaced by a 3-layer SVX detector capable of longitudinal as well as axial measurements [35], each measurement taking place on the two sides of each of the silicon wafers. The radii of the SVX layers are 2.35 cm, 3.25 cm, and 4.75 cm, for layers 1, 2, and 3, respectively. It is composed of 96 wafers arranged into 8 octants of 12 wafers each, with 26,208 data readout channels. The intrinsic resolution from $e^+e^- \rightarrow \mu^+\mu^-$ events at normal incidence is 29 μm .

The improved measurement resolution of the SVX detector in comparison with the PTL detector allows for more accurate determination of the event vertex. This advantage is most useful to lifetime studies, yet it does not affect greatly the results presented here.

2.2.3 Drift Chamber

The drift chamber system (the main drift chamber and the vertex detector), together with the SVX or PTL, are used to measure the momentum of charged

particles. Some vertex detector and drift chamber parameters are shown in Table 2.2. The beam pipe is located at radius 3.5 cm in the CLEO II data and at radius 2.0 cm in the CLEO II.5 data.

Table 2.2: Vertex detector and drift chamber parameters

Detector	Layers	Radius (cm)	Wires per layer
PTL (CLEO II only)	6	4.7 to 7.2	64
Vertex Detector (VD)	10	8.4 to 16	64 (first 5), 96 (second 5)
Outer Drift chamber	51	17.5 to 95	96 to 384

The $r - \phi$ and z measurement resolutions for each of the sections are shown on Table 2.3.

Table 2.3: Drift chamber resolution

Detector	$r - \phi$ resolution	z resolution
PTL (CLEO II only)	90 μm	N/A
Vertex Detector (VD)	150 μm	0.75 mm
outer drift chamber	110 μm	3 cm

The Vertex Detector (VD) is bounded by concentric inner and outer cathode strips which provide z measurements. The segmentation of the VD cathode strips is 5.85(6.85) mm along z , which is the beam direction, on the inner(outer) cathode. Segmented cathodes also bound layers 1 and 51 of the outer drift chamber. Segmentation is about 1 cm along z .

2.2.4 Momentum and Angular Resolution

There are two factors that affect the track momentum resolution:

1. The error in the measurement of the track curvature due to the hit-level measurement error in drift distance. This resolution component is parametrized by a term linear in p_t , the transverse momentum.

2. Multiple scattering at material boundaries which cause the track trajectory to deviate from a helix. This resolution component is parametrized by a constant term.

The parametrization for CLEO II data is, in GeV:

$$\left(\frac{\delta p_t}{p_t}\right)^2 = (0.0011 p_t)^2 + (0.0067)^2$$

In Table 2.4 we show this resolution in MeV for selected values of p_t .

Table 2.4: Momentum resolution (δp_t) for the CLEO II data at selected values of p_t

p_t	δp_t
0.5 GeV	3.3 MeV
1.0 GeV	6.8 MeV
1.5 GeV	10.4 MeV
2.0 GeV	14.1 MeV

The angular resolution is measured using $e^+e^- \rightarrow \mu^+\mu^-$ events, in which the typical $p_t = 5.0$ GeV. $\delta\phi = 1$ mrad and $\delta\theta = 4$ mrad. We expect $\delta\phi$ and $\delta\theta$ to be higher for the tracks we use in our analysis since muons have a much lower probability of multiple scattering than do other charged particles.

2.2.5 dE/dx Measurements

dE/dx is a function of particle mass and momentum, since $p = m\beta\gamma$, where $\beta = v/c$. The degree of separation we are able to achieve is shown in Figure 2.4

for the CLEO II data. The 51 layers of the outer, or main, drift chamber—to be referred to as DR—are used to measure the specific ionization energy loss (dE/dx) of particles.

A mixture of argon-ethane gas was used in the main drift chamber for the CLEO II data. This mixture was changed to helium-propane during data taking for CLEO II.5, which allowed for an improvement in the dE/dx resolution, resulting in better charged particle separation. In Figure 2.4 each of the particle bands has been plotted after a subtraction of some of the higher dE/dx data points in a given particle band.

The main drift chamber has contiguous cells each with a sense wire surrounded by field wires, as shown in Figure 2.5. Overall, there are three field wires for every sense wire in the main drift chamber. A number of corrections are applied to optimize the resolution:

1. Dip angle saturation: tracks perpendicular to the sense wires have the highest density of ionization along the z direction. The amount of collected charge is reduced by electric shielding for these tracks.
2. Drift distance: varies depending on the field configuration of each cell.
3. (r, ϕ) entrance angle: its magnitude as well as its sign is field dependent.
4. Axial-stereo layer: cells for axial and stereo layers have a different field dependence.

Plot not available

For information on the CLEO detector, please see: Y. Kubota et al., Nucl. Instrum. Meth.A320:66-113,1992

Figure 2.4: dE/dx vs. track momentum

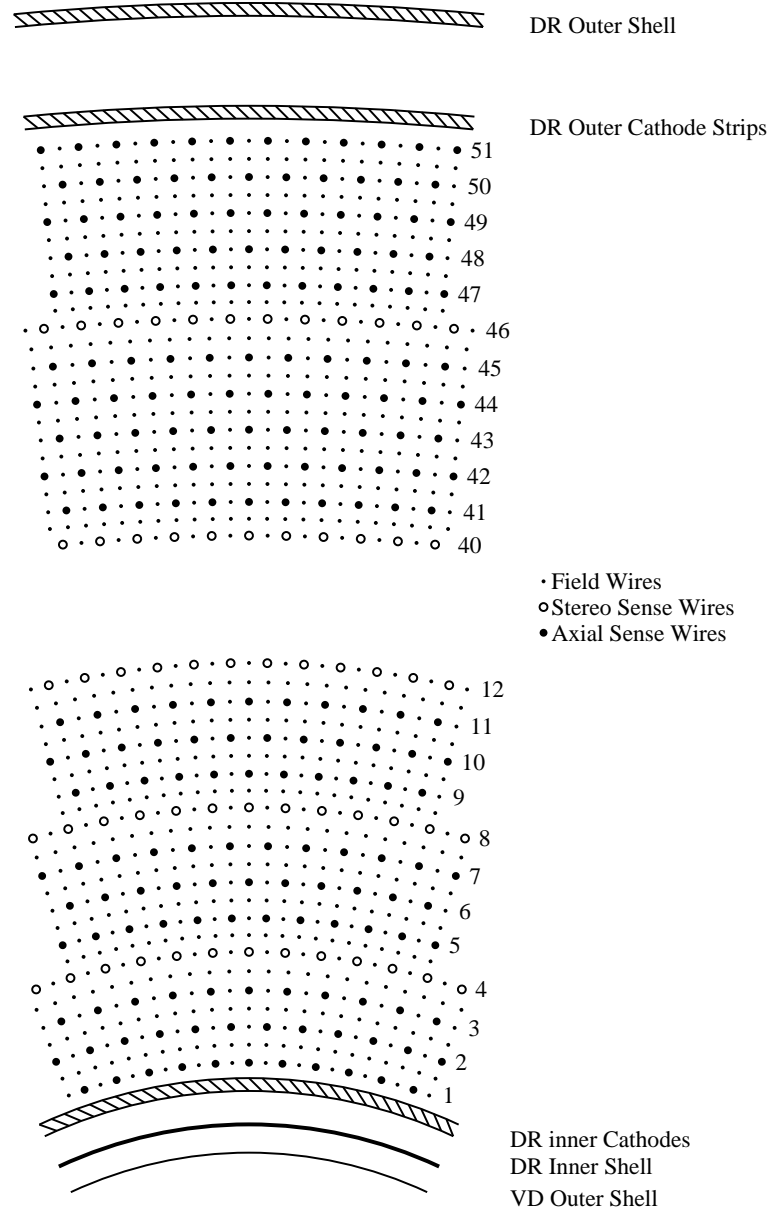


Figure 2.5: Main drift chamber (DR) wire arrangement

2.2.6 Time-of-Flight Measurements

Time-of-flight detectors surround the DR. A bar of organic scintillating material 5 cm thick has photomultiplier tubes at each end for the barrel detectors, and at one end for those in the endcaps. A time measurement is made, with a 154 ps resolution for the barrel, and 272 ps resolution for the endcaps. From the time and distance travelled, a $1/\beta$ quantity is defined. $1/\beta$ varies by particle type, as shown in Figure 2.6.

2.3 Electromagnetic Calorimeter

The electromagnetic calorimeter is used to measure the electromagnetic energy deposition of charged and neutral particles. It is composed of 7800 CsI crystals. A clustering algorithm is used to combine the energy deposition in a crystal region, which is called a shower.

The information from detector components is used in our analysis in a way that is consistent with previous CLEO II analyses with the exception of measurements from the electromagnetic calorimeter. The electromagnetic calorimeter has been used previously to measure electron and photon energy deposition. In our measurement of $B^0 \rightarrow D^{*-} p \bar{n}$ we are required to select showers that are consistent with being due to antineutrons annihilating with the CsI. The antineutron selection procedure is successful for the first time at CLEO.

Plot not available

For information on the CLEO detector, please see: Y. Kubota et al., Nucl. Instrum. Meth.A320:66-113,1992

Figure 2.6: Time-of-Flight vs. track momentum

2.3.1 Dimensions

The calorimeter is within the 1.5 Tesla magnetic field. All crystal faces are at 1 m from the interaction point, facing it in such a way that showers reach all crystals at normal incidence. A partial diagram showing some of the barrel and one of the endcaps is shown in Figure 2.7. Each calorimeter crystal is $5\text{-cm} \times 5\text{-cm} \times 30\text{-cm}$, where the latter is the length of the crystal. The choice of thallium doped CsI for the calorimeter crystals took into consideration factors such as cost, resistance to cracking, high density, and short radiation length (1.83 cm). Because the calorimeter is 16.4 radiation lengths deep, $\approx 1\%$ of the energy of a 5 GeV electron leaks out of it. There are 6,144 barrel crystals and 828 crystals for each endcap.

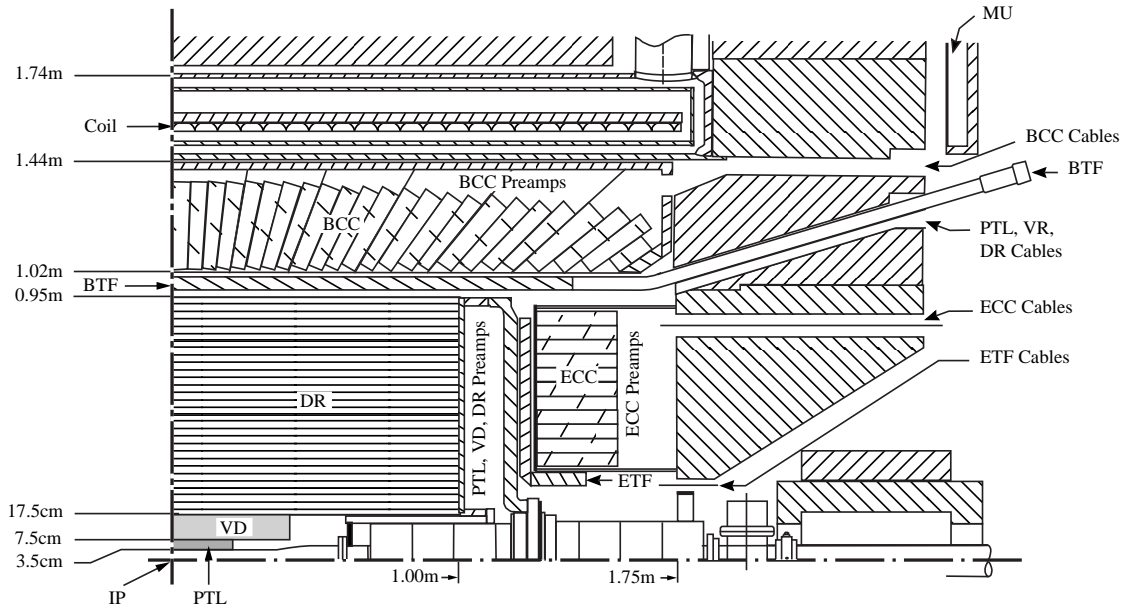


Figure 2.7: Layout of CLEO II detector showing barrel and endcap calorimeter sections

The crystals are arranged in a rectilinear grid with care taken to have a minimum of material between crystals. The material in front of the barrel section is described by radiation lengths in Table 2.5.

Table 2.5: Radiation lengths of material before barrel section of the calorimeter

Material	Radiation length (%)
beam line to layer 1 of DR	2.5
argon-ethane gas and rest of DR	0.4
DR outer cathode layer	1.0
outer DR wall	2.0
TOF counters	12.0

There is more material in front of the endcap calorimeter sections, which degrades measurement quality. We use endcap information in the π^0 reconstruction, but not for the antineutron selection criteria. The central barrel, which covers 71% of the polar angle ($45^\circ < \theta < 135^\circ$), has less material in front of it, thus providing the measurements with highest resolution.

2.3.2 Clustering

The algorithm involved in associating a group of nearby cells with energy above a threshold in the calorimeter is called clustering. An average of 430 crystals have energy recorded in a hadronic event (either $B\bar{B}$ or continuum). The raw ADC count measurements need to be calibrated using a crystal-to-crystal calibration. The sample used is Bhabba events ($e^+e^- \rightarrow e^+e^-$). This sample has high statistics and a beam energy constraint. The electrons and positrons in Bhabba events deposit almost 100% of their energy in the calorimeter. Crystal noise, which is

in the range of a few MeV, does not affect this sample appreciably. The set of constants obtained from the crystal-to-crystal calibration needs to be updated only every few months. The main change is the preponderance of a few crystals to become noisy.

A clustering algorithm for CLEO should accomplish the following:

1. Match tracks to showers.
2. Allow π^0 reconstruction.
3. Allow separation of photons and K_L 's from antineutrons.

There are two clustering packages in the CLEO II data: CCFC, and XBAL. Both accomplish these three requirements. Even though we use CCFC, using XBAL would have yielded results similar at the few % level. Our discussion of clustering is limited to CCFC. A discussion of clustering using XBAL would be similar to ours.

In order to separate shower clusters from noise, only cells with energy > 10 MeV are considered as candidates for the center of a shower. Only cells that are at most two cells away from a cell in the cluster are added to the cluster, which allows cells without an energy measurement to be located inside a cluster. The number of cells N that is considered a cluster is a function of the total energy of the cluster. For example, 4 cells correspond to a 25 MeV shower, 17 cells to a 4 GeV shower.

The position vector, which contains the directional cosines, is determined using a weighted sum of the energy measured with each cell, using the geometric center

of each to define a centroid. Two corrections, one lateral, and another longitudinal, are applied to this position vector. These corrections account for calorimeter segmentation as well as depth into the CsI crystal of the shower center.

The cluster energy E and angular resolutions, using Monte Carlo, are:

$$\text{Barrel: } \frac{\sigma_E}{E}[\%] = \frac{0.35}{E^{0.75}} + 1.9 - 1.0E$$

$$\text{Endcap: } \frac{\sigma_E}{E}[\%] = \frac{0.26}{E^{0.75}} + 2.5$$

$$\text{Barrel: } \sigma_\phi[mrad] = \frac{2.8}{\sqrt{E}} + 1.9$$

$$\text{Endcap: } \sigma_\phi[mrad] = \frac{3.7}{\sqrt{E}} + 7.3$$

$$\text{Barrel: } \sigma_\theta[mrad] = 0.8\sigma_\phi \sin(\theta)$$

$$\text{Endcap: } \sigma_\theta[mrad] = \frac{1.4}{\sqrt{E}} + 5.6$$

Using the example of a photon in the barrel, we list in Table 2.6 energy and azimuthal angular resolutions at two cluster energies. Their low values are a testament of our ability to properly reconstruct electromagnetic showers. A by-product of this ability is our success in separating baryon-antibaryon annihilation showers from electromagnetic showers.

Table 2.6: Energy and angle resolutions for a photon in the barrel at two values of cluster energy

Cluster energy	$\frac{\sigma_E}{E}[\%]$	$\sigma_\phi[mrad]$
100 MeV	3.8	11
5 GeV	1.5	3

2.4 Muon Detector

By the time a particle has traversed all the sub-detector components enclosed within the muon detector, all particles except muons have deposited most of their energy in the calorimeter and/or have been deflected by the magnetic field within the drift chamber. Since the muon detector is, above everything else, a large volume of iron, only muons are expected to pass through a significant section of the muon detector.

The nuclear absorption length λ_i for a muon in iron is 16.8 cm. It is considerably less for all other charged tracks we study. The maximum depth of iron to be traversed by a particle is between $7.2\lambda_i$ and $10\lambda_i$. We do not use the muon detector in our analysis.

CHAPTER 3

PARTICLE SELECTION

In order to reconstruct $B^0 \rightarrow D^{*-} p \bar{p} \pi^+$ and $B^0 \rightarrow D^{*-} p \bar{n}$ we need to have low background samples of all the decay daughters. Protons, antiprotons and pions are selected as single tracks, the $m_{D^*}-m_{D^0}$ distribution is used to select D^* 's, and shower selection criteria is used to select antineutrons. We select the B decay daughters from ON resonance hadronic events. The ON resonance candidates can be fully or partially reconstructed B mesons, or background candidates from ON resonance continuum events. The OFF resonance candidates can only be continuum events as the total event energy is below the energy threshold for $B\bar{B}$ production. We use the Mn_fit histogram package [36], and its function fitting utility, MINUIT [37], both of which are widely used by experimental high energy physicists.

To suppress the already small number of continuum background candidates in our reconstructions, we select events using the parameter R2GL [38]. R2GL is a measure of how the momentum is distributed for the event. A high value of R2GL corresponds to continuum events, in which the initial quarks hadronize to form a two-body decay. The $B\bar{B}$ momentum distributions are the result of two separate two-body or higher decays that can be most approximately described by a spherically symmetric momentum distribution, which tends to yield a low value of R2GL.

3.1 Data Sample

The CLEO data is collected at the $\Upsilon(4S)$ resonance (ON resonance) and 60 MeV below the resonance (OFF resonance). Roughly 2/3 of the ON resonance data is continuum and the remaining 1/3 is $B\bar{B}$ pairs. We show in Table 3.1 the integrated luminosity by dataset.

Table 3.1: The CLEO data

Dataset	ON luminosity	OFF luminosity	$B\bar{B}$'s
CLEO II	3.14 fb^{-1}	1.61 fb^{-1}	3.30×10^6
CLEO II.5	6.03 fb^{-1}	2.94 fb^{-1}	6.35×10^6

3.2 Monte Carlo Sample

We use Monte Carlo generated events to model the data in order to study the efficiency of our selection criteria as well as the effect of backgrounds. Two types of Monte Carlo samples are used:

1. Generic Monte Carlo, in which many decays are generated using our current knowledge of B decays.
2. Signal Monte Carlo, in which one of the B mesons in the event decays via a predetermined mode, such as $B^0 \rightarrow D^{*-} p \bar{n}$. The remaining \bar{B} meson in the event decays according to the prescription used to generate generic Monte Carlo events.

The generic Monte Carlo sample consists of B decays of type $b \rightarrow cW^-$. A detailed explanation of the criteria used for the generic Monte Carlo sample is

found in the Appendix of [24]. This sample does not include any $B \rightarrow [D]N\bar{N}X$ decays because until now we have had no evidence for their existence. The $B \rightarrow$ Baryons decays in the generic Monte Carlo sample are of the type $B \rightarrow \Pi W^+$, in which $\Pi \rightarrow \Lambda_c^- \bar{N}$, where \bar{N} is an antiproton or an antineutron. The conjugate modes are also generated.

3.3 Track Selection

A combination of measurements is used to select quality tracks that are most likely to be the particle type we need for a given reconstruction-pion, kaon, or proton. The tracks we use in our reconstruction are particles that are stable (in the case of protons), or decay outside our detector (in the case of kaons and pions). Therefore, a track is assumed to begin near the interaction point, which is within a solid volume defined by the uncertainty with which we can measure the beam spot. This volume is a few microns wide in x and y and a few hundred microns wide in z.

3.3.1 Fitting Algorithm

Tracks are fitted using DR hits by a Kalman algorithm that is based on the assumption that the track is a helix inside a vacuum. The change of trajectory due to material interaction is taken into consideration in the track fit. The fit is performed from both ends of the track. The inward fit begins a hit-to-hit swim, adding hits to form a track, analogous to the way beads are strung to form a necklace. Where there is more than one hit to a layer of the drift chamber, the

hit with the better resolution is chosen. The outward fit begins at the outermost layer of the drift chamber, performing a hit swim into the drift chamber.

3.3.2 Drift Chamber Track Variables

Variables we use which are defined with main drift chamber measurements (DR) are:

1. PQCD: signed 3-momentum of track. This vector does not have a correction assuming the mass of a particle type.
2. Z0CD: distance of closest approach along the z-axis. The z measurement resolution is considerably worse than the $r - \phi$ measurement resolution. However, Z0CD is effective in separating tracks from the interaction point from material interaction tracks and long decay particle daughter tracks.
3. DBCD: radial distance of point of closest approach to the interaction point. DBCD is usually more accurately determined than Z0CD.

All tracks are required to pass the following track quality cuts:

1. $PQCD < 1 \text{ GeV}$: $DBCD \text{ (in meters)} < 0.005 - (0.0038) \times |PQCD|$.
2. Low momentum tracks are more likely to have a poorly measured DBCD.
 $PQCD > 1 \text{ GeV}$: $DBCD \text{ (in meters)} < 0.001$.
3. $Z0CD < 0.05 \text{ meter}$.

3.3.3 The TRKMNG Package

A software package is used to reject duplicated tracks from curlers [39]. A curler is a low momentum track which is bent more than one revolution inside the drift chamber. A curler spirals inside the drift chamber as the momentum of the particle decreases. The tracking algorithm will often assign a track number in the list of tracks for each half-revolution. The TRKMNG package selects the half-revolution that is most likely the closest to where the track began to curl, rejecting all other half-revolutions. The variable used in the TRKMNG Package is $\text{tng}(\text{track}) \geq 0$. All negative numbers of $\text{tng}(\text{track})$ are for the redundant half-revolutions.

3.4 Particle Separation

By population size alone, all tracks are pions. The purpose of particle separation, or particle ID, is to separate tracks that are likely to be something other than a pion from the overwhelmingly more numerous pions. Protons are produced with a significantly reduced rate, therefore constituting a small background to all other charged particles. The predominant backgrounds to protons are kaons, pions, electrons and muons. For the case of kaons, pions represent the largest background. The kaon in $\bar{D}^0 \rightarrow K^+ \pi^-$ has more phase space available than the kaon in $\bar{D}^0 \rightarrow K^+ \pi^- \pi^0$ and $\bar{D}^0 \rightarrow K^+ \pi^- \pi^+ \pi^-$, which allows its kinematic separation from backgrounds. Even for the low x_p in D^* 's from B decays, the kaon in $\bar{D}^0 \rightarrow K^+ \pi^-$ can be easily separated from the pion by the decay kinematics.

Charged particle identification is accomplished by combining the specific ionization (dE/dx) measurements from the drift chamber with time-of-flight (TOF)

measurements. A normalized probability ratio L_i is used for charged particle separation.

L_i is defined as $L_i = P_i / (P_{pion} + P_{kaon} + P_{proton})$, and P_i is the particle hypothesis χ_i^2 probability combining dE/dx and TOF measurements, with χ_i^2 defined as:

$$\chi_i^2 = \left[\frac{(dE/dx)_{measured} - (dE/dx)_{expected}}{\sigma_{dE/dx}} \right]^2 + \left[\frac{(TOF)_{measured} - (TOF)_{expected}}{\sigma_{TOF}} \right]^2$$

$\sigma_{dE/dx, TOF}$ are the deviations from the mean and vary by particle type. We define the respective χ_i^2 for each particle type using the $\sigma_{dE/dx, TOF}$ for the identical particle type. L_{kaon} , for example, is defined using the $\sigma_{dE/dx, TOF}$'s for kaons. In Table 3.2 we show how our criteria varies, depending on how much information is available. By defaulting to a pion we are setting $P_i = 1.0$. Useful dE/dx information is available for the vast majority of tracks passing the track quality requirements outlined in section 3.3.2. Low momentum particles (< 200 MeV) curl before reaching the TOF detectors.

Table 3.2: Particle identification criteria

$\sigma_{dE/dx}$	σ_{TOF}	Action
< 3	< 3	use both
< 3	> 3	use $\sigma_{dE/dx}$ only
> 3	< 3	use σ_{TOF} only
> 3	> 3	default to pion

We place loose requirements of $L_{pion} > 0.001$ on all pion candidates, and the kaon candidates in $\bar{D}^0 \rightarrow K^+ \pi^-$. Kaon candidates in $\bar{D}^0 \rightarrow K^+ \pi^- \pi^0$, and $\bar{D}^0 \rightarrow K^+ \pi^- \pi^+ \pi^-$ are required to satisfy $L_{kaon} > 0.4$. Proton candidates in $B^0 \rightarrow D^{*-} p \bar{p} \pi^+$ and

$B^0 \rightarrow D^{*-} p \bar{n}$ are required to satisfy $L_{proton} > 0.9$. In addition, electron backgrounds to protons and antiprotons are rejected using the variable cut $R2ELEC < 0$. $R2ELEC$ is a logarithmic probability that a particle is an electron. Negative values of $R2ELEC$ are least likely to be for an electron. $R2ELEC$ is defined using $\frac{E}{p}$ from the electromagnetic calorimeter, which is very close to 1 for electrons, which leave all of their energy in the calorimeter, as well as a non-negligible number of protons.

3.5 π^0 Reconstruction

The π^0 's used to reconstruct $\bar{D}^0 \rightarrow K^+ \pi^- \pi^0$ decay via $\pi^0 \rightarrow \gamma\gamma$. The π^0 's in this decay are soft, with momenta < 500 MeV. The decay angle for $\pi^0 \rightarrow \gamma\gamma$ is large enough at this momentum range for the individual γ 's not to overlap. On average there are 7 π^\pm 's in a $B\bar{B}$ event. The average number of π^0 's, as of yet unmeasured, should be near this number. Since shower multiplicity increases with decreasing shower energy, as π^0 momentum decreases, the combinatoric shower background increases. A minimum momentum of 100 MeV is required of our π^0 candidates to suppress this background.

A shower is considered a γ if the ratio between the summed energy of a 3 by 3 grid of shower cells over the same are extended to a 5 by 5 grid of shower cells is almost 1. This ratio is referred to as E9OE25. Most photons have most of their energy concentrated within a 3 by 3 grid of shower cells.

We require at least one of the γ 's to be in the good barrel section of the calorimeter, which is defined as $|\cos(\theta_\gamma)| < 0.71$. When one of the γ 's is not in the barrel, we require that it not be from the overlap region between the barrel

and endcap sections of the calorimeter or near the beam pipe, both of which yield degraded shower energy measurements. We also require the candidate π^0 mass to be within 2.5σ ($\pi^0 \sigma \sim 5$ MeV) from 135 MeV central value.

3.6 D^* Reconstruction

Finding D^* candidates with high efficiency and low backgrounds is an important part of this analysis. In the decay $D^* \rightarrow D^0 \pi_{soft}$ $m_{D^*-m_{D^0}}$ is only slightly larger than the mass of the π_s . Since the $m_{D^*-m_{D^0}}$ resolution is smaller than the m_{D^*} resolution, we use the former to select D^* candidates. We verify our D^* yield with a previous analysis.

In order to reconstruct $B \rightarrow D^* X$ with $D^* \rightarrow D^0 \pi_{soft}$ correctly, we check our yield for the scaled momentum X_p range $0.25 < X_p < 0.35$. It is in this range that we find ≈ 50 % of D^* 's to be generated in signal $B^0 \rightarrow D^{*-} p \bar{p} \pi^+$ and $B^0 \rightarrow D^{*-} p \bar{n}$ Monte Carlo. We check our yield with a previous CLEO result [40].

3.6.1 The KNLIB Fitting Package

The KNLIB fitting package is a collection of kinematic routines used for track vertexing [41]. We use it to vertex D^0 's and D^* 's. D^0 's are vertexed using the KNLIB routine KNVTX3. A new invariant mass is calculated with this vertex, and only the D^0 mass range 1.70 to 2.03 GeV is allowed to pass on to D^* reconstruction. To form a D^* vertex, we use KNLIB routine KNBVXK which combines the D^0 decay products and the π_s track to make a vertex-constrained mass from which $m_{D^*-m_{D^0}}$ is calculated. We use KNBVXK with the flag IVOPT set to 1 for the π_s -

i.e. the π_s is constrained to pass through the vertex formed by the other particles, but not used to determine that vertex. The latter method offers a noticeable improvement over other options tested, including use of π_s track when vertexing, as well as using the D^0 vertex instead of the individual D^0 tracks when vertexing the D^* . We place a loose cut of $\chi^2 < 100$ on the D^* vertex fit for all three modes.

3.6.2 Fit Optimization

We reconstruct D^0 's, selecting candidates near the mean mass. After the addition of a π_s , we select candidates within a range of $m_{D^*}-m_{D^0}$ values. We use the 1998 Review of Particle Properties values for m_{D^0} , 1.8646 GeV, and $m_{D^*}-m_{D^0}$, 0.1454 GeV, as our central values [5]. The double Gaussian fits model $m_{D^*}-m_{D^0}$ better than the single Gaussian fits.

The optimization procedure is as follows:

1. The background is fitted with a second order Chebyshev polynomial.
2. The signal is fitted with a double Gaussian distribution.
3. The continuum subtracted data m_{D^0} distribution is fitted using $\text{abs}(m_{D^*}-m_{D^0}-0.1454) < 0.002$ GeV, which is a wide cut.
4. The widths, as well as the means of each of the double Gaussians are allowed to float. The best fits are obtained with non-zero Δ_{MEAN} 's. Δ_{MEAN} is the difference between the mean value of each of the two Gaussians. We integrate the double Gaussian, keeping 95% of the signal symmetrically from the PDG mean.

5. The final set of double Gaussian m_{D^0} and $m_{D^*}-m_{D^0}$ cuts from data are used in the B reconstructions, and the same cuts are applied to the Monte Carlo to find ϵ_{MC} , the signal Monte Carlo reconstruction efficiency.

Shown in Figures 3.1, 3.2, 3.3, 3.4, 3.5 and 3.6 are the double Gaussian fits for each of the three D^0 modes for either dataset, all in the X_p range $0.25 < X_p < 0.35$.

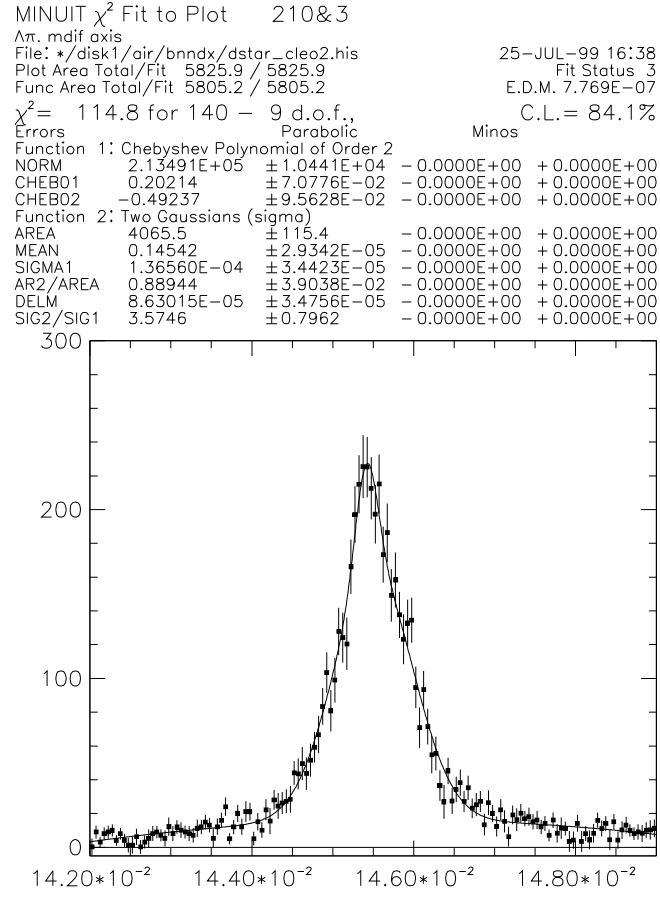


Figure 3.1: $m_{D^*} - m_{D^0}$ in GeV for $B \rightarrow D^* X$ with $\bar{D}^0 \rightarrow K^+ \pi^-$ in CLEO II

MINUIT χ^2 Fit to Plot 210&3
 $\Delta\pi$. mdif axis
File: */disk1/air/bnndx/dstar_cleo25.his 26-JUL-99 10:09
Plot Area Total/Fit 6783.2 / 6783.2 Fit Status 3
Func Area Total/Fit 6770.0 / 6770.0 E.D.M. 2.662E-07
 $\chi^2 = 126.8$ for 140 - 9 d.o.f., C.L. = 58.7%
Errors Parabolic Minos
Function 1: Chebyshev Polynomial of Order 2
NORM 2.10956E+05 $\pm 1.2915E+04$ - 0.0000E+00 + 0.0000E+00
CHEB01 0.29909 $\pm 6.6768E-02$ - 0.0000E+00 + 0.0000E+00
CHEB02 -0.42591 ± 0.1134 - 0.0000E+00 + 0.0000E+00
Function 2: Two Gaussians (sigma)
AREA 5083.6 ± 142.3 - 0.0000E+00 + 0.0000E+00
MEAN 0.14553 $\pm 1.0554E-05$ - 0.0000E+00 + 0.0000E+00
SIGMA1 2.26699E-04 $\pm 1.6435E-05$ - 0.0000E+00 + 0.0000E+00
AR2/AREA 0.55532 $\pm 5.2112E-02$ - 0.0000E+00 + 0.0000E+00
DELM 3.45832E-05 $\pm 2.8669E-05$ - 0.0000E+00 + 0.0000E+00
SIG2/SIG1 2.5902 ± 0.1501 - 0.0000E+00 + 0.0000E+00

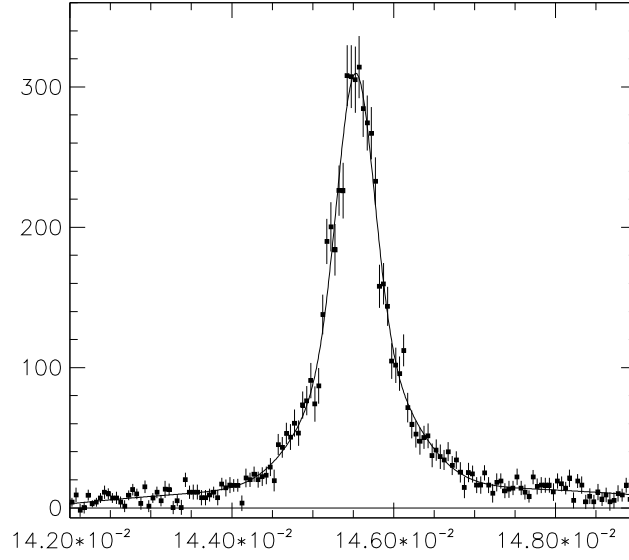


Figure 3.2: $m_{D^*} - m_{D^0}$ in GeV for $B \rightarrow D^* X$ with $\bar{D}^0 \rightarrow K^+ \pi^-$ in CLEO II.5

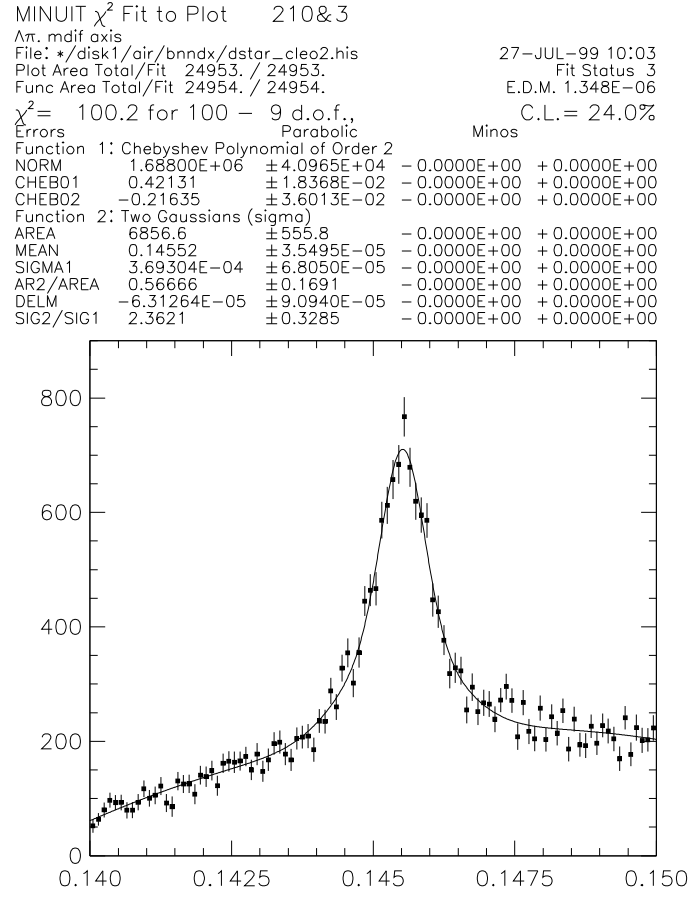


Figure 3.3: $m_{D^*} - m_{D^0}$ in GeV for $B \rightarrow D^* X$ with $\bar{D}^0 \rightarrow K^+ \pi^- \pi^0$ in CLEO II

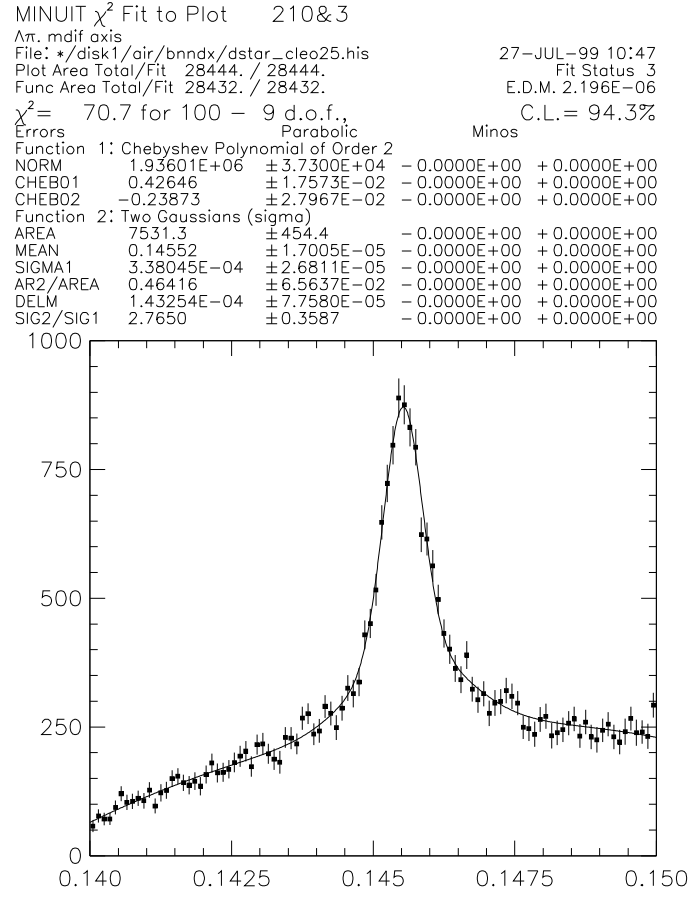


Figure 3.4: $m_{D^*} - m_{D^0}$ in GeV for $B \rightarrow D^* X$ with $\bar{D}^0 \rightarrow K^+ \pi^- \pi^0$ in CLEO II.5

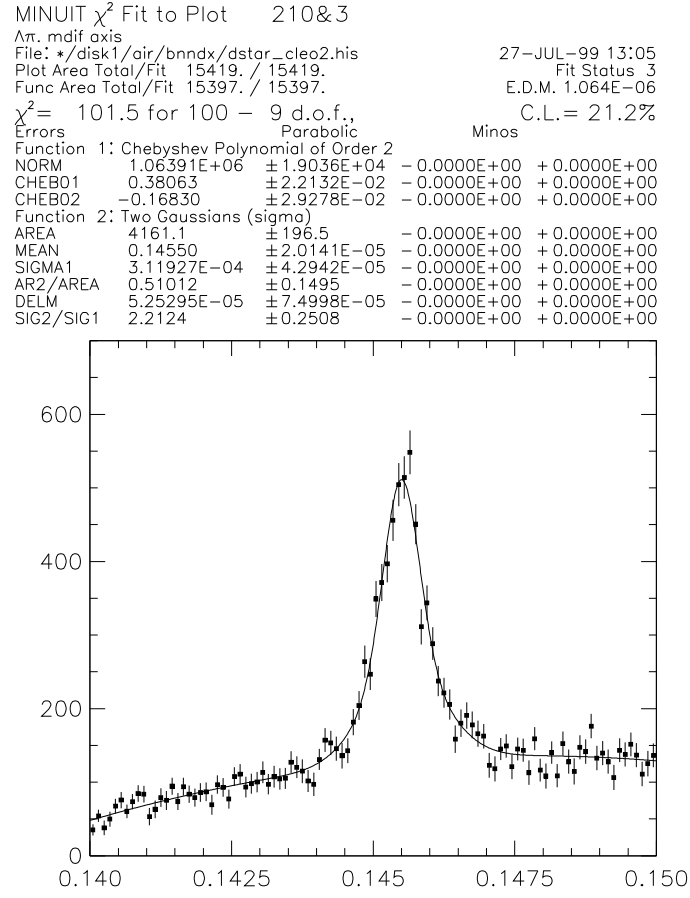


Figure 3.5: $m_{D^*} - m_{D^0}$ in GeV for $B \rightarrow D^* X$ with $\bar{D}^0 \rightarrow K^+ \pi^- \pi^+ \pi^-$ in CLEO II

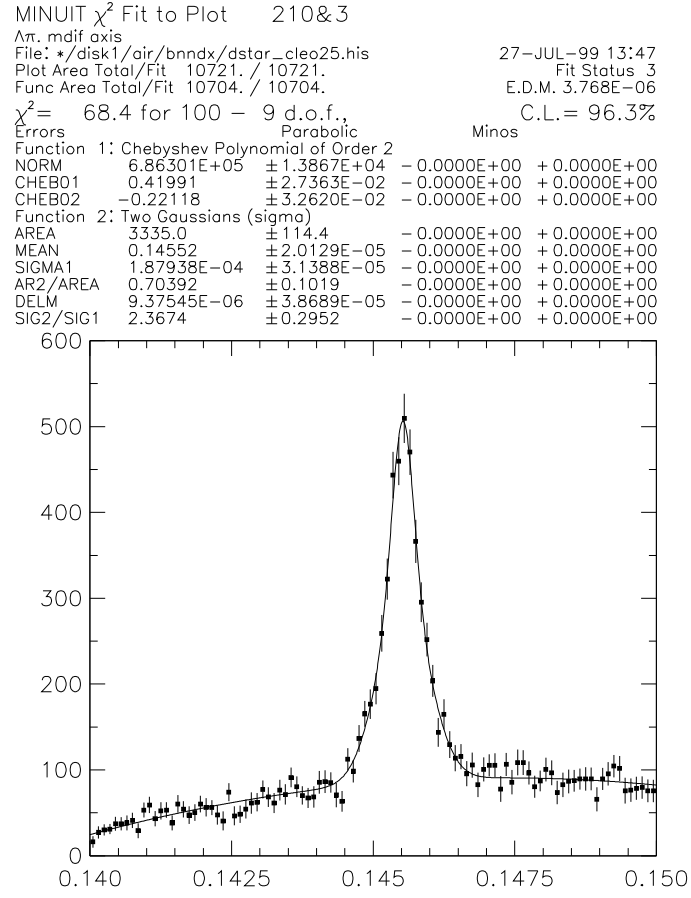


Figure 3.6: $m_{D^*} - m_{D^0}$ in GeV for $B \rightarrow D^* X$ with $\bar{D}^0 \rightarrow K^+ \pi^- \pi^+ \pi^-$ in CLEO II.5

Shown in Table 3.3 are the m_{D^0} and $m_{D^*}-m_{D^0}$ double Gaussian data cuts for all three D^0 modes and for each dataset.

Table 3.3: m_{D^0} and $m_{D^*}-m_{D^0}$ double Gaussian data cuts

Mode	Dataset	m_{D^0} in \pm MeV	$m_{D^*}-m_{D^0}$ in \pm MeV
$D^0 \rightarrow K^+ \pi^-$	CLEO II	17.5	1.15
$\bar{D}^0 \rightarrow K^+ \pi^-$	CLEO II.5	15.0	1.10
$\bar{D}^0 \rightarrow K^+ \pi^- \pi^0$	CLEO II	26.0	1.50
$\bar{D}^0 \rightarrow K^+ \pi^- \pi^0$	CLEO II.5	27.0	1.50
$\bar{D}^0 \rightarrow K^+ \pi^- \pi^+ \pi^-$	CLEO II	14.0	1.30
$\bar{D}^0 \rightarrow K^+ \pi^- \pi^+ \pi^-$	CLEO II.5	12.0	0.90

3.6.3 Comparison with $B \rightarrow D^* X$

To verify the accuracy of our D^* reconstruction, we compare our results with the PDG value $\text{Br}(B \rightarrow D^* X) = 22.7 \%$ [5]. Since ϵ_{MC} varies with momentum, we need to compare our fully reconstructed sample with the expected number in the same momentum range. In $B^0 \rightarrow D^{*-} p \bar{n}$ and $B^0 \rightarrow D^{*-} p \bar{p} \pi^+$ signal Monte Carlo is $\approx 50 \%$ of the generated D^* 's are in the scaled momentum (X_p) range from 0.25 to 0.35. Approximately 32 % of $\text{Br}(B \rightarrow D^* X)$ lies in this momentum range [40]. The expected D^* yield is given by:

$$\begin{aligned}
& (\text{Number of charged/neutral B's}) \times \\
& (\text{Br}(B \rightarrow D^* X) \text{ in } X_p \text{ range } 0.25 \text{ to } 0.35) \times \\
& (\text{Br}(D^0 \text{ mode})) \times \\
& (\text{Br}(D^* \rightarrow D^0 \pi_{soft}) = 68.3 \%) \times \\
& (D^* \epsilon_{MC}) \times
\end{aligned}$$

(0.32/0.50: efficiency correction).

This number is efficiency corrected for single and double Gaussian signal fits using $B^0 \rightarrow D^{*-} p \bar{n}$ Monte Carlo. The corrected product is the expected yield that we compare to our respective fitted yield for each mode.

The close agreement between the expected yield from Monte Carlo and the data result for each mode, as shown on Tables 3.4, 3.5, and 3.6, is a function of how well our Monte Carlo models D^* decays from B mesons and of the accuracy of our reconstruction code. The double Gaussian fits yield better agreement than the single Gaussian fits. There is a significant drop in reconstruction efficiency for all three D^0 modes in the CLEO II.5 data. This drop is due to the significantly reduced reconstruction efficiency of the soft pion in $D^* \rightarrow D^0 \pi_{soft}$ in CLEO II.5. Whereas in CLEO II the PTL drift chamber is used in the tracking algorithm, the SVX silicon detector which replaces it in the CLEO II.5 data, in addition to having more material, is not used in the tracking algorithm.

Table 3.4: D^* yield: $\bar{D}^0 \rightarrow K^+ \pi^-$

Dataset	Single Gaussian ϵ_{MC}	Expected yield	Found	Double Gaussian ϵ_{MC}	Expected yield	Found
CLEO II	30.8 %	3,862.3	4,117.8	33.0 %	4,138.1	4,065.5
CLEO II.5	16.3 %	3,933.1	4,455.2	20.7 %	4,994.9	5,083.6

Table 3.5: D^* yield: $\bar{D}^0 \rightarrow K^+ \pi^- \pi^0$

Dataset	Single Gaussian ϵ_{MC}	Expected yield	Found	Double Gaussian ϵ_{MC}	Expected yield	Found	$S / \sqrt{S+B}$
CLEO II	14.0 %	6,371.3	5,955.8	15.3 %	6,963.0	6,856.6	59.7
CLEO II.5	8.4 %	7,356.0	6,138.5	8.9 %	7,793.9	7,531.3	61.4

Table 3.6: D^* yield: $\bar{D}^0 \rightarrow K^+ \pi^- \pi^+ \pi^-$

Dataset	Single Gaussian ϵ_{MC}	Expected yield	Found	Double Gaussian ϵ_{MC}	Expected yield	Found	$S / \sqrt{S+B}$
CLEO II	14.5 %	3,560.6	3,637.6	16.0 %	3,928.9	4,161.6	48.3
CLEO II.5	6.5 %	3,071.3	3,100.5	6.9 %	3,260.3	3,335.0	47.7

3.7 Antineutron Showers

We need to define a set of criteria which allows us to select antineutrons with high accuracy without incurring a large loss in efficiency. The following characteristics, some limiting, some exploitable, apply to antineutron showers in the CLEO II electromagnetic calorimeter:

1. The antineutron shower yields an incomplete measurement of its energy and an accurate measurement of its direction. We use the antineutron shower energy to select candidates, but cannot use this energy when reconstructing the B candidate. We can use the well-measured shower direction.

2. Antineutrons frequently annihilate with matter in the calorimeter. Since antineutron annihilation showers have distinctive characteristics that enable us to separate them from other showers, we use these characteristics to select them.
3. By baryon number conservation, if the event has an antineutron, it must have a corresponding baryon. In an exclusive reconstruction, as is ours, the selection of an proton increases the probability of there being an antineutron in the event substantially due to baryon number conservation. In addition, once we have selected a D^* , only shower candidates within a narrow momentum cone can be selected in the event.

We refer the reader to other studies of baryon-antibaryon annihilation [43, 44].

In Table 3.7 we outline the types of showers encountered in a hadronic event.

Table 3.7: Shower types and energy measured in calorimeter

Particle	Shower type	Energy measured
$\mu^\pm, \pi^\pm, K^\pm, p^\pm$	minimum ionizing	small fraction
e^\pm, γ	electromagnetic	full measurement
K_L	soft annihilation	small fraction
neutron	small electromagnetic	very small fraction
\bar{p} and \bar{n}	medium to hard annihilation	small fraction

We are limited by the absence of an independent antineutron sample that we can study to define our selection criteria. However, antiprotons also annihilate with nucleons in the calorimeter. Therefore, antiproton annihilation showers compose the shower sample in data and Monte Carlo which we use to define our antineutron

selection criteria as well as to gauge how well the Monte Carlo models antineutron annihilation showers.

3.7.1 Shower Parameters

We use the CCFC clustering package to select antineutron candidates. The CCFC shower package was not optimized to separate annihilation showers from other showers in the calorimeter. Nevertheless, we find that the parameters previously optimized to include photons, such as E9OE25, the list of nearby showers, and track-to-shower matching, are useful in excluding them as well.

The shower parameters used are:

1. E9OE25 < cut 1, a pre-determined value: E9OE25 has been defined in our discussion of π^0 's. It is very close to 1 for photons, and, we find, farthest from 1 for annihilation showers, overlapped π^0 's-which are not merged, but have the two photon showers very near each other, and K_L 's. An energy dependent cut, cut 1, on E9OE25, is applied to reject 99% of isolated photons.
2. NNESH: List of nearby showers (which does not include the shower to which the list belongs). The area encompassed increases with energy. It is in this list that we find showers near the antineutron that are most likely to be hadronic split-offs. We call the shower associated with the list the main shower, and sum the energy of it and all the others in NNESH, we call a group. In $B^0 \rightarrow D^{*-} p \bar{n}$ CLEO II signal MC, showers in the NNESH list are tagged to the parent shower in excess of 93 % of the time.

3. $|(\cos(\theta))|$: The calorimeter can be divided by polar angle θ into sections: good barrel, bad barrel, barrel/endcap overlap, bad endcap, good endcap, and near beampipe. We use the good barrel section throughout, which corresponds to $|(\cos(\theta))| < 0.71$.
4. Match level: The track to shower match levels in CCFC's NTRSH array are:
 - (a) Match level 1: shower center < 8 cm from the track projection.
 - (b) Match level 2: not level 1, but ≥ 1 member crystal
 - (c) Match level 3: not level 1 nor level 2.

We use match 3 showers for antineutron candidates and match 1 and 2 showers for antiprotons.

3.7.2 Antiproton Showers in Data

Lacking a sample of antineutrons to study in data which is independent of the sample we will use to measure $B^0 \rightarrow D^{*-} p \bar{n}$ and $B^0 \rightarrow D^{*-} p \bar{p} \pi^+$, we use antiproton annihilation showers which have been matched to a track. Antiprotons, like antineutrons, annihilate with matter in the calorimeter. The annihilation group of showers that results from this process has a distinctive signature: the antibaryon interaction is associated with a main shower, which has most of the energy of the annihilation, and the hadronic splitoffs from the interaction are associated with satellite showers near the point of interaction, each making a small contribution to the group energy.

In Figure 3.7 we plot shower energy E_{main} vs. signed momentum (PQCD) for protons and antiprotons, allowing all values of E9OE25, in the CLEO II data from

a D^* skim. Continuum and $B\bar{B}$ hadronic events are combined in this plot. The use of a D^* skim is a result of convenience.

The selection criteria used to generate Figure 3.7 is as follows:

1. $|PQCD(track)| > 300$ MeV.
2. $L_{proton} > 0.9$.
3. Track-to-shower match level 1.
4. $|\sigma_{dE/dx,electron}| > 2.2$ to reject electron fakes.
5. $|(cos(\theta))| < 0.71$: good barrel.
6. All values of E9OE25 allowed.

In Figure 3.8 we use the same selection criteria as was used for Figure 3.7 with the exception of a rejection cut, $E9OE25 < \text{cut } 1$, to suppress non-annihilation showers. The antiproton annihilation showers are typically those with $E_{main} > 300$ MeV and in the track momentum range 500 MeV to 900 MeV. Note that for these showers there is only a loose correlation between the reconstructed energy of the shower and the momentum of the antiproton that produced it. We can identify an annihilation shower, but have a very poor measurement of the momentum of the particle that produced it.

The horizontal line at shower energy 200 MeV, sloping upwards at PQCD 1 GeV, corresponds to minimum ionizing protons and antiprotons. The rest of this

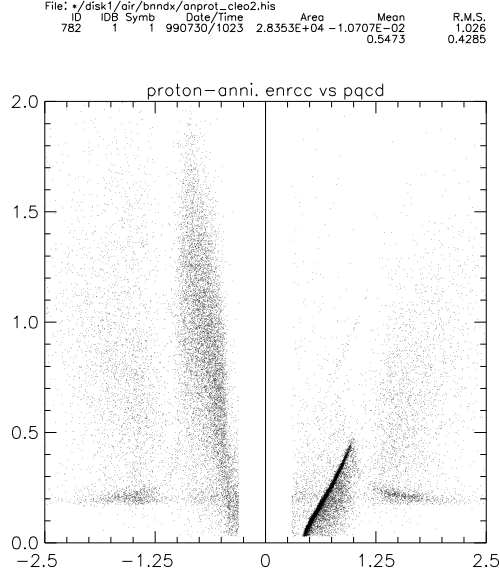


Figure 3.7: E_{main} vs. PQCD for protons and antiprotons in CLEO II

line in the lower momentum range corresponds to minimum ionizing pions. In the case of protons, before an E9OE25 cut is applied, the diagonal line corresponds to protons captured in the calorimeter. 1.0 GeV momentum is the threshold for this capture. Neutrons, analogously to protons, do not annihilate, and, since we have neither momentum information nor distinguishable showers, the study of B decays with neutrons is beyond CLEO's capabilities.

3.7.3 Antineutron Selection Criteria

Using antiproton annihilation showers, we devise the antineutron selection criteria to be used when reconstructing $B^0 \rightarrow D^{*-} p \bar{n}$, as shown in Table 3.8. Although this selection criteria allows a shower to have no nearby daughters, in which case $E_{main} = E_{group}$, the majority of antineutron showers have at least one

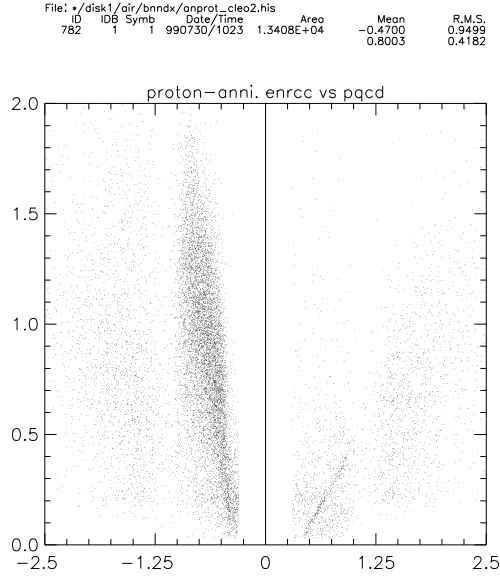


Figure 3.8: E_{main} vs. PQCD for protons and antiprotons in CLEO II

nearby daughter in Monte Carlo, as well as in our exclusively reconstructed B^0 signal events.

Table 3.8: Antineutron shower selection criteria.

Track-to-shower match level 3
$E_{9OE25} < \text{cut } 1$
$ \cos(\theta_{shower}) < 0.71$
$E_{main} > 500 \text{ MeV}$
$E_{group} > 800 \text{ MeV}$

We test this selection criteria in a generic $B\bar{B}$ Monte Carlo before and after the requirement that there be a proton with $|PQCD(track)| > 300 \text{ MeV}$ and $L_{proton} > 0.9$ in the event. The generic Monte Carlo sample is discussed in Section 3.2. In

Table 3.9 we show the results before and after applying the antineutron selection criteria cuts for a sample before the proton requirement is applied.

Table 3.9: Shower population in a generic $B\bar{B}$ Monte Carlo sample without proton requirement

Shower type	Annihilation cuts without E_{group} cut	Annihilation cuts with $E_{group} > 800$ MeV
γ from π^0	44.5	46.2
K_L	33.0	22.2
\bar{p}	0.5	0.6
π^\pm, K^\pm	3.3	1.9
other(ω ,etc)	1.4	1.3
\bar{n}	17.3	27.8
TOTAL	100.0	100.0

According to our generic Monte Carlo simulation, even before a proton requirement is applied 27.8% of the annihilation-like showers in a $B\bar{B}$ event are antineutrons. We next apply the proton requirement to a generic $B\bar{B}$ Monte Carlo sample. The results are shown in Table 3.10.

Table 3.10: Shower population in a generic $B\bar{B}$ Monte Carlo sample with proton requirement

Shower type	Annihilation cuts without E_{group} cut	Annihilation cuts with $E_{group} > 800$ MeV
γ from π^0	16.3	11.4
K_L	9.5	3.9
\bar{p}	2.7	1.8
π^\pm, K^\pm	2.0	0.9
other(ω ,etc)	0.7	0.5
\bar{n}	68.8	81.5
TOTAL	100.0	100.0

The above results are not surprising: use of baryon number conservation by selecting a proton increases the probability of an event having an antineutron from a few % to 50 %, while leaving all other annihilation like backgrounds at near the same level. Use of E_{group} cut reduces K_L contribution by 1/3 in the Non-baryon sample and by 1/2 in the baryon sample.

3.7.4 Antineutron Backgrounds

In Figures 3.9 and 3.10 we compare the shower energy spectrum of each of the two major backgrounds to antineutrons- γ from π^0 's, and K_L -to that of antineutrons. All antineutron selection criteria cuts, including $E_{group} > 800$ MeV, have been applied. Figure 3.9 is for case before proton requirement has been applied, and Figure 3.10 is for the case after proton requirement has been applied. The sample is, again, generic $B\bar{B}$ Monte Carlo. The backgrounds that have not been included make up (4.3,3.0) % of the (before,after) proton requirement distributions. In Figure 3.9 the solid distribution is for \bar{n} 's, the slanted lines distribution is for γ 's from π^0 's, and the white distribution is for K_L 's.

In Figure 3.10 the white distribution is for \bar{n} 's, the solid distribution is for γ 's from π^0 's, and the slanted lines distribution is for K_L 's. The large contamination in the low range of the E_{main} spectrum, as shown in Figure 3.9 and Figure 3.10 does not affect $B^0 \rightarrow D^{*-} p \bar{n}$ since for this B meson mode the antineutron shower energy spectrum is dominantly in the range $1.0 < E_{main} < 1.5$ GeV.

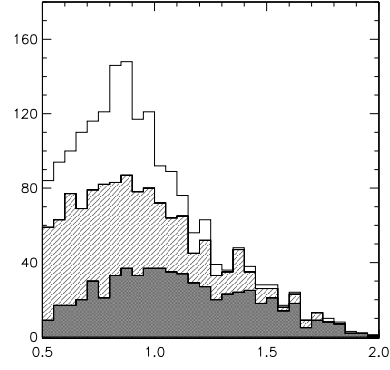


Figure 3.9: E_{main} in GeV without proton requirement for \bar{n} 's, γ 's from π^0 's, and K_L 's

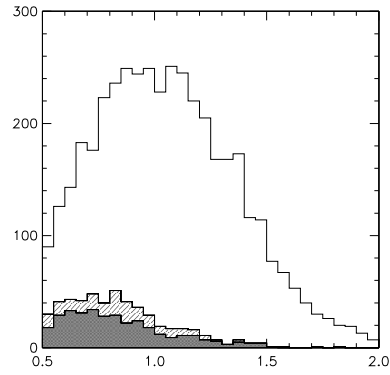


Figure 3.10: E_{main} in GeV with proton requirement for \bar{n} 's, γ 's from π^0 's, and K_L 's

CHAPTER 4

MEASUREMENT OF $B^0 \rightarrow D^{*-} P \bar{P} \pi^+$

Modes in $B \rightarrow [D] N \bar{N} X$ have not been previously measured. The reconstruction efficiency multiplied by the number of B mesons in our dataset for $B^0 \rightarrow D^{*-} p \bar{p} \pi^+$ and $B^0 \rightarrow D^{*-} p \bar{n}$, assuming branching fractions similar to the ones measured for $B^+ \rightarrow \bar{\Lambda}_c p \pi^+$ and $B^0 \rightarrow \bar{\Lambda}_c p \pi^+ \pi^-$ [29], is at a level we can measure, which lends credibility to a search for both modes.

4.1 Monte Carlo Reliability

The reconstruction process at CLEO, as well as at all other high energy detectors, involves a reconstruction efficiency ϵ_{Data} . For any given B decay, only a fraction of the number present in the data can be partially or fully reconstructed. If x number of B decays in our data are $B \rightarrow \text{Baryons}$ decays, only $\epsilon_{Data} \times x$ are measured. In the case of $B \rightarrow pX$, for example, there is a significant contamination due to protons from beam gas interactions at the low end of the momentum spectrum which limits $B \rightarrow pX$ to be carried out using antiprotons only, and then multiplying the result by 2.

By tuning a wide range of parameters, the Monte Carlo simulation can be made to closely resemble the data, in which case the assumption $\epsilon_{Data} \approx \epsilon_{MC}$ is reasonable. ϵ_{MC} is reliable because several processes which are measured at CLEO allow considerable ease of simulation as well as large samples which can be reliable

separated from backgrounds. Processes such as $e^+e^- \rightarrow e^+e^-$, $e^+e^- \rightarrow \mu^+\mu^-$, $e^+e^- \rightarrow \pi^+\pi^-$, $e^+e^- \rightarrow \gamma\gamma$, and $e^+e^- \rightarrow \gamma\gamma\gamma$ allow very accurate Monte Carlo modeling of individual particles, which in turn can be combined to model many B decays well.

On this level of accuracy a second group of decays is studied to widen the scope of our simulation: $K_S \rightarrow \pi^+\pi^-$, $\phi \rightarrow K^+K^-$, $D^* \rightarrow D^0\pi_{soft}$ with $\bar{D}^0 \rightarrow K^+\pi^-$, and $\Lambda \rightarrow p\pi$ all have very low backgrounds. Many particle separation studies are based on these decays. An example is the use of a low background sample of $\bar{\Lambda}$'s to study antiproton annihilation showers, as will be discussed later in this chapter.

4.2 Reconstruction Procedure

B mesons are produced with ≈ 300 MeV momentum at CLEO, which implies that E_{beam} is very close to E_B . This momentum is small when compared with the B meson mass of 5.28 GeV. Since the beam energy at CLEO is measured with a 2 MeV resolution, we can constraint the mass of the B meson candidate to be equal to the beam energy E_{beam} . We therefore use the beam constrained mass when reconstructing $B^0 \rightarrow D^{*-} p \bar{p} \pi^+$:

$$M_{BC} = \sqrt{E_{beam}^2 - \sum_i^3 p_i^2}$$

where E_{beam} is the beam energy, on average 5.29 GeV, and $\sum_i^3 p_i^2$ is the sum of daughter momenta squared.

The energy difference between the beam energy and the energy of the reconstructed B candidate, defined by:

$$\Delta_E = E_{beam} - E_{reconstructed B}$$

is centered at 0 and has a Gaussian width similar to the M_{BC} Gaussian width, whereas background events are much more likely to form a random distribution in Δ_E . Selecting B candidates using Δ_E cuts based on the Monte Carlo is useful in separating signal from background. As modelled by our Monte Carlo Δ_E for $B^0 \rightarrow D^{*-} p \bar{p} \pi^+$ is centered near zero and has a Gaussian width $\sigma < 100$ MeV, which allows us to separate the signal from backgrounds that differ by a miss-measured extra pion. The methodology we use in measuring $B^0 \rightarrow D^{*-} p \bar{p} \pi^+$ is analogous to that used in previous exclusive reconstructions at CLEO [45, 46].

4.3 Monte Carlo Study

In order to find the detector efficiency for the reconstruction of the modes we are searching for, we generate Monte Carlo in which one of the B mesons in the event is forced to decay to the mode we are reconstructing. We refer to this sample as signal Monte Carlo. In this signal Monte Carlo B mesons decay according to phase space.

We also use a sample of generic Monte Carlo $B\bar{B}$ events on which we run the $B^0 \rightarrow D^{*-} p \bar{p} \pi^+$ analysis code. The generic sample is composed of the B decays that have previously been measured as well as randomly generated events assuming inclusive momentum distributions. There are no $B \rightarrow [D]N\bar{N}X$ modes in the generic Monte Carlo sample. We use the generic Monte Carlo sample to model our backgrounds due to modes of the D^0 we are not reconstructing.

Applying the particle selection criteria outlined in Chapter 3 for the $B^0 \rightarrow D^{*-} p \bar{p} \pi^+$ decay daughters, we fit the ΔE distribution to a single Gaussian for signal and a 1st order Chebyshev polynomial for background. We show in Table 4.1 and Table 4.2 the result of these fits.

Table 4.1: ΔE fit results for $B^0 \rightarrow D^{*-} p \bar{p} \pi^+$ signal MC in CLEO II

Decay mode	Central value (MeV)	σ (MeV)	ΔE cut (MeV)
$D^0 \rightarrow K^+ \pi^-$	0.6	11.8	± 35
$\bar{D}^0 \rightarrow K^+ \pi^- \pi^0$	-2.3	16.8	± 50
$\bar{D}^0 \rightarrow K^+ \pi^- \pi^+ \pi^-$	1.1	9.8	± 29

Table 4.2: ΔE fit results for $B^0 \rightarrow D^{*-} p \bar{p} \pi^+$ signal MC in CLEO II.5

Decay mode	Central value (MeV)	σ (MeV)	ΔE cut (MeV)
$D^0 \rightarrow K^+ \pi^-$	-1.0	9.8	± 29
$\bar{D}^0 \rightarrow K^+ \pi^- \pi^0$	-3.1	13.4	± 40
$\bar{D}^0 \rightarrow K^+ \pi^- \pi^+ \pi^-$	-1.6	6.1	± 18

We define mode/dataset specific ΔE cuts which are applied to M_{BC} . The M_{BC} distribution is then fitted to a single Gaussian to determine each ϵ_{MC} , as shown in Table 4.3 and Table 4.4.

Table 4.3: M_{BC} distribution fit results for $B^0 \rightarrow D^{*-} p \bar{p} \pi^+$ signal MC in CLEO II

Decay mode	ϵ_{MC} (%)	σ (MeV)
$\bar{D}^0 \rightarrow K^+ \pi^-$	8.69 ± 0.21	2.63
$\bar{D}^0 \rightarrow K^+ \pi^- \pi^0$	4.48 ± 0.15	2.86
$\bar{D}^0 \rightarrow K^+ \pi^- \pi^+ \pi^-$	3.89 ± 0.14	2.65

Table 4.4: M_{BC} distribution fit results for $B^0 \rightarrow D^{*-} p \bar{p} \pi^+$ signal MC in CLEO II.5

Decay mode	ϵ_{MC} (%)	σ (MeV)
$\bar{D}^0 \rightarrow K^+ \pi^-$	4.32 ± 0.22	2.55
$\bar{D}^0 \rightarrow K^+ \pi^- \pi^0$	1.88 ± 0.14	2.60
$\bar{D}^0 \rightarrow K^+ \pi^- \pi^+ \pi^-$	1.05 ± 0.08	2.50

The π_{soft} in $D^* \rightarrow D^0 \pi_{soft}$ for the CLEO II.5 dataset is the most sensitive particle to errors in our Monte Carlo simulation. The replacement of the PTL detector by the SVX detector decreased by approximately a factor of 2 the reconstruction efficiency for the π_{soft} 's used here, and may have introduced a systematic uncertainty.

4.4 Results in Data

In Figure 4.1 and Figure 4.2 we show the ΔE vs M_{BC} distribution for $B^0 \rightarrow D^{*-} p \bar{p} \pi^+$ in, respectively, CLEO II and CLEO II.5. In Figure 4.3 and Figure 4.4 we show the M_{BC} distribution for $B^0 \rightarrow D^{*-} p \bar{p} \pi^+$ in, respectively, CLEO II and CLEO II.5, after the mode dependent ΔE cuts have been applied. The mode-by-mode M_{BC} distributions are combined for each of Figure 4.3 and Figure 4.4, in which (dark) events are from continuum. The continuum background to $B^0 \rightarrow D^{*-} p \bar{p} \pi^+$ is statistically insignificant. If this had not been the case, continuum subtraction would have been necessary to subtract this background from the M_{BC} distribution.

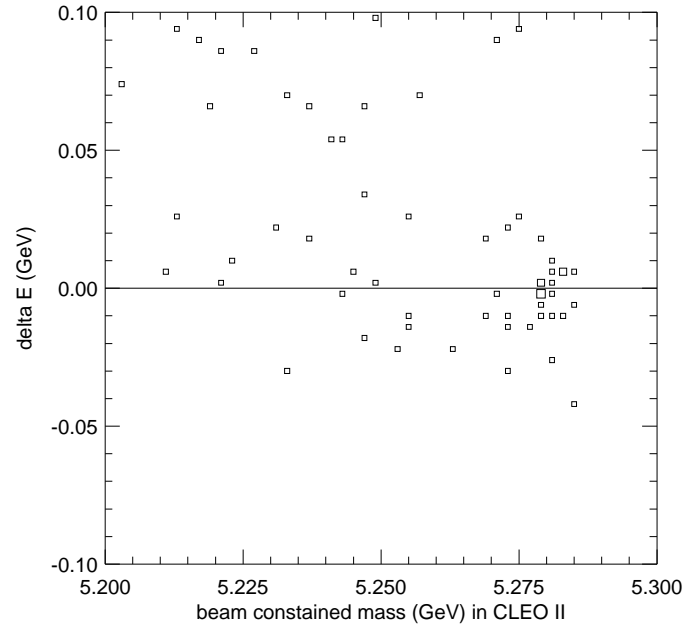


Figure 4.1: ΔE vs M_{BC} distribution for $B^0 \rightarrow D^{*-} p \bar{p} \pi^+$ in CLEO II ON resonance data.

Figure 4.2: ΔE vs M_{BC} distribution for $B^0 \rightarrow D^{*-} p \bar{p} \pi^+$ in CLEO II.5 ON resonance data

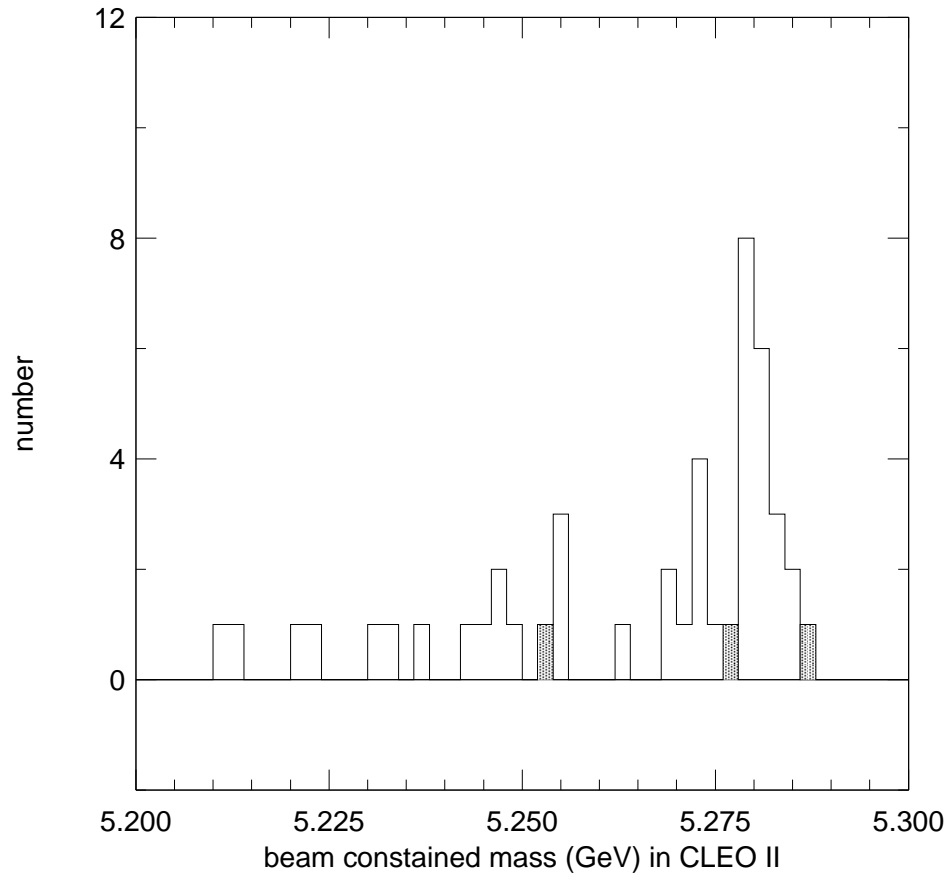


Figure 4.3: M_{BC} (in GeV) for $B^0 \rightarrow D^{*-} p \bar{p} \pi^+$ in CLEO II

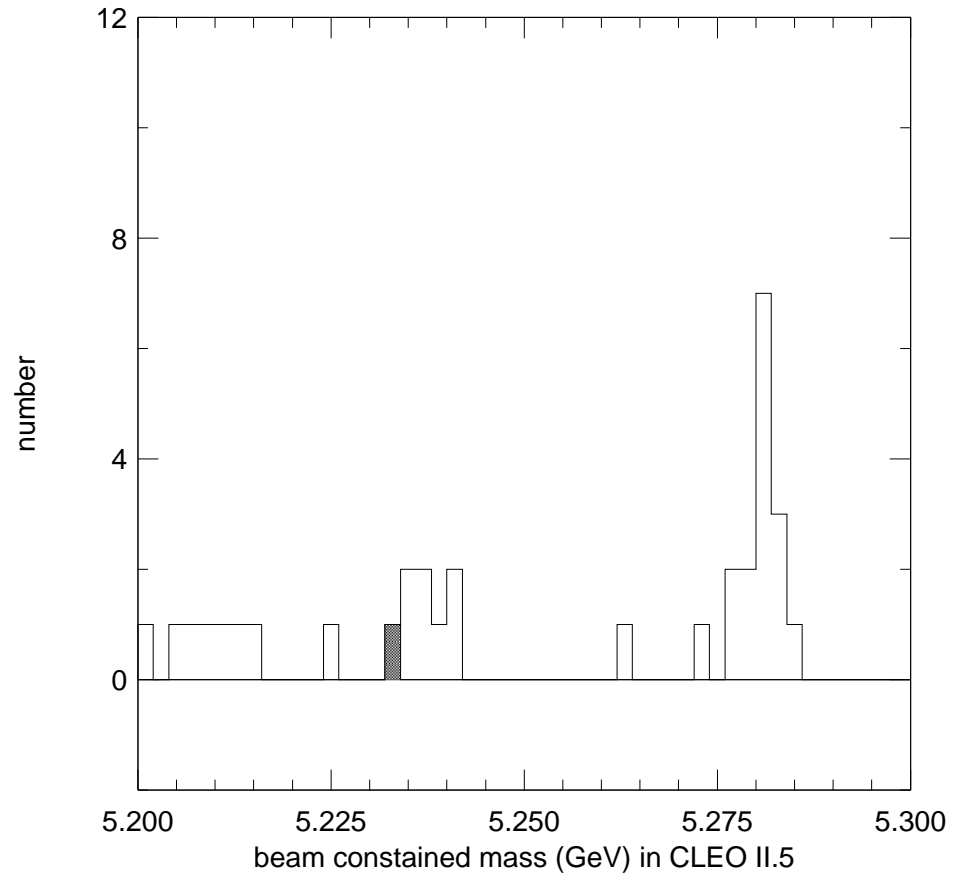


Figure 4.4: M_{BC} (in GeV) for $B^0 \rightarrow D^{*-} p \bar{p} \pi^+$ in CLEO II.5.

In Table 4.5 we attempt various fits to the combined CLEO II and CLEO II.5 M_{BC} distribution for $B^0 \rightarrow D^{*-} p \bar{p} \pi^+$:

1. Allowing M_{BC} and $\sigma_{M_{BC}}$ to float.
2. Fixing $M_{BC} = 5.28$ GeV and allowing $\sigma_{M_{BC}}$ to float.
3. Allowing M_{BC} to float and fixing $\sigma_{M_{BC}}$ according to expectations from signal MC.
4. Fixing both M_{BC} and $\sigma_{M_{BC}}$ as prescribed in 2. and 3. above.

The result of these fits are shown in Table 4.5. The variation in yield is small.

Table 4.5: Results in the CLEO II/II.5 data of various fits to M_{BC} for $B^0 \rightarrow D^{*-} p \bar{p} \pi^+$

fitting options:	fit results
floating values	
M_{BC} (in MeV)	$5,280.7^{+0.43}_{-0.45}$
σ (in MeV)	$2.05^{+0.43}_{-0.33}$
Fit yield	$30.52^{+6.55}_{-5.92}$
fixed M_{BC}	
σ (in MeV)	$2.40^{+0.69}_{-0.53}$
Fit yield	$31.88^{+7.34}_{-6.54}$
fixed σ	
M_{BC} (in MeV)	$5,280.5^{+0.55}_{-0.56}$
σ (in MeV)	2.65
Fit yield	$32.44^{+6.68}_{-6.02}$
fixed M_{BC} and σ	
Fit yield	$32.98^{+6.75}_{-6.02}$
$\mathcal{B}(B^0 \rightarrow D^{*-} p \bar{p} \pi^+) \times 10^{-4}$	$6.6^{+1.3}_{-1.2}$

$\mathcal{B}(B^0 \rightarrow D^{*-} p \bar{p} \pi^+)$ is calculated using:

$$\mathcal{B}(B^0 \rightarrow D^{*-} p \bar{p} \pi^+) = \frac{FittedYield}{(2 \times B^0 B^0 \times \epsilon_{MC})_{CLEOII} + (2 \times B^0 B^0 \times \epsilon_{MC})_{CLEOII.5}}$$

The product $(B\bar{B} \times \epsilon_{MC})_{CLEOII}$ is \approx the product $(B\bar{B} \times \epsilon_{MC})_{CLEOII.5}$. The number of events for $M_{BC} > 5.275$ GeV is 21 for CLEO II, and 15 for CLEO II.5. Fitting each dataset separately would yield a measurable $\mathcal{B}(B^0 \rightarrow D^{*-} p \bar{p} \pi^+)$.

In table 4.6 we quote the number of background events in the range $5.2 \text{ GeV} < M_{BC} < 5.275 \text{ GeV}$, and the number of signal events for $M_{BC} > 5.275 \text{ GeV}$. The D^0 mode with the largest background is $\bar{D}^0 \rightarrow K^+ \pi^- \pi^0$. Signal region contains $\approx 10 \%$ background events.

Table 4.6: $B^0 \rightarrow D^{*-} p \bar{p} \pi^+$: number of events found per mode

Mode	Background region CLEO II	Signal region CLEO II	Background region CLEO II.5	Signal region CLEO II.5
$D^0 \rightarrow K^+ \pi^-$	7	6	0	6
$\bar{D}^0 \rightarrow K^+ \pi^- \pi^0$	14	10	15	6
$\bar{D}^0 \rightarrow K^+ \pi^- \pi^+ \pi^-$	4	5	3	3

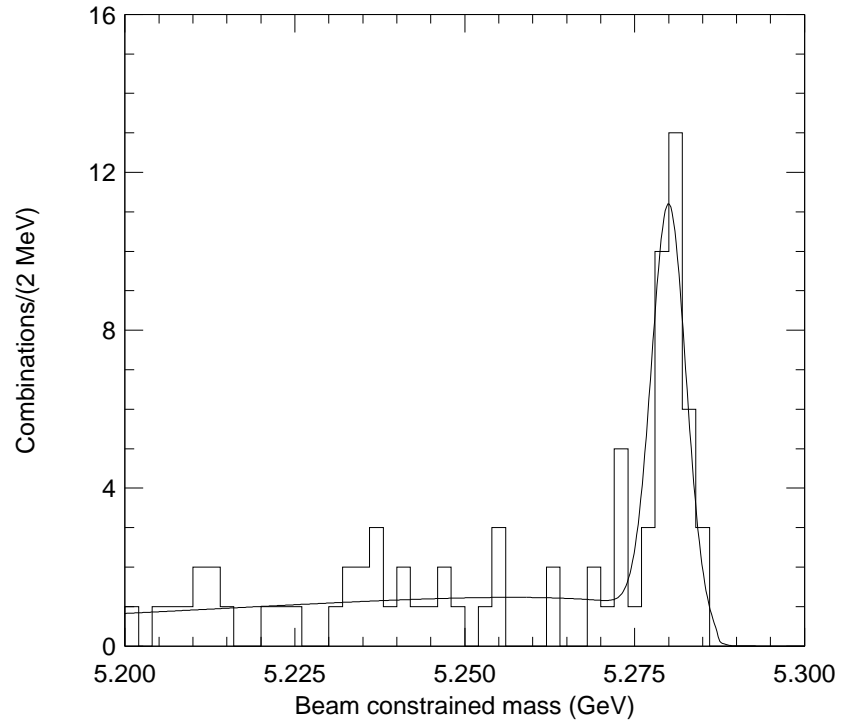


Figure 4.5: M_{BC} for $B^0 \rightarrow D^{*-} p \bar{p} \pi^+$ in data

We find the ΔE distribution for $B^0 \rightarrow D^{*-} p \bar{p} \pi^+$, as shown in Figure 4.6 to be Gaussian, as expected from signal MC. We also find the momentum spectrum for π_s from the D^* decay, as shown in Figure 4.7, to agree with expectations from signal MC and to be very soft. In Figure 4.7 the solid distribution is CLEO II Monte Carlo and the dashed distribution is CLEO II/II.5 data. Only events with $M_{BC} > 5.27$ are plotted for both figures.

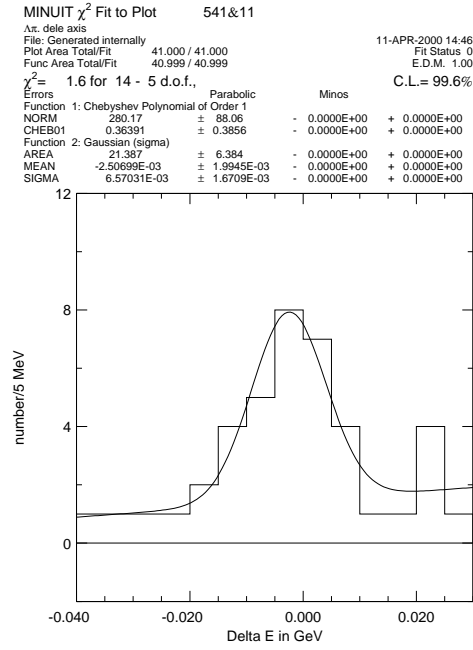


Figure 4.6: ΔE (in GeV) for $B^0 \rightarrow D^{*-} p \bar{p} \pi^+$ in CLEO II/II.5 data

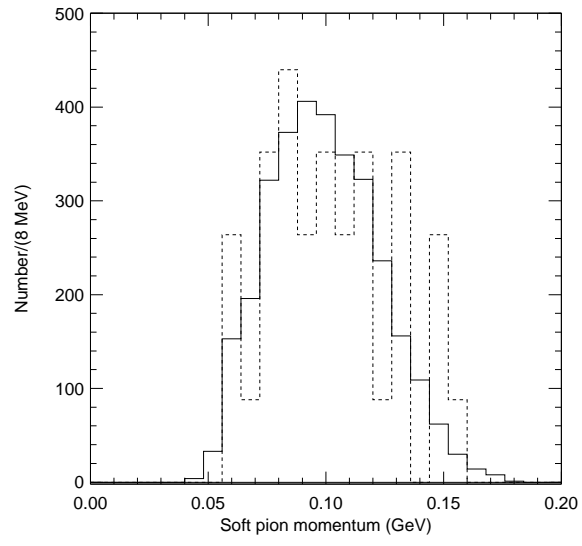


Figure 4.7: π_s from D^* momentum for $B^0 \rightarrow D^{*-} p \bar{p} \pi^+$ in data and Monte Carlo

4.5 Resonant Substructure

In order to determine whether we are using the correct ϵ_{MC} to measure $\mathcal{B}(B^0 \rightarrow D^{*-} p \bar{p} \pi^+)$, we need to know if we are measuring $B^0 \rightarrow D^{*-} p \bar{p} \pi^+$ or a mode with intermediate particles decaying to the same combination of decay daughters. We therefore search for possible contributions to the resonant substructure of $B^0 \rightarrow D^{*-} p \bar{p} \pi^+$. Any measurable resonant substructure would have to be subtracted from the inclusive measurement of $\mathcal{B}(B^0 \rightarrow D^{*-} p \bar{p} \pi^+)$, and the ϵ_{MC} would likewise have to be adjusted.

4.5.1 Two-body Decay and Possible Strong Resonances

We search for two types of resonances:

1. A heavy charmed baryon decaying strongly to $\bar{p} + D^{*-}$. No significant peaking is observed.
2. A resonance of the virtual W decaying to $p\bar{p}\pi^+$, $B^0 \rightarrow D^{*-} p \bar{p} \pi^+$ being a two body decay. No significant peaking is observed.

We study the $M_{p+\bar{p}+\pi^+}$ spectrum in data to check if it is consistent with phase space or two-body decay. For the two-body sample we generate MC with a fictitious heavy particle that decays to $p\bar{p}\pi^+$ for $B^0 \rightarrow D^{*-} p \bar{p} \pi^+$. It has a mass of 2.6 GeV and a width of 200 MeV.

No conclusive evidence is found for a measurable contribution to $\mathcal{B}(B^0 \rightarrow D^{*-} p \bar{p} \pi^+)$ from these possible contributions. The ϵ_{MC} for $B^0 \rightarrow D^{*-} p \bar{p} \pi^+$ varies slightly depending on the resonance substructure. We allow a 5% systematic uncertainty to account for these variations.

4.5.2 Δ Baryon Contributions in the Form of $B^0 \rightarrow D^{*-} \bar{p} \Delta^{++}$ and $B^0 \rightarrow D^{*-} p \bar{\Delta}^0$

Only the non-resonant $B^0 \rightarrow D^{*-} p \bar{p} \pi^+$ ϵ_{MC} 's are shown in table 4.5.2. The ϵ_{MC} does not vary by more than 5 % for any of the three possible assumptions: $B^0 \rightarrow D^{*-} p \bar{p} \pi^+$, $B^0 \rightarrow D^{*-} \bar{p} \Delta^{++}$, and $B^0 \rightarrow D^{*-} p \bar{\Delta}^0$. Any contribution from the latter two would imply a lumping of events in the 1.0 to 1.3 GeV range for $M_{p\pi^+}$ or $M_{\bar{p}\pi^+}$. The % makeup of $M_{p\pi^+}$ and $M_{\bar{p}\pi^+}$ is nearly identical in Monte Carlo, and we quote only the former. There are 41 events in data in signal region.

Table 4.7: % composition of generated (phase space MC) and events reconstructed (data) of $M_{p\pi^+}$ and $M_{\bar{p}\pi^+}$

Mass in GeV	Signal MC (%)	Data $M_{p\pi^+}$	%	Data $M_{\bar{p}\pi^+}$	%
1.0 - 1.1	7.1 ± 2.1	0	0.0	2	4.9
1.1 - 1.2	11.2 ± 0.8	3	7.3	4	9.8
1.2 - 1.3	11.9 ± 0.7	8	19.5	7	17.1
1.3 - 1.4	11.4 ± 0.6	8	19.5	9	22.0
1.4 - 1.5	10.2 ± 0.6	11	26.8	7	17.1
1.5 - 1.6	9.2 ± 0.6	3	7.3	6	14.6
1.6 - 1.7	11.3 ± 0.6	3	7.3	3	7.3
1.7 - 1.8	6.4 ± 0.6	3	7.3	3	7.3

We place an upper limit of < 2 events for $M_{p\pi^+}$, and < 3 events for $M_{\bar{p}\pi^+}$ as contributions from $B^0 \rightarrow D^{*-} \bar{p} \Delta^{++}$, and $B^0 \rightarrow D^{*-} p \bar{\Delta}^0$ respectively. These upper limits are educated guesses, and **do not** have any effect on the systematic uncertainty of our measurement of $\mathcal{B}(B^0 \rightarrow D^{*-} p \bar{p} \pi^+)$, since our quoted value includes the resonant substructure. Our quoted systematic uncertainty allows for the possibility of Δ baryon contributions to the resonant substructure of $B^0 \rightarrow D^{*-} p \bar{p} \pi^+$.

4.6 Backgrounds

We use generic Monte Carlo, which is discussed in Section 3.2, to study possible backgrounds to $B^0 \rightarrow D^{*-} p \bar{p} \pi^+$. Several characteristics of $B^0 \rightarrow D^{*-} p \bar{p} \pi^+$ result in expected low backgrounds as well as an accurate Monte Carlo simulation:

1. $B^0 \rightarrow D^{*-} p \bar{p} \pi^+$ has a proton and an antiproton as decay daughters, the baryon-antibaryon constraint is strictly applied.
2. D^{*-} 's have low $B\bar{B}$ and continuum backgrounds.
3. The high combined mass of the decay daughters is an added suppressant of continuum backgrounds.

The ΔE cut suppresses modes of type $B^0 \rightarrow D^{*-} p \bar{p} \pi^+ X$, where X is any additional number of neutral and charged pions, but it does not suppress their combinatoric backgrounds. Since, as previously mentioned, $B \rightarrow [D]N\bar{N}X$ decays are not accounted for in the generic MC sample we study, it is reasonable to assume that if 75 % of the background in the range $5.2 \text{ GeV} < M_{BC} < 5.275 \text{ GeV}$ is not accounted for by the generic MC sample, the most likely source of this background is combinatoric background to $B \rightarrow [D]N\bar{N}X$ decays. The small amount of non- $B \rightarrow [D]N\bar{N}X$ background is shown as a solid filled region in Figure 4.8, in which filled overlay on data is combinatoric non- $B \rightarrow [D]N\bar{N}X$ background from generic MC.

Figure 4.8: M_{BC} in data and generic Monte Carlo for $B^0 \rightarrow D^{*-} p \bar{p} \pi^+$ (in GeV)

4.7 Systematic Uncertainties

In Table 4.8 we show the systematic uncertainties we consider to contribute significant errors to our measurement of $\mathcal{B}(B^0 \rightarrow D^{*-} p \bar{p} \pi^+)$. $B^0 \rightarrow D^{*-} p \bar{p} \pi^+$ has an average of 6.6 tracks.

Table 4.8: Estimate of systematic uncertainties (in %) for $B^0 \rightarrow D^{*-} p \bar{p} \pi^+$

Source	Uncertainty (in %)
D^0 branching fractions	0.6
D^* branching fraction	1.4
D^* reconstruction	5.0
Monte Carlo statistics	5.0
# of $B\bar{B}$'s	2.0
tracking (1%/track)	6.6
PRLEV proton ID	8.0
Δ signal contribution	5.0
Δ background contribution	5.0
Phase space versus two body	5.0
TOTAL	15.5 %

CHAPTER 5

MEASUREMENT OF $B^0 \rightarrow D^{*-} P \bar{N}$

As mentioned in Chapter 4, we have selected the $B \rightarrow [D]N\bar{N}X$ modes which are expected to have the lowest backgrounds as well as the highest reconstruction efficiency. When reconstructing $B^0 \rightarrow D^{*-} p \bar{n}$, however, we encounter a stumbling block not encountered in the reconstruction of $B^0 \rightarrow D^{*-} p \bar{p} \pi^+$ by virtue of the former mode having an antineutron-or a neutron in the case of its charge conjugate-as one of its decay daughters. Our inability to separate neutron showers from their backgrounds reduces the reconstruction efficiency for $B^0 \rightarrow D^{*-} p \bar{n}$ by 50%. The antineutron reconstruction efficiency, however, is sufficiently large (in the range of 30 to 40%). We do not have an accurate measurement of the antineutron energy, yet we do have a well measured direction of its shower, which we use to reconstruct $B^0 \rightarrow D^{*-} p \bar{n}$. The reconstruction method we use is analogous to that used in an unpublished reconstruction of $B \rightarrow J/\Psi K_L$ by CLEO [47]. In Table 5.1 we outline our antineutron selection criteria which we derived in Chapter 3.

Table 5.1: Antineutron shower selection criteria.

Track-to-shower match level type 3
E9OE25 < cut 1
$ \cos(\theta) < 0.71$, or good barrel
$E_{main} > 500$ MeV
$E_{group} > 800$ MeV

5.1 Reconstruction Procedure

Instead of M_{BC} , we define m_{B^0} , in which we set $\Delta E = 0$ and assign the missing energy to the antineutron using the directional cosines of its shower. Since the measured shower energy for an antineutron, even after summing the energy in the list of nearby showers, fails to match the total energy of the antineutron, we only use the electromagnetic shower energy as part of our selection criteria.

The reconstruction steps for this mode are:

1. $E_{\bar{n}} = E_{beam} - E_{D^*+p}$ is assigned to the antineutron. This energy difference is the equivalent of setting $\Delta E = 0$, or $E_{beam} = E_{reconstructed B}$.
2. 3-momentum magnitude of antineutron candidate $p_{\bar{n}} = \sqrt{E_{\bar{n}}^2 - m_{\bar{n}}^2}$, with $m_{\bar{n}} = 0.9395$ GeV.
3. 3-momentum magnitude of antineutron $p_{\bar{n}}$ times x,y,z directional cosines of shower energy are assigned to, respectively, x,y,z components of $p_{\bar{n}}$.
4. 4-momentum of B candidate $p_{B^0} = p_{\bar{n}} + p_{D^*} + p_{proton}$.
5. Mass of B candidate $m_{B^0} = \sqrt{E_{beam}^2 - p_{B^0}^2}$.

As in the $B^0 \rightarrow D^{*-} p \bar{p} \pi^+$ reconstruction, we use Monte Carlo samples in which the B meson decays according to phase space. The resonant substructure of $\bar{D}^0 \rightarrow K^+ \pi^- \pi^0$ is same as in $B^0 \rightarrow D^{*-} p \bar{p} \pi^+$.

5.2 $D_s^+ \rightarrow p \bar{n}$ in Monte Carlo

In reconstructing $B^0 \rightarrow D^{*-} p \bar{n}$ we can also be reconstructing $B^0 \rightarrow D_s^+ D^{*-}$ with $D_s^+ \rightarrow p \bar{n}$. The $B^0 \rightarrow D_s^+ D^{*-}$ with $D_s^+ \rightarrow p \bar{n}$ contribution is part of our signal, yet it is not a mode within the resonant substructure of $B^0 \rightarrow D^{*-} p \bar{n}$. It is a separate mode of the B meson with $\mathcal{B}(B^0 \rightarrow D_s^+ D^{*-}) = 9.6 \pm 3.4 \times 10^{-3}$ [5]. $D_s^+ \rightarrow p \bar{n}$, a Feynman diagram of which is shown in Figure 5.1. Yet another contribution which can be in the $M_{p+\bar{n}}$ distribution is $B^0 \rightarrow D_s^{*+} D^{*-}$ with $D_s^+ \rightarrow p \bar{n}$, which is a background. $\mathcal{B}(B^0 \rightarrow D_s^{*+} D^{*-}) = 2.0 \pm 0.7 \times 10^{-2}$ [5]. The effect of either on $B^0 \rightarrow D^{*-} p \bar{n}$ cannot be assessed accurately since we do not know $\mathcal{B}(D_s^+ \rightarrow p \bar{n})$. If we assume $\mathcal{B}(D_s^+ \rightarrow p \bar{n})$ is $\approx 1\%$, the effect on $B^0 \rightarrow D^{*-} p \bar{n}$ can be significant enough to affect our measurement of $\mathcal{B}(B^0 \rightarrow D^{*-} p \bar{n})$.

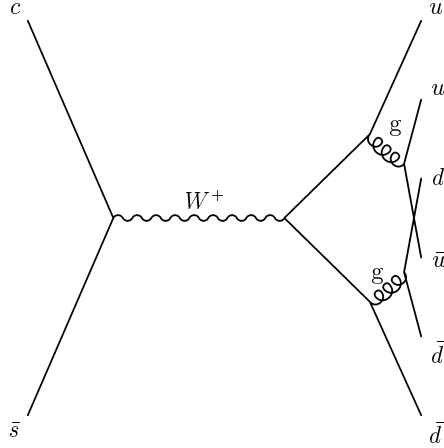


Figure 5.1: A Feynman diagram for $D_s^+ \rightarrow p \bar{n}$

The $M_{p+\bar{n}}$ distribution should not peak appreciably in $B^0 \rightarrow D^{*-} p \bar{n}$, and a narrow Gaussian peak with 5 MeV σ in $B^0 \rightarrow D_s^+ D^{*-}$ with $D_s^+ \rightarrow p \bar{n}$. The $D_s^+ \rightarrow p \bar{n}$ Monte Carlo peak for $B^0 \rightarrow D_s^+ D^{*-}$ is shown in Figure 5.2.

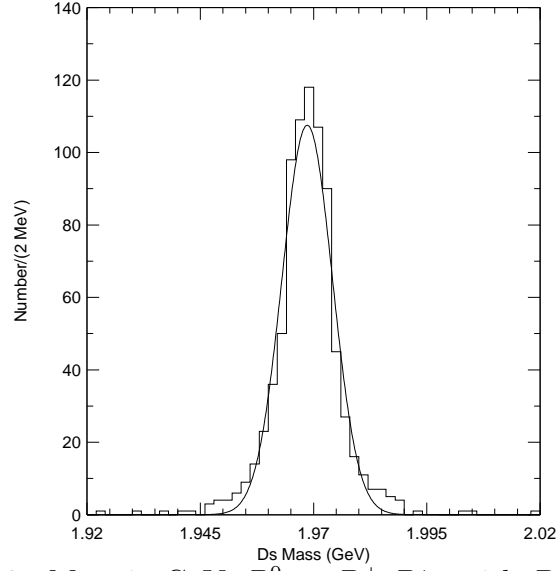


Figure 5.2: $M_{p+\bar{n}}$ in GeV. $B^0 \rightarrow D_s^+ D^{*-}$ with $D_s^+ \rightarrow p \bar{n}$

In Figure 5.3 we show the smeared $M_{p+\bar{n}}$ distribution resulting from reconstructing $B^0 \rightarrow D^{*-} p \bar{n}$ in a signal Monte Carlo $B^0 \rightarrow D_s^{*+} D^{*-}$ with $D_s^+ \rightarrow p \bar{n}$ sample. $D_s^{*+} \rightarrow D_s^+ \gamma = 1$. The missing soft photon will cause this background sample to be considerably broader than the $B^0 \rightarrow D_s^+ D^{*-}$ with $D_s^+ \rightarrow p \bar{n}$ signal contribution.

The $B^0 \rightarrow D_s^{*+} D^{*-}$ contribution is a background to $B^0 \rightarrow D^{*-} p \bar{n}$ as well as $B^0 \rightarrow D_s^+ D^{*-}$ with $D_s^+ \rightarrow p \bar{n}$. Our choice regarding how to deal with these contributions is to exclude both possible contributions ($B^0 \rightarrow D_s^+ D^{*-}$ with D_s^+

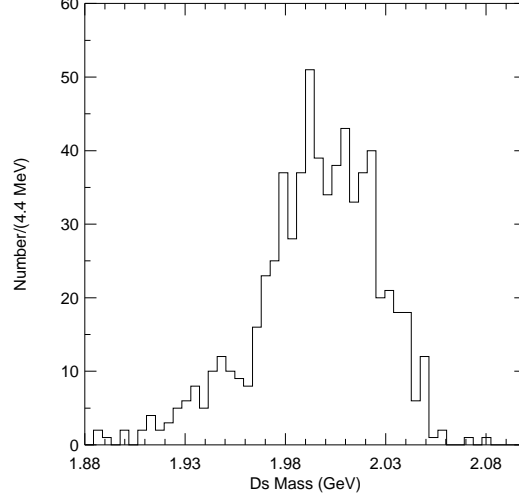


Figure 5.3: $M_{p+\bar{n}}$ (in GeV) from a reconstruction of $B^0 \rightarrow D^{*-} p \bar{n}$ in a signal Monte Carlo $B^0 \rightarrow D_s^{*+} D^{*-}$ with $D_s^+ \rightarrow p \bar{n}$

$\rightarrow p \bar{n}$ and $B^0 \rightarrow D_s^{*+} D^{*-}$ with $D_s^+ \rightarrow p \bar{n}$) in quoting our final value for $\mathcal{B}(B^0 \rightarrow D^{*-} p \bar{n})$.

Both $D_s^+ \rightarrow p \bar{n}$ contributions can be excluded with $1.91 \text{ GeV} < M_{p+\bar{n}} < 2.04 \text{ GeV}$. In Tables 5.2 and 5.3 we outline the ϵ_{MC} 's for $B^0 \rightarrow D^{*-} p \bar{n}$. These ϵ_{MC} 's take into consideration that we are not reconstructing the conjugate mode-with a neutron.

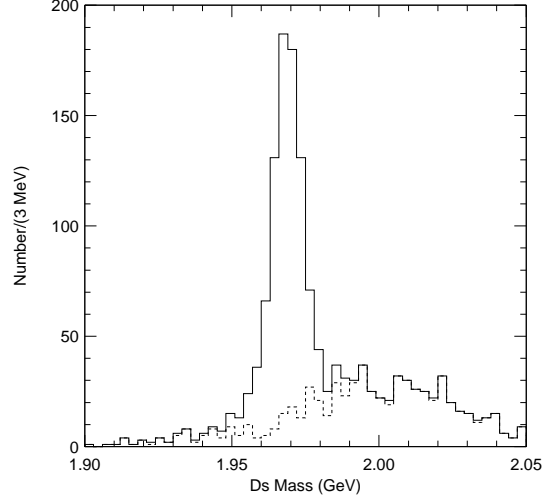


Figure 5.4: (white) is $B^0 \rightarrow D_s^+ D^{*-}$ with $D_s^+ \rightarrow p \bar{n}$. (dashed) is $B^0 \rightarrow D_s^{*+} D^{*-}$ with $D_s^+ \rightarrow p \bar{n}$. $M_{p+\bar{n}}$ (in GeV)

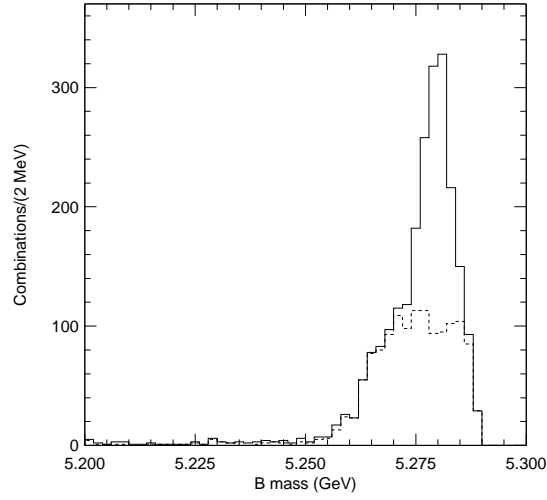


Figure 5.5: (white) is $B^0 \rightarrow D_s^+ D^{*-}$ with $D_s^+ \rightarrow p \bar{n}$. (dashed) is $B^0 \rightarrow D_s^{*+} D^{*-}$ with $D_s^+ \rightarrow p \bar{n}$. m_{B^0} (in GeV)

Table 5.2: $B^0 \rightarrow D^{*-} p \bar{n}$ signal MC ϵ_{MC} 's and widths in CLEO II.

Mode	%	MeV
both $D_s^+ \rightarrow p \bar{n}$ contributions excluded.		
$D^0 \rightarrow K^+ \pi^-$	7.47 ± 0.28	3.10
$\bar{D}^0 \rightarrow K^+ \pi^- \pi^0$	2.88 ± 0.17	3.40
$\bar{D}^0 \rightarrow K^+ \pi^- \pi^+ \pi^-$	3.33 ± 0.19	3.11
both $D_s^+ \rightarrow p \bar{n}$ contributions included, without any background correction.		
$D^0 \rightarrow K^+ \pi^-$	8.12 ± 0.32	3.14
$\bar{D}^0 \rightarrow K^+ \pi^- \pi^0$	3.09 ± 0.19	3.00
$\bar{D}^0 \rightarrow K^+ \pi^- \pi^+ \pi^-$	3.52 ± 0.20	3.05

Table 5.3: $B^0 \rightarrow D^{*-} p \bar{n}$ signal MC ϵ_{MC} 's and widths in CLEO II.5

Mode	%	MeV
Both $D_s^+ \rightarrow p \bar{n}$ contributions excluded.		
$D^0 \rightarrow K^+ \pi^-$	4.51 ± 0.17	2.95
$\bar{D}^0 \rightarrow K^+ \pi^- \pi^0$	1.60 ± 0.13	3.23
$\bar{D}^0 \rightarrow K^+ \pi^- \pi^+ \pi^-$	1.68 ± 0.14	2.79
Both $D_s^+ \rightarrow p \bar{n}$ contributions included, without any background correction.		
$D^0 \rightarrow K^+ \pi^-$	4.99 ± 0.18	2.92
$\bar{D}^0 \rightarrow K^+ \pi^- \pi^0$	1.82 ± 0.14	3.35
$\bar{D}^0 \rightarrow K^+ \pi^- \pi^+ \pi^-$	1.83 ± 0.15	2.78

5.3 Results in Data

We look for $B^0 \rightarrow D^{*-} p \bar{n}$ with or without the mass region $1.91 \text{ GeV} < M_{p+\bar{n}} < 2.04 \text{ GeV}$. We compare in Figure 5.6 these two cases in CLEO II/II.5.

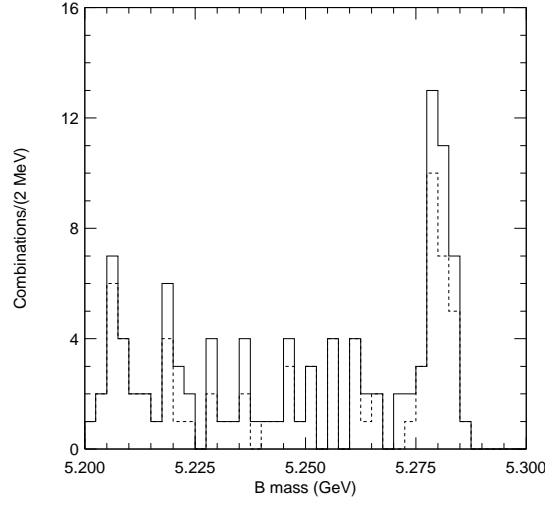


Figure 5.6: (white) is inclusive of all contributions. (dashed) is after exclusion of both $D_s^+ \rightarrow p \bar{n}$ contributions

The $B^0 \rightarrow D^{*-} p \bar{n}$ m_{B^0} distribution is less statistically significant without the $D_s^+ \rightarrow p \bar{n}$ contributions. However, the cost of lost events for the purposes of our measurement is warranted for the following reasons:

1. The signal events we are left with have an insignificant probability of being something other than $B^0 \rightarrow D^{*-} p \bar{n}$.
2. We properly account for the lost events in our ϵ_{MC} 's.

In Figure 5.7 we show m_{B^0} for ON resonance and OFF resonance for the case we use to quote $\mathcal{B}(B^0 \rightarrow D^{*-} p \bar{n})$: without both contributions.

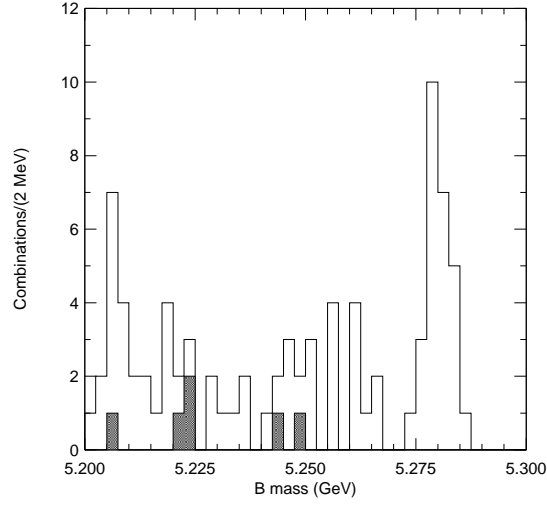


Figure 5.7: (white) is ON resonance, (solid) is OFF resonance

The number of OFF resonance events is not significant enough to affect our measurement. We choose not to subtract these from the ON resonance distribution.

In Figure 5.8 and Figure 5.9 we show m_{B^0} distributions by dataset.

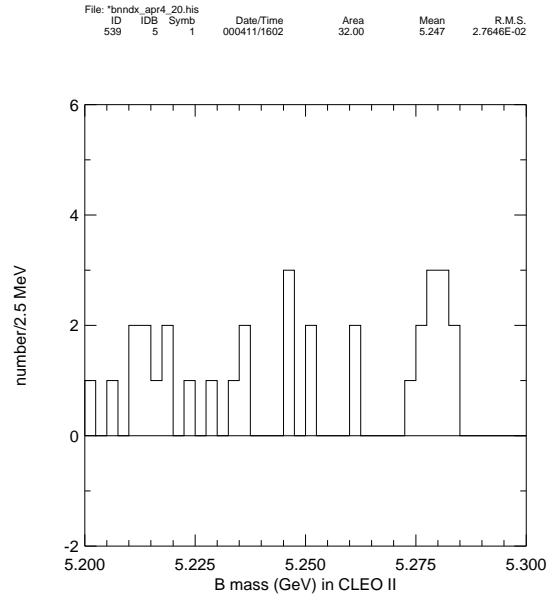


Figure 5.8: M_{B^0} for $B^0 \rightarrow D^{*-} p \bar{n}$ in CLEO II ON resonance data

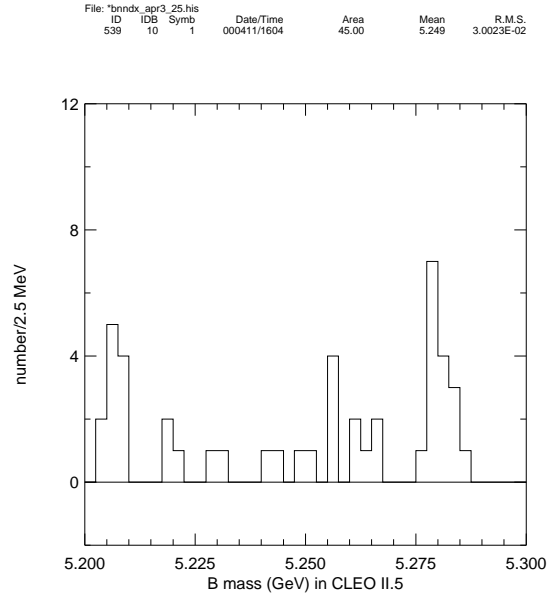


Figure 5.9: M_{B^0} for $B^0 \rightarrow D^{*-} p \bar{n}$ in CLEO II.5 ON resonance data

5.4 $D_s^+ \rightarrow p \bar{n}$ in Data

In Figure 5.10 we plot $M_{p+\bar{n}}$ for the region where we expect to see $D_s^+ \rightarrow p \bar{n}$ as a small width signal for $B^0 \rightarrow D_s^+ D^{*-}$, and as a shallow background for $B^0 \rightarrow D_s^{*+} D^{*-}$. The horizontal lines demarcate the mass region $1.91 \text{ GeV} < M_{p+\bar{n}} < 2.04 \text{ GeV}$, which we are excluding. Events with $m_{B^0} > 5.275 \text{ GeV}$ region are shown in Figure 5.10. The vertical lines demarcate the mass region $1.91 \text{ GeV} < M_{p+\bar{n}} < 2.04 \text{ GeV}$, which we are excluding. Not shown are events with $M_{p+\bar{n}} > 2.27 \text{ GeV}$. We expect to find $\approx 10\%$ of $B^0 \rightarrow D^{*-} p \bar{n}$ signal events in this region, which translates to 3 events.

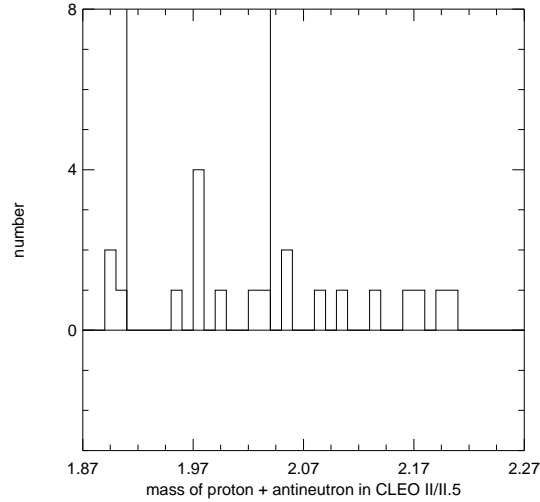


Figure 5.10: $M_{p+\bar{n}}$ for $B^0 \rightarrow D^{*-} p \bar{n}$ (in GeV) in CLEO II/II.5

We find 8 events where a $D_s^+ \rightarrow p \bar{n}$ signal is expected. This sample is not sufficiently significant to label these events as signal. The scatter plot in Figure 5.11 contains more information than Figure 5.10: there are other regions in this

plot that are equally statistically significant to the region where we expect to find $D_s^+ \rightarrow p \bar{n}$. If we are to claim a signal in one, we should be able to claim one in any of these others.

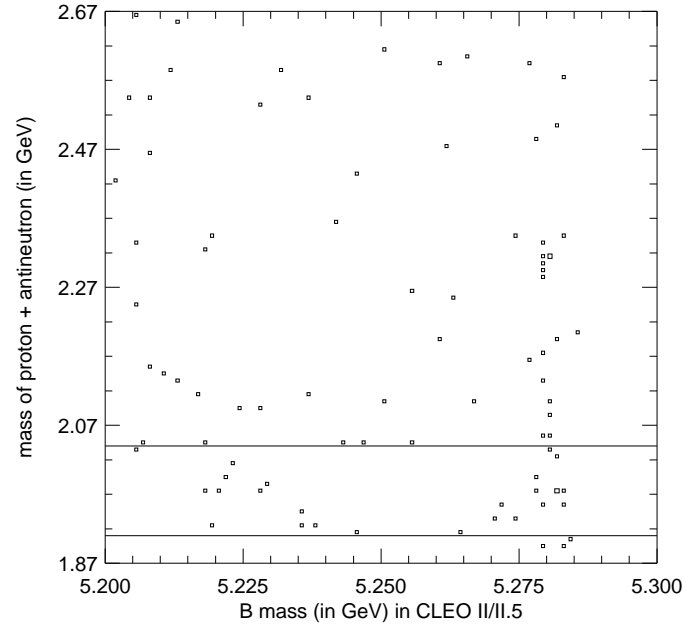


Figure 5.11: $M_{p+\bar{n}}$ vs. m_{B^0} (both in GeV)

We can, however, estimate an upper limit for $D_s^+ \rightarrow p \bar{n}$. The most conservative estimate is to call all 8 events in the expected region signal, which leads to a value of 11.5 for a 90% confidence level measurement. 11.5 signal events correspond to $\mathcal{B}(D_s^+ \rightarrow p \bar{n}) < 5.4\%$ using the PDG value for $\mathcal{B}(B^0 \rightarrow D_s^+ D^{*-})$.

5.5 $\mathcal{B}(B^0 \rightarrow D^{*-} p \bar{n})$ Measurements.

We use the same equation to calculate $\mathcal{B}(B^0 \rightarrow D^{*-} p \bar{n})$ as we did for $B^0 \rightarrow D^{*-} p \bar{p} \pi^+$:

$$\mathcal{B}(B^0 \rightarrow D^{*-} p \bar{p} \pi^+) = \frac{FittedYield}{(2 \times B^0 \bar{B}^0 \times \epsilon_{MC})_{CLEO II} + (2 \times B^0 \bar{B}^0 \times \epsilon_{MC})_{CLEO II.5}}$$

As we mentioned when calculating $\mathcal{B}(B^0 \rightarrow D^{*-} p \bar{p} \pi^+)$, the product $(B \bar{B} \times \epsilon_{MC})$ is almost the same for CLEO II and CLEO II.5. The number of events for this mode for $M_{BC} > 5.275$ GeV is 10 for CLEO II, and 16 for CLEO II.5.

The combined m_{B^0} distribution can be fitted to yield results that are consistent with Monte Carlo expectations.

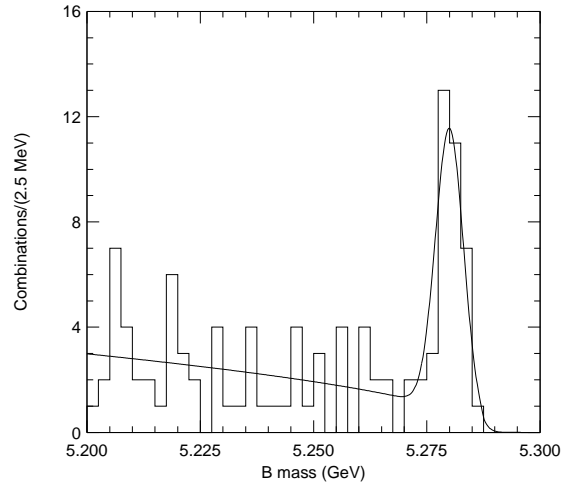


Figure 5.12: Inclusive m_{B^0} in data for $B^0 \rightarrow D^{*-} p \bar{n}$ (in GeV)

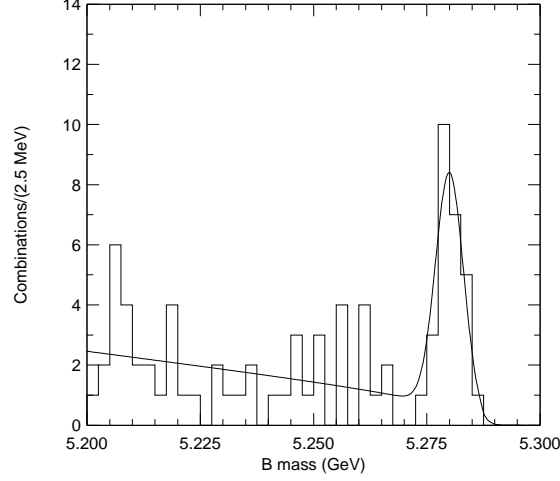


Figure 5.13: m_{B^0} in data for $B^0 \rightarrow D^{*-} p \bar{n}$ in GeV excluding both $D_s^+ \rightarrow p \bar{n}$ contributions

Table 5.4: Measurements of $B^0 \rightarrow D^{*-} p \bar{n}$ branching fractions

Mode	Yield	Branching Fraction
$B^0 \rightarrow D^{*-} p \bar{n}$ inclusive	$32.94^{+6.56}_{-5.92}$	$14.9^{+3.0}_{-2.7} \times 10^{-4}$
$B^0 \rightarrow D^{*-} p \bar{n}$ without both contributions	$24.02^{+5.60}_{-4.96}$	$11.9^{+2.8}_{-2.5} \times 10^{-4}$

The difference in branching fractions does not imply that what has been excluded is only $D_s^+ \rightarrow p \bar{n}$. We do not attempt to derive an upper limit by this method. As in the case of our measurement of $B^0 \rightarrow D^{*-} p \bar{p} \pi^+$, we find the $B^0 \rightarrow D^{*-} p \bar{n}$ signal events are consistent with phase space decay. We look for a resonance of type $(cud) + (d\bar{d})_{strong} \rightarrow \bar{n} + D^{*-}$, and fail to find it.

The fits are quoted in Table 5.5. m_{B^0} is fitted to a single Gaussian for signal, and an Argus function for background. The offset is fixed at 0.0025, and the E_{beam}

is fixed at 5.29 GeV in all the fits. As in the case of $B^0 \rightarrow D^{*-} p \bar{p} \pi^+$, in table 5.5, leaving some parameters fixed, but not others allows us to test the validity of our results. The excluded region is $1.91 \text{ GeV} < M_{p+\bar{n}} < 2.04 \text{ GeV}$.

Table 5.5: Results of various fits to m_{B^0} for $B^0 \rightarrow D^{*-} p \bar{n}$ with or without the $D_s^+ \rightarrow p \bar{n}$ contributions

Fitting options	No $D_s^+ \rightarrow p \bar{n}$	Inclusive
floating values		
m_{B^0} (MeV)	$5,280.3^{+0.60}_{-0.61}$	$5,280.5^{+0.50}_{-0.52}$
σ (MeV)	$2.59^{+0.49}_{-0.41}$	$2.43^{+0.46}_{-0.37}$
Fit Yield	$23.57^{+5.61}_{-4.97}$	$31.48^{+6.52}_{-5.86}$
fixed $m_{B^0} = 5.28 \text{ GeV}$		
σ (MeV)	$2.62^{+0.49}_{-0.42}$	$2.55^{+0.47}_{-0.40}$
Fit Yield	$23.67^{+5.62}_{-4.99}$	$31.97^{+6.57}_{-5.93}$
fixed $\sigma = 3.07 \text{ MeV}$		
m_{B^0} (in MeV)	$5,280.3^{+0.68}_{-0.67}$	$5,280.3^{+0.60}_{-0.60}$
Fit Yield	$23.97^{+5.60}_{-4.96}$	$32.75^{+6.56}_{-5.91}$
fixed m_{B^0} and σ		
Fit Yield	$24.02^{+5.60}_{-4.96}$	$32.94^{+6.56}_{-5.92}$
$\mathcal{B}(B^0 \rightarrow D^{*-} p \bar{n}) \times 10^{-4}$:		
From raw yield	$11.9^{+2.8}_{-2.5}$	$14.9^{+3.0}_{-2.7}$
With MC Correction Factor	$14.8^{+3.5}_{-3.1}$	$18.3^{+3.7}_{-3.3}$

In the following section we discuss the correction factor we apply to the raw $\mathcal{B}(B^0 \rightarrow D^{*-} p \bar{n})$ due to a discrepancy between data and Monte Carlo in the $\epsilon_{\bar{p}}$ for antiproton annihilation showers. The Correction Factor we use increases the raw $\mathcal{B}(B^0 \rightarrow D^{*-} p \bar{n})$ quoted in Table 5.5 by a factor of 1.21 with an added systematic uncertainty of 4%.

5.6 Correction Factor

The Monte Carlo we use has not been optimized to model nucleon-antinucleon annihilation. We find a discrepancy between the reconstruction efficiency for data and Monte Carlo for antiprotons. We consider the discrepancy credible and change the antineutron efficiency using a Correction Factor. We assume that the Monte Carlo fails to model antineutrons by the same amount as it does for antiprotons, even though the quark content of antiprotons and antineutrons is different.

We define $\epsilon_{annihilation}$ as the efficiency for an antibaryon shower to pass the annihilation shower cuts outlined in Table 3.8. This quantity will be different for antiprotons and antineutrons. In the former case we choose a sample which is inevitably biased by the momentum range in which we can separate antiprotons from other charged tracks. In the latter case we use a sample which has shower backgrounds.

We define a correction factor to account for the discrepancy between data and Monte Carlo for annihilation showers as:

$$\text{Correction Factor} = \frac{\epsilon_{annihilation,MC}}{\epsilon_{annihilation,Data}}$$

This Correction Factor is found for antiproton momentum bins in a range consistent with the momentum range of antineutrons in $B^0 \rightarrow D^{*-} p \bar{n}$ as found from the energy assigned to the antineutron candidate shower after assuming the antineutron mass. The number of antineutrons in each of these momentum bins is used to weigh the contribution of each bin to the Correction Factor, which is defined for the entire range.

5.7 Use of a $\bar{\Lambda}$ Sample

The selection of a clean sample of antiprotons is achieved by reconstructing $\bar{\Lambda}$'s. In the decay $\bar{\Lambda} \rightarrow \bar{p}\pi^+$, due to the large difference in mass between the \bar{p} and the π^+ , the kinematics of the decay allow for a clear separation of the \bar{p} tracks from the π^+ tracks. Furthermore, the single Gaussian width of the $m_{\bar{\Lambda}}$ distribution is 1 MeV and is affected by backgrounds insignificantly.

Antiprotons are selected with the same criteria used in the reconstruction of $B^0 \rightarrow D^{*-} p \bar{p} \pi^+$ except for the use of $L_{proton} > 0.1$. Λ 's are from the KNVF package [42]. The $\bar{\Lambda}$ selection criteria is as shown in Table 5.6.

Table 5.6: Λ selection criteria

Both tracks pass TRKMNG flag $tng(track) \geq 0$
χ^2 of two tracks to form a vertex ≤ 30
χ^2 for Λ to point back to the interaction region ≤ 30
Significance of the two dimensional flight distance $< 3\sigma$
Flight distance ≥ 0.005 meter

We count the number of Λ 's in the signal region after applying a double Gaussian fit with fixed parameters as shown in Table 5.7.

Table 5.7: Λ double Gaussian fixed parameters

Mass	1.1158 GeV
σ^1	0.00162
Area2/area1	0.46
Δ_{MEAN}	0
σ^2/σ^1	0.425

In Table 5.8 we find the % of antiproton showers in a Λ sample which pass the annihilation shower cuts. In Table 5.8 we find $\epsilon_{annihilation}$ for MC and Data $\bar{\Lambda}$ samples. The samples are a combination of ON and OFF resonance. The ON and OFF resonance $\epsilon_{annihilation}$'s were found to yield the same results.

Table 5.8: $\epsilon_{annihilation}$: (%) of match 1 or 2 antiprotons in $\bar{\Lambda}$'s passing annihilation shower selection cuts for six momentum spectra

Momentum range	CLEO II MC %	CLEO II Data %	CLEO II.5 MC %	CLEO II.5 Data %
300-500 MeV	28.3 ± 1.3	13.2 ± 0.3	26.5 ± 1.0	13.3 ± 0.2
500-700 MeV	65.1 ± 1.7	52.7 ± 0.9	65.0 ± 2.6	52.2 ± 0.6
700-900 MeV	70.8 ± 1.8	60.6 ± 1.0	71.5 ± 2.8	60.9 ± 0.7
900-1100 MeV	65.3 ± 1.7	52.9 ± 0.9	63.4 ± 2.5	50.7 ± 0.6
1100-1300 MeV	50.6 ± 2.0	41.9 ± 1.0	52.2 ± 2.1	41.4 ± 0.7
1300-1700 MeV	47.4 ± 1.9	44.0 ± 1.0	46.3 ± 1.8	41.0 ± 0.7
1700-2100 MeV	56.0 ± 2.0	54.0 ± 1.0	55.1 ± 1.9	53.2 ± 0.7

The Correction Factor is weighed according to the fraction of antineutrons in a momentum range as produced in Monte Carlo. The solid distribution in Figure 5.14 is data and the dashed distribution is signal Monte Carlo.

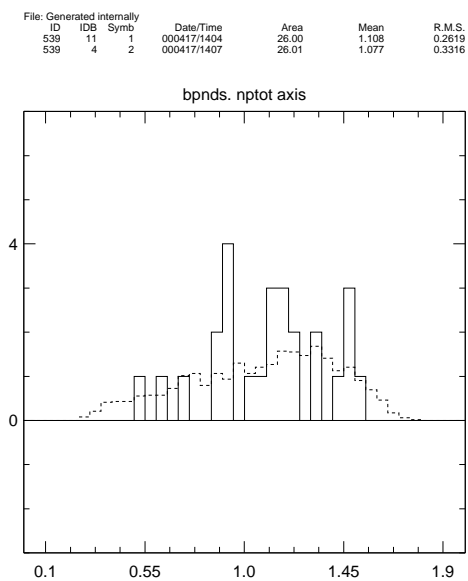


Figure 5.14: Antineutron momentum distribution (in GeV)

In Table 5.9 we calculate the Correction Factor as previously defined, as well as the fraction of antineutrons found in signal Monte Carlo for each momentum range.

Table 5.9: Correction Factor (C.F.) as a function of p_{proton} and % of antineutrons found in signal Monte Carlo for each momentum range in CLEO II/II.5

Momentum range	% of \bar{n} in MC	C.F.
300-500 MeV	9.1	2.07 ± 0.11
500-700 MeV	10.0	1.25 ± 0.04
700-900 MeV	14.7	1.17 ± 0.04
900-1100 MeV	15.2	1.24 ± 0.04
1100-1300 MeV	16.3	1.23 ± 0.06
1300-1700 MeV	20.7	1.10 ± 0.05
1700-2100 MeV	15.7	1.04 ± 0.05
300-1700 MeV	100.0	1.21 ± 0.05

We will use 1.21 as the Correction Factor by which to increase $\mathcal{B}(B^0 \rightarrow D^{*-} p \bar{n})$, which is an equally weighed average of CLEO II and CLEO II.5, and add to our list of systematic errors a 4% contribution due to this correction.

5.7.1 Backgrounds in Signal and Generic Monte Carlo

To check that our antineutron selection criteria does not contaminate our sample with showers from decays similar to $B^0 \rightarrow D^{*-} p \bar{n}$, we run our $B^0 \rightarrow D^{*-} p \bar{n}$, with $\bar{D}^0 \rightarrow K^+ \pi^-$ reconstruction code on signal Monte Carlo for $B^0 \rightarrow D^{*-} p \bar{n}$ with equal numbers of $D_1(2420)^0$ and $D_2^*(2460)^0$, $B^0 \rightarrow D^{*-} p \bar{n} \pi^0$, and $B^0 \rightarrow D^{*-} p \bar{\Delta}^0$ with $\Delta^0 \rightarrow n \pi^0$. The result for m_{B^0} are overlayed in solid on our data results, in white, for $B^0 \rightarrow D^{*-} p \bar{n}$ in Figure 5.15.

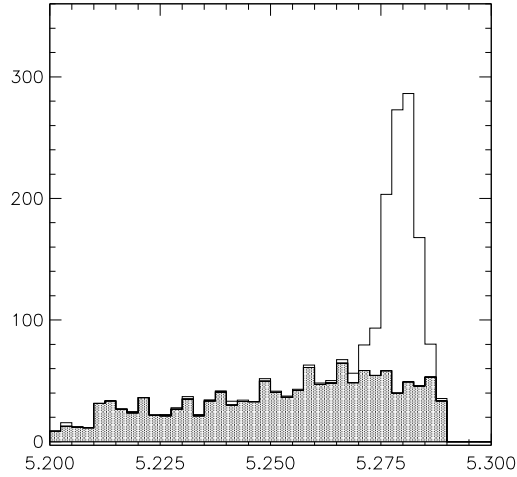


Figure 5.15: m_{B^0} in GeV for $B^0 \rightarrow D^{*-} p \bar{n}$ selection criteria applied to selected signal Monte Carlo background modes

We also run the $B^0 \rightarrow D^{*-} p \bar{n}$ code for all three D^0 modes on our generic Monte Carlo sample, as shown in Figure 5.16. The generic Monte Carlo sample is discussed in Section 3.2. Scaling the generic Monte Carlo sample to the size of our dataset, we find it to account for 40% of the background.

Within the generic MC sample $\approx 25\%$ is combinatoric background events from each of $\bar{D}^0 \rightarrow K^+ \pi^- \pi^+ \pi^-$ and $\bar{D}^0 \rightarrow K^+ \pi^-$. The remaining events, 50%, are from $\bar{D}^0 \rightarrow K^+ \pi^- \pi^0$. Since $B \rightarrow D^{*\pm} N \bar{N} X$ decays are not included in the generic MC, these events are from random combinations of a $B \rightarrow \text{Baryons}$ decay and a $B \rightarrow D^* X$ decay.

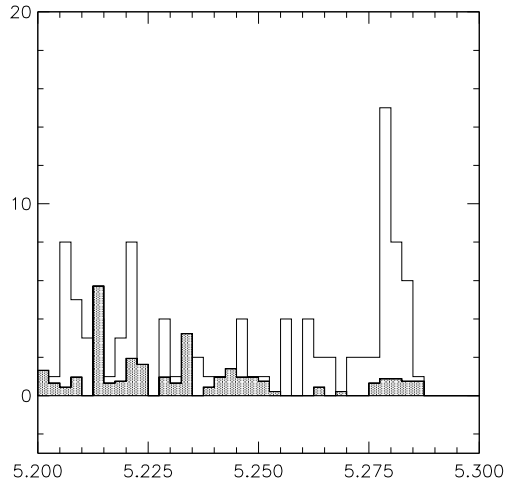


Figure 5.16: m_{B^0} for $B^0 \rightarrow D^{*-} p \bar{n}$ in GeV. (white) is data, (solid) is generic MC

We are unable to account for 60% of the background found in data in the m_{B^0} distribution for $B^0 \rightarrow D^{*-} p \bar{n}$. However, this background is small, and the m_{B^0} distribution we find is consistent with a signal at the nominal B mass.

5.8 Antineutron Directional Cosine Resolution

We compare the generated and reconstructed directional cosines for the antineutron candidates in signal Monte Carlo. We find the median error to be 37.8

milliradians. Since a single 5-cm calorimeter cell corresponds to ≈ 50 milliradians, the systematic error in our measurement of the directional cosines of the antineutron candidate shower is insignificant.

5.9 $\bar{B}^0 \rightarrow D^{*+}\bar{p}n$.

Neutrons do not annihilate in the calorimeter. Since our selection criteria for antineutron showers rejects the vast majority of neutrons, we derive a new set of cuts specific to neutrons. The selection criteria we used is shown in Figure 5.10. The most important difference with antineutrons is the selection of low energy photon-like showers.

Table 5.10: Neutron shower selection criteria

Track-to-shower match level type 3
E9OE25 > cut 1
$ (cos(\theta)) < 0.71$, or good barrel
$E_{main} < 500$ MeV

We are unable to define selection criteria that allow us to separate neutrons from soft photons. This background overwhelms the signal, making unattainable the reconstruction of $\bar{B}^0 \rightarrow D^{*+}\bar{p}n$. We plot E_{main} for neutrons (solid distribution) and antineutrons (dashed distribution) in Figure 5.17.

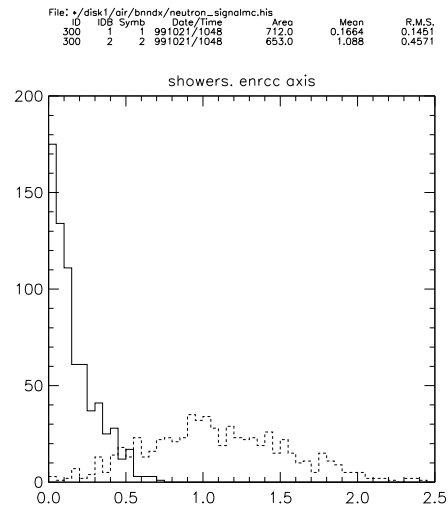


Figure 5.17: E_{main} (in GeV) for neutrons and antineutrons in $B^0 \rightarrow D^{*-} p \bar{n}$ signal Monte Carlo

5.10 Systematic Uncertainties

In Table 5.11 we show the systematic uncertainties we consider to contribute significant errors to our measurement of $\mathcal{B}(B^0 \rightarrow D^{*-} p \bar{n})$. $B^0 \rightarrow D^{*-} p \bar{n}$ has an average of 4.6 tracks.

Table 5.11: Estimate of systematic uncertainties (in %) for $B^0 \rightarrow D^{*-} p \bar{n}$

Source	Uncertainty (in %)
D^0 branching fractions	0.6
D^* branching fraction	1.4
D^* reconstruction	5.0
Monte Carlo statistics	5.0
# of $B\bar{B}$'s	2.0
tracking (1%/track)	4.6
PRLEV proton ID	4.0
Δ background contribution	5.0
Phase space versus two body	3.0
antineutron miss-ID	15.0
TOTAL	18.8 %

CHAPTER 6 CONCLUSION

This work comprises the second successful exclusive reconstruction of $B \rightarrow$ Baryons modes, after the exclusive reconstructions of $B^+ \rightarrow \bar{\Lambda}_c p \pi^+$ and $B^0 \rightarrow \bar{\Lambda}_c p \pi^+ \pi^-$ carried out by CLEO in 1997 [29]. In Table 6.1 we summarize all the exclusive $B \rightarrow$ Baryons measurements to date. We rank the modes from largest to smallest branching fraction central value. The first error is statistical and the second is systematic. The Λ_c modes have a third uncertainty, which is systematic and is due to the error in the determination of $\mathcal{B}(\Lambda_c^+ \rightarrow p K^- \pi^+)$.

Table 6.1: Exclusive measurements in $B \rightarrow$ Baryons to date

Mode	Branching Fraction ($\times 10^{-4}$)
$B^0 \rightarrow D^{*-} p \bar{n}$	$14.5_{-3.0}^{+3.4} \pm 2.7$
$B^0 \rightarrow \bar{\Lambda}_c p \pi^+ \pi^-$	$13.3_{-4.2}^{+4.6} \pm 3.1 \pm 2.1$
$B^0 \rightarrow D^{*-} p \bar{p} \pi^+$	$6.6_{-1.2}^{+1.3} \pm 1.0$
$B^+ \rightarrow \bar{\Lambda}_c p \pi^+$	$6.2_{-2.0}^{+2.3} \pm 1.1 \pm 1.0$

As shown in Table 6.1, the size of the branching fractions we are measuring in this work are of the same order of magnitude as those previously measured in decay modes including a Λ_c . We are unable to extrapolate the exclusive results to compare the relative magnitude of the inclusive modes with or without a Λ_c . For instance, the available phase space for the production of more light mesons is larger in the case of modes with a Λ_c than in the case without, which may cause the $B \rightarrow \Lambda_c X$ inclusive rate to be larger than the $B \rightarrow [D] N \bar{N} X$ inclusive

rate. However, we think it reasonable to assume that the measurements we have at our disposal to date are representative of the inclusive modes. We infer that $B \rightarrow [D]N\bar{N}X$ modes contribute significantly to the total $B \rightarrow$ Baryons decay rate.

6.1 $B \rightarrow$ Baryons phenomenology

The $B \rightarrow$ Baryons theoretical models attempted to date [48, 49] rely on the assumption that the B meson decays to two decay daughters, which is the two-body assumption. Unlike two-body B meson modes, most $B \rightarrow$ Baryons modes, including all four that have been measured to date, have at least three decay daughters. Most $B \rightarrow$ Baryons modes also have a varied resonant substructure. The assumption that the hadronization process takes place at a late stage in the decay, which allows for a substantial simplification of the equations due to the suppressed dependence on the exchange of gluons and light quarks, is justified in hard two-body decays. However, in many-body decays there can be re-scattering of the hadronizing quarks and multiple exchanges of soft gluons and virtual quarks. Notwithstanding the calculational difficulties of many-body $B \rightarrow$ Baryons decays such as the ones we measure here, progress continues to be made using HQET to explain B meson decay. The focus has been on decays for which HQET can be used to extract the most information, and which can be used to search for CP violation [14, 15]. Future attempts to theoretically explain $B \rightarrow$ Baryons are needed.

6.2 Possible Future $B \rightarrow$ Baryons Modes at CLEO

In CLEO II D^0 reconstruction from B decays is plagued by high backgrounds due to poor separation between kaons and pions. The substantial improvements in charged particle separation (pion-kaon-proton) in the CLEO III data should allow for the successful reconstruction of $B^+ \rightarrow \bar{D}^0 p \bar{n}$ and $B^+ \rightarrow \bar{D}^0 p \bar{p} \pi^+$.

The ability to reconstruct antineutron modes should allow for the reconstruction of modes of type $B \rightarrow (\Lambda_c, \Sigma_c) \bar{n} X$. Modes of type $B \rightarrow (\Lambda_c^*, \Sigma_c^*) \bar{p} X$, and $B \rightarrow \Xi_c \bar{\Lambda}_c$, which have low reconstruction efficiencies in CLEO II/II.5, are also worth pursuing.

$B \rightarrow$ Baryons for $b \rightarrow sg$, and $b \rightarrow u$ modes will also be of interest and likely within range. If previous measurements of the meson modes are used as a guide, the modes $B^+ \rightarrow \bar{\Lambda} p$, $\bar{B}^0 \rightarrow p \bar{n} \pi^-$, and $\bar{B}^0 \rightarrow p \bar{p} \pi^+ \pi^-$ are worth pursuing.

Semileptonic $b \rightarrow c$ $B \rightarrow$ Baryons decays, such as $B^+ \rightarrow \Lambda_c^- p l^+ \nu_l$, with $l = e, \mu$, due to the low reconstruction efficiency at CLEO for low momentum leptons, have not been measured. The substantially larger dataset expected in CLEO III may compensate for the low reconstruction efficiency. A mode such as $B^+ \rightarrow \bar{p} p l^+ \nu_l$ should be feasible. This latter mode can be used as an auxiliary in the measurement of $|V_{ub}|$.

6.3 Significance of Results

We have found the first evidence of decay modes of the B^0 of the type $B \rightarrow DN\bar{N}\pi$. We measure the branching fractions $\mathcal{B}(B^0 \rightarrow D^{*-} p \bar{p} \pi^+) = (6.5_{-1.2}^{+1.3} \pm 1.0) \times 10^{-4}$, and $\mathcal{B}(B^0 \rightarrow D^{*-} p \bar{n}) = (14.8_{-3.1}^{+3.5} \pm 3.0) \times 10^{-4}$. These measurements

indicate the fraction of baryonic decays of B mesons that do not proceed via Λ_c^+ may be of approximately the same magnitude as those that do.

REFERENCES

- [1] Abraham Pais, *Inward Bound*, Clarendon Press, Oxford, 1986.
- [2] *The Particle Hunters*. Y. Ne'eman and Y. Kirsh, Cambridge University Press, 1996.
- [3] *An Introduction to Quantum Field Theory*. Michael E. Peskin and Daniel V. Schroeder, Addison Wesley, 1998.
- [4] *Dynamics of the Standard Model*. John F. Donogue, Eugene Golowich and Barry R. Holstein, Cambridge University Press, 1992.
- [5] Particle Data Group. Review of particle physics. *The European Physical Journal C*, 3(1-4), 1998. The current web edition is <http://pdg.lbl.gov/>.
- [6] Y. Fukuda *et al.* (The Super-Kamiokande collaboration), hep-ex/9909022 and *Phys. Rev. Lett* 81, 1562, 1998.
- [7] V. Fanti *et al.* (The NA48 Collaboration) *Phys.Lett.* B465, 335-348, 1999.
- [8] B. H. Bherens *et al.* (CLEO Collaboration) hep-ex/0005013. Submitted to *Phys. Rev. Lett.*
- [9] D. J. Gross and F. Wilczek, *Phys. Rev. Lett.* 30, 1343, 1973.
- [10] H. D. Politzer, *Phys. Rev. Lett.* 30, 1346, 1973.
- [11] Chris Quigg, *Gauge Theories of the Strong, Weak, and Electromagnetic Interactions*, Benjamin/Cummins, 1983.
- [12] M. B. Voloshin, *Inclusive Weak Decay Rates of Heavy Hadrons*. hep-ph/0004257.
- [13] M. Shifman, *Snapshots of Hadrons*. hep-ph/9802214.
- [14] Mathias Neubert. *Introduction to B physics*. hep-ph/0001334.
- [15] Mark B. Wise. *Heavy Quark physics*. hep-ph/9805468.

- [16] N. Isgur and M.B. Wise, Phys. Lett B 237, 527, 1990.
- [17] Karl M .Ecklund. Semileptonic B decays at CLEO. hep-ex/9912034.
- [18] M. E. Luke, Phys. Lett B 252, 447, 1990.
- [19] M. Bauer, B. Stech and M. Wirbel, Z. Phys. C 34, 103, 1987.
- [20] Mathias Neubert. Non-Leptonic Weak Decays of B mesons. hep-ph/9705292.
- [21] A. J. Buras and L. Silvestrini. Non-Leptonic Two-Body B Decays Beyond Factorization. hep-ph/9812392.
- [22] K. G. Wilson, Phys. Rev. 179, 1499, 1969.
- [23] A. J. Buras. Operator Product Expansion, Renormalization Group and Weak Decays. hep-ph/9901409.
- [24] G. Crawford *et al.* (CLEO Collaboration) Phys. Rev. D 45: 752, 1992
- [25] M. Procaro *et al.* (CLEO Collaboration) Phys. Rev. Lett 73, 1472, 1994.
- [26] B. Barish *et al.* (CLEO Collaboration) Phys. Rev. Lett 79, 3599-3603, 1997.
- [27] G. Bonvicini *et al.* (CLEO Collaboration) Phys. Rev. D57: 6604-6608, 1998.
- [28] T. E. Coan *et al.* (CLEO Collaboration) Phys. Rev. D59: 111101, 1999.
- [29] X. Fu *et al.* (CLEO Collaboration) Phys. Rev. Lett 79, 3125, 1997.
- [30] D. Jaffe *et al.* (The CLEO Collaboration), CLEO 00-3, accepted for publication in Phys. Rev. D.
- [31] M. Zoeller, Ph. D. Thesis, State University of New York, Albany, 1994 (unpublished).
- [32] I. Dunietz. Phys. Rev. D58: 094010-1, 1998.
- [33] Y. Kubota *et al.* Nucl. Instrum. Methods Phys. Res. A 320, 66, 1992.
- [34] Introduction to High Energy Physics. Donald H. Perkins, Addison-Wesley, 1987.
- [35] T. Hill. Nucl. Instrum. Methods Phys. Res. A 418, 32-39, 1998.
- [36] I. Brock, Mn_fit: A fitting and Plotting Package Using Minuit. L3 Note, 918, 1995.

- [37] Minuit: Function Minimization and Error Analysis. CERN Program Library, D506.
- [38] G. C. Fox and S. Wolfrum, Phys. Rev. Lett. 41, 1581, 1978.
- [39] L. Gibbons *et al.* CLEO CBX, 96/103, 1996 (unpublished).
- [40] L. Gibbons *et al.* (CLEO Collaboration) Phys. Rev. D 56, 3783, 1997.
- [41] P. Avery. KNLIB documentation. <http://www.phys.ufl.edu/avery/kwfit>
- [42] C. Prescott. The knvf secondary vertex fitting package. CLEO CSN, 97/353, 1997 (unpublished).
- [43] C. Amsler. Rev. Mod. Phys. 70 No.4, 1293, 1998.
- [44] C. Amsler *et al.* Annu. Rev. Nuc. Part. Sc. Vol 41, p219, 1991.
- [45] G. Brandenburg *et al.* (CLEO Collaboration) Phys. Rev. Lett 80, 2762-2766, 1998.
- [46] J. Rodriguez *et al.* CLEO CBX, 96/64, 1996 (unpublished).
- [47] A. Foland. CLEO CBX, 97/70, 1997 (unpublished).
- [48] M. Jarfi *et al.* Phys. Rev. D 43, 1599, 1991.
- [49] N. G. Deshpande *et al.* Mod. Phys. Lett. A 3, 749, 1988.

BIOGRAPHICAL SKETCH

Antonio Rubiera was born in Havana, Cuba on January 21, 1967. He came to the U.S. by the Mariel boatlift in 1980. He attended Shenandoah Jr. High and Miami Sr. High in Miami, Florida. From 1986 to 1991 he attended Cornell University, obtaining a B.S. and an M.Eng., both in Electrical Engineering. From 1991 to 1994 he resided in Miami, where he worked for the Latin America branch of Ingersoll-Rand Co. He pursued a PhD in physics at the University of Florida from 1995 to 2000.

